General Disclaimer

One or more of the Following Statements may affect this Document

- This document has been reproduced from the best copy furnished by the organizational source. It is being released in the interest of making available as much information as possible.

- This document may contain data, which exceeds the sheet parameters. It was furnished in this condition by the organizational source and is the best copy available.

- This document may contain tone-on-tone or color graphs, charts and/or pictures, which have been reproduced in black and white.

- This document is paginated as submitted by the original source.

- Portions of this document are not fully legible due to the historical nature of some of the material. However, it is the best reproduction available from the original submission.

GRADUATE AERONAUTICAL LABORATORIES
CALIFORNIA INSTITUTE OF TECHNOLOGY

A FLYING HOT WIRE STUDY OF THE TURBULENT NEAR WAKE OF A CIRCULAR CYLINDER AT A REYNOLDS NUMBER OF 140, 000

Thesis by

Brian Joseph Cantwell

Experimental Study of Flow about Bluff Bodies
Including a Circular Cylinder
and a Stalled Two-Dimensional Airfoil

Progress Report No. 7

February, 1975 - October, 1975

NASA Grant NGL 05-002-229

D. Coles (PI) and B. Cantwell
California Institute of Technology
1201 E. California Blvd.
Pasadena, California 91125

Firestone Flight Sciences Laboratory

Guggenheim Aeronautical Laboratory

Karman Laboratory of Fluid Mechanics and Jet Propulsion

Pasadena

A FLYING HOT WIRE STUDY OF THE TURBULENT NEAR WAKE OF A CIRCULAR CYLINDER AT A REYNOLDS NUMBER OF 140,000

Thesis by

Brian Joseph Cantwell

In Partial Fulfillment of the Requirements

for the Degree of

Doctor of Philosophy

California Institute of Technology

Pasadena, California

1976

(Submitted October 3, 1975)

ACKNOWLEDGEMENT

The author would like to express his appreciation to the many people who contributed to this reseach.

Especially to the author's advisor, Professor Donald Coles, whose expertise, particularly with regard to experimental techniques, was an invaluable source of aid and inspiration.

To Professor Anatol Roshko whose timely advice first sparked the author's interest in separated flows.

To the people of NASA Ames Research Center who provided funds for the research.

To Doctor Anthony Perry who contributed the design as well as his understanding of the hot wire anemometers.

To William Bettes and the members of the 10 Foot Wind Tunnel crew, Jerry Landry and Efraim Mandracchia for their willing and skilled cooperation during the hectic period of the cylinder experiment.

To Mrs. Karen Cheetham who spent long hours proofreading, correcting and typing the manuscript.

Deepest gratitude is felt toward my wife, Ruth, and daughter, Alice, whose encouragement and willing sacrifice made all the difference. They always understood.

ABSTRACT

An experiment was performed in the GALCIT 10-foot wind tunnel to study the flow in the near wake of a circular cylinder at a Reynolds number of 140,000.

The main objective of this investigation was to study the phenomenology of the processes of vortex formation and transport in the near wake, at a Reynolds number sufficiently high to insure a fully turbulent wake, but low enough to insure a laminar separation. The latter requirement anticipates the eventual use of the results as a test case for advanced calculation codes.

Much current experimental work on turbulent flows is concerned with large, coherent, organized vortex structures which have a relatively long lifetime and which account for much of the transport of mass, momentum and heat in turbulent shear flows. High Reynolds number flow past a cylinder is one case where such structures dominate.

The apparatus developed for measuring this flow consists of x-array hot wire probes mounted on the ends of a pair of whirling arms. In such a flow, where large changes in flow direction occur, a fixed hot wire would rectify the velocity signal and give ambiguous results. However, by applying a large enough bias velocity to the wires, the relative velocity vector can be maintained within the ±30 degree range of sensitivity of the x-array. One useful property of this technique is that a rotation of the arms in a uniform flow applies a wide range of relative flow angles to the x-arrays, making them inherently self-calibrating in pitch.

The most important element of the instrumentation concomitant to the flying hot wire is a computer controlled data acquisition system which is slaved to the position of the rotating arm and which manages, monitors, edits and records the vast profusion of data which is continuously poured out by the device. A fast sensor responding to model surface pressure was used to generate a signal synchronized with the vortex-shedding process. This signal was recorded along with the hot wire data and used later to sort the data into populations having the same phase. Ensemble averages conditioned this way yield an average picture of the instantaneous flow field in which the vortices are frozen as they would be in a photograph.

In addition to the conventional velocity, pressure and stress data, results are presented which show the instantaneous (in the sense of an average at constant phase) velocity, intermittency, vorticity and stress fields as a function of phase for the first six diameters of the near wake.

In the present study, the Reynolds stresses are broken up into the contribution from large scale periodic motions and that from background or random turbulence, and, when dissected in this way, permit an enlightening look at the anatomy of this turbulent flow. Laid against the background of the instantaneous velocity, vorticity and intermittency, the stresses in the near wake emerge as a concatenation of peaks and valleys, some the result of strong induced motions in the outer flow which cause free stream fluid to move rapidly inward toward the center of the wake, others the result of the random motions of the background turbulence.

TABLE OF CONTENTS

TABLE OF CONTENTS (Cont'd)

LIST OF TABLES

LIST OF FIGURES

LIST OF FIGURES (Cont'd)

LIST OF FIGURES (Cont'd)

LIST OF FIGURES (Cont'd)

I. INTRODUCTION

It has become increasingly clear to many workers in turbulence research that the process of Reynolds averaging of the equations of motion hides from view many of the salient features of turbulent flow. In an effort to retain some of these features and to understand the physics of turbulence, various conditional sampling and conditional averaging techniques have been developed.

As an outgrowth of this work, a new element has emerged--the so-called "large eddy" or "coherent structure", which accounts for much of the transport of momentum, mass and heat in turbulent shear flows. Whatever name is used to describe it, the large eddy represents an organized part of the motion in turbulence which may retain its identity over many characteristic lengths of the flow.

The experimental techniques used to isolate these coherent motions all have a common difficulty, which is that while the motion of the eddy may not be random, the passage of an eddy by a particular position in a flow often is, itself, a random event. This difficulty is particularly true in the case of the flat plate boundary layer. In the case of the turbulent mixing layer, rapid changes in scale result in strong interactions between large eddies which cause them to lose their identity in a process of amalgamation (the cascade to low wave number described by Brown and Roshko, Ref. 2).

The flow around a circular cylinder at high Reynolds number is the most outstanding example where this difficulty is not encountered. Here the vortices are produced naturally in a constant, regular manner. Except for some dispersion, they are not subject

to pairing or some combining process which might obscure their identity (at least in the first few diameters downstream of the cylinder).

The flow in the near wake is a collage of many important processes which occur in a wide variety of turbulent flows. The cylinder imparts to the fluid both positive and negative vorticity. The two shear layers from opposite sides of the cylinder combine in a complicated roll up process to form the eddies which, once formed, rapidly accelerate downstream, interacting with their neighbors in a process of relaxation toward a stable, slowly changing wake.

The regular periodic character of the processes of vortex formation and movement downstream make it possible to identify the large eddy for this flow and to trace its history as it is carried downstream. In a frame of reference moving with the cylinder, the flow field takes on the appearance of a wave of frequency equal to the shedding frequency (37 Hz in this experiment) and of wavelength equal to about 4.3 diameters. From this information, one can calculate the wave speed to be about 1600 cm/sec or about 75 percent of the free stream speed (U_∞). In a frame of reference moving downstream at this velocity, the vortices become apparent as a pattern of centers and saddles which delineate the individual structures and locate regions of opposite vorticity. In fact, this method of visualizing the structures is ambiguous, since no single value of the celerity for the vortices can apply over the entire first six diameters of the near wake where the eddies are strongly

accelerated. However, there are other, unambiguous criteria for locating the vortex centers. The best of these is the peak in the instantaneous vorticity field. In this respect the eddies are real entities, and if one is willing to focus on one eddy, there exists a best frame of reference for viewing the instantaneous streamline pattern of the average eddy.

In the experiment described in this thesis, the flow in the near wake at a Reynolds number of 140,000 was mapped using a fast sensor responding to model surface pressure to keep track of the phase of the vortex shedding process. X-array hot wire sensors on the ends of a pair of whirling arms sampled the flow at closely spaced points along an arc approximately 151 cm in diameter.

Later, the data taken at each point in the flow were sorted into 16 groups, each corresponding to successive constant values of the phase of the surface pressure signal. The result is a 16-frame animation of the flow in terms of intermittency, instantaneous velocity, instantaneous vorticity and instantaneous Reynolds stresses. These results are in addition to the more conventional results for the globally averaged flow field.

It is necessary to state what is meant by an average at constant phase and how an average at constant phase is related to the global average.

Represent a fluctuating quantity by

$$s(t) = \bar{s} + \tilde{s}(t) + s'(t) = \bar{s} + s''(t) \qquad (1.1)$$

where $\bar{s}$ is the global mean of s defined by an ensemble average

$$\bar{s} = \frac{1}{N} \sum_{n=1}^{N} s_n \qquad (1.2)$$

and $\tilde{s}$ is the periodic part of the motion with period τ such that $\tilde{s}(t) = \tilde{s}(t + m\tau)$ (m an integer), and

$$\tilde{s}(\psi) = \frac{1}{N_\psi} \sum_{n=1}^{N_\psi} (s((\psi + n)\tau) - \bar{s}). \qquad (1.3)$$

Here ψ is the phase of $\tilde{s}$ and is a dimensionless number in the range 0 to 1, and $(\psi + n)\tau$ is the time at which a sample with phase ψ is taken. N_ψ is the number of samples taken at phase ψ. The random part of the signal is s'. At any given instant $\tilde{s} + s'$ (also denoted by s'') represents the fluctuation of s away from the global mean.

In practice, the surface pressure signal was neither a pure harmonic nor exactly periodic function. Its amplitude was modulated in a random way with maxima and minima occurring about 15-20 cycles apart. The frequency of the vortex shedding (center frequency 37 Hz) also varied, but these changes in frequency were effectively tracked out by a phase-lock loop. The phase-lock loop generated a ramp, synchronized with the pressure, which was later used to assign phase information to the data. A histogram of the period of the ramp signal showed that the shedding frequency spent more than 90 percent of its time within 10 Hz of the center frequency. Loss of lock was rare.

The issue of whether or not the average at a constant phase of such an imperfect reference oscillator is meaningful finally

hinges on how well the flow repeats itself from cycle to cycle. From all the empirical evidence thus far, the answer to this would seem to be that, in spite of a small amount of dispersion, the flow repeats rather well.

To determine some of the properties that follow from the definitions of time and phase averages, let $< >$ denote the operation of averaging a signal at constant phase. Consider a population of N samples of s. Assume for simplicity that the period of the periodic part of the signal is divided into p equally spaced intervals. The population can then be sorted into groups, each corresponding to an interval of the phase. In this way

$$\bar{s} = \frac{1}{N}\sum_{n=1}^{N} s_n = \frac{1}{N}\left\{N_1\left[\frac{1}{N_1}\sum_{n_1=1}^{N_1} s_{n_1}\right] + \ldots N_p\left[\frac{1}{N_p}\sum_{n_p=1}^{N_p} s_{n_p}\right]\right\}. \qquad (1.4)$$

If the sampling process is completely asynchronous with the periodic motion, then, in the limit of a large number of samples, $N_i/N \rightarrow 1/p$, $i=1, 2, \ldots p$, and

$$\bar{s} = \frac{1}{p}\sum_{i=1}^{p} \langle s\rangle_i = \overline{\langle s\rangle}. \qquad (1.5)$$

Note that equation (1.5) is exact independently of the value of p and also that the same result holds for any sampled quantity. For example,

$$\overline{U'V'} = \overline{\langle U'V'\rangle}. \qquad (1.6)$$

Consider the correlation between the periodic motion and the random fluctuations. Then

$$\langle \tilde{s}f' \rangle_i = \lim_{N_i \to \infty} \frac{1}{N_i} \sum_{n_i=1}^{N_i} \tilde{s}_i f'_{n_i} = \lim_{N_i \to \infty} \frac{1}{N_i} (\tilde{s}_i) \sum_{n_i=1}^{N_i} f'_{n_i} = 0 \quad . \tag{1.7}$$

From equation (1.5),

$$\overline{\langle \tilde{s}f' \rangle} = \frac{1}{p} \sum_{i=1}^{p} \langle \tilde{s}f' \rangle_i = 0 \tag{1.8}$$

which states that the background turbulence and the periodic motion are uncorrelated.

Some other properties which follow immediately are

$$\langle s' \rangle = 0 \ , \quad \bar{\tilde{s}} = 0 \ , \quad \bar{s}' = 0 \tag{1.9}$$

$$\overline{\bar{s}f} = \bar{s}\bar{f} \ , \tag{1.10a}$$

$$\langle \tilde{s}f \rangle = \tilde{s}\langle f \rangle = \tilde{s}(\bar{f} + \tilde{f}) \tag{1.10b}$$

and

$$\langle \bar{s}f \rangle = \bar{s}\langle f \rangle \ . \tag{1.11}$$

Reynolds and Hussain (Ref.10) cast the equations of motion into a form appropriate to this discussion, and much of what immediately follows will be based on their work.

For incompressible constant property flow, the dimensionless Navier-Stokes equations, using the summation convention, are

$$\frac{\partial U_i}{\partial x_i} = 0 \tag{1.12}$$

and

$$\frac{\partial U_i}{\partial t} + U_j \frac{\partial U_i}{\partial x_j} = - \frac{\partial P}{\partial x_i} + \frac{1}{Re} \frac{\partial^2 U_i}{\partial x_j \partial x_j} \quad . \tag{1.13}$$

Decompose the velocity and pressure fields as

$$U_i = \overline{U_i} + \tilde{U}_i + U_i' \tag{1.14}$$

$$P = \overline{P} + \tilde{P} + P' \quad . \tag{1.15}$$

Substituting equation (1.14) into equation (1.12) and averaging, one obtains

$$\frac{\partial \overline{U}_i}{\partial x_i} = 0 \quad , \quad \frac{\partial (\widetilde{U} + U')_i}{\partial x_i} = 0 \quad . \tag{1.16}$$

Averaging equation (1.16) at constant phase, one obtains

$$\frac{\partial \widetilde{U}}{\partial x_i} = 0 \, , \quad \frac{\partial U'}{\partial x_i} = 0 \tag{1.17}$$

Substituting equations (1.14) and (1.15) into the momentum equation and averaging at constant phase, one obtains

$$\frac{\partial \widetilde{U}_i}{\partial t} + \overline{U}_j \frac{\partial \overline{U}_i}{\partial x_j} + \overline{U}_j \frac{\partial \widetilde{U}_i}{\partial x_j} + \widetilde{U}_j \frac{\partial \overline{U}_i}{\partial x_j} =$$

$$-\left(\frac{\partial \overline{P}}{\partial x_i} + \frac{\partial \widetilde{P}}{\partial x_i}\right) - \frac{\partial}{\partial x_j} \langle U_i' U_j' \rangle - \frac{\partial}{\partial x_j} (\widetilde{U}_i \widetilde{U}_j) + \frac{1}{Re} \left(\frac{\partial^2 \overline{U}_i}{\partial x_j \partial x_j} + \frac{\partial^2 \widetilde{U}_i}{\partial x_j \partial x_j}\right) \tag{1.18}$$

The global average of equation (1.18) gives the equations for the mean field:

$$\overline{U}_j \frac{\partial \overline{U}_i}{\partial x_j} = -\frac{\partial \overline{P}}{\partial x_i} + \frac{1}{Re} \frac{\partial^2 \overline{U}_i}{\partial x_j \partial x_j} - \frac{\partial}{\partial x_j} \overline{\langle U_i' U_j' \rangle} - \frac{\partial}{\partial x_j} (\overline{\widetilde{U}_i \widetilde{U}_j}) \quad . \tag{1.19}$$

Equation (1.19) differs from the usual mean equation for turbulent flow only in the last two terms and indicates that the mean Reynolds stress may be broken up into two components

$$\overline{U_i'' U_j''} = \overline{\widetilde{U}_i \widetilde{U}_j} + \overline{\langle U_i' U_j' \rangle} \tag{1.20}$$

where '' denotes a fluctuation away from the global mean. The first term on the right hand side of equation (1.20) is the contribution to the mean Reynolds stress from the large scale periodic motion. The second term is the contribution from the correlation between fluctuations away from the mean at constant phase averaged over

all phases. In this sense, the quantity $\langle U_i' U_j' \rangle$ can be thought of as the contribution to the Reynolds stress at a given phase of the motion due to the background turbulence that pertains at that phase. The sum $\tilde{U}_i \tilde{U}_j + \langle U_i' U_j' \rangle$ can be regarded as the instantaneous Reynolds stress if one is careful to keep in mind that it does <u>not</u> represent the <u>total</u> transport of momentum in any one direction at any instant due to fluctuating velocities.

One of the main themes of this research is an examination of the flow in the near wake in terms of equation (1.20). The cylinder experiment is an attempt to answer by observation some of the basic questions about the transport processes at work in a turbulent flow. Where are the stresses produced? How much stress is due to the large scale motions? How much stress is due to the background turbulence?

II. THE APPARATUS

2.1 The Cylinder Model

Figure 2.1 shows a detail of the cylinder model used in the experiment. A 297.2 centimeter* length of stainless steel tubing 10.137 cm in diameter was centerless ground and lapped to an outside surface roughness of about 30-100 micro centimeters. The inside was honed to fit a series of sealed pistons which connected 0.076 cm diameter pressure holes in the wall of the tubing to pressure instrumentation outside the tunnel. At the center span position, the holes were drilled at -90, -45, -30, 0, +45, and +90 degrees in a spiral pattern with a lateral spacing of 1.59 cm, so that each cell of the central piston was ventilated by only one tap. Two other -30 degree holes, located 9.84 cm on either side of center, were used for two fast response Pitran pressure transducers which were installed inside the model and closely coupled to the surface orifices. One Pitran was used mainly to monitor the phase of the vortex-shedding cycle, while the other was used briefly to verify that the shedding was acceptably two dimensional over a lateral distance of at least two cylinder diameters. A series of taps at the 180-degree position along the base was used to measure the base pressure distribution as a check on the two-dimensionality of the flow. End plates 60.96 cm in diameter were used to reduce the adverse effect of the tunnel wall boundary layer on the flow.

---

*Wherever appropriate, metric units are used. The exceptions to this are:

1) vertical traverse settings (inches)
2) tunnel dynamic pressure as set by tunnel operator (lbs/ft^2)
3) all other pressures (mm Hg).

The model is held in place by a pair of ringfeder locking assemblies. The outer ring of the locking assembly bears up against the inside wall of the stainless steel tubing. The inner ring of the locking assembly tightens around an aluminum plug with a threaded central hole which is used to hold a hollow shaft. This shaft is inserted through an oversized hole in the wall of the test section and is used to rotate the model for measuring pressure distributions. Pressure tubing from inside the model is brought out through the center of the shaft to a pressure manifold outside the tunnel. The aluminum plug fits over a short length of steel tubing welded to a piece of steel plate which is bolted into a T-slot along the tunnel centerline.

The Pitran sensor consists of a small can, to the inside of which is attached a stylus which bears on the emitter-base junction of a transistor. Variations in the difference between the inside and outside pressure cause the stress exerted by the stylus to vary, changing the current gain of the transistor. The response is linear over a fairly wide range. However, the DC bias of the transistor has a tendency to drift.

2.2 Mechanical Design of the Flying Hot Wire

Figure 2.2 shows some of the details of the flying hot wire apparatus. The arms are constructed of 321 seamless stainless steel elliptical tubing with a thickness ratio of about 0.33. The hub to which the arms are fastened is fitted onto a hub extension, and the unit is bolted to a steel flange mounted on the shaft of a DC motor by a split hub clamp. The hub extension moves the

rotating arms out away from the flow disturbance caused by the supporting strut. The motor is of the permanent magnet type, model U16M4 built by Printed Motors, Inc. This assembly is clamped into an 203.2 cm length of two- by eight-inch steel tubing. Wooden cladding attached to the steel tubing is shaped to a NACA 0024 profile to form a streamlined strut. The strut is fastened to the saddle of a Gilman slide assembly mounted vertically on a machined angle plate which rides on the saddle of a lathe bed. The whole assembly of about 1800 pounds of metal and machinery is designed to move a pair of tiny, barely visible wires through a flow at a known speed and a known position. The vertical traverse has a range of 36 inches and is repeatable to 0.001 of an inch. The horizontal traverse has a range of 106.68 cm and is repeatable to several thousandths of a centimeter.

Figure 2.2 also shows the arrangement of the apparatus and model in the GALCIT 10-foot wind tunnel. Hot wires are mounted in clamp-type holders at the ends of the arms. A square section on the probe slips into a square recess broached in the forward end of the clamp, allowing the probe to be rotated 90 degrees about its axis and back without losing registration. Figure 2.3 shows a side view of one arm with an x-array probe mounted in its holder.

Hot wire signals are brought, via low noise microdot cables, down through the hollow arms to the hub and thence through a 0.953 cm diameter through-hole along the axis of the motor shaft. The rotating leads make contact with stationary terminals through a set of 12 mercury slip rings. The circuit just described

represents a quarter of the resistance bridge of a constant temperature anemometer. The slip rings lie within the bridge, and for this reason the resistive noise (~10 milliohms) associated with brush-type rings is a serious problem. Mercury slip rings with their extremely low resistance variations are an excellent remedy. The four hot wires use eight rings, and the remaining four rings are used to carry power, ground, and signal leads to an Optron proximity sensor located on the end of arm I. Low noise microdot cables carry the signals from the slip rings down through the center of the streamlined strut to isolated BNC connectors at the bottom.

2.3 Geometry

Figure 2.4a shows the various important dimensions of the flying hot wire. The arm angle ϕ is measured in a counterclockwise direction from the top dead center position of the x-array sensor. The flow angle α is zero when ϕ is zero and increases with increasing ϕ. The angle at which the first of 128 frames* of digital data is taken (12 samples/frame) is called ϕ_1. The arms are 75.25 cm long** and the x-array probe is nominally held at a right angle, with the center of the sensor 7.43 cm away from a diameter

*The term "frame" will be used to denote any one of the following: the position along the arc where a burst of 12 samples is taken, the unit of data represented by a burst, or the temporal relation between bursts; e.g., "10 frames later".

**This distance is measured from the center of rotation to the axis of the probe. The distance from the outer edge of the arms to the center of rotation is 75.41 cm.

through the centroid of the arms. Therefore, the cross of the x-array is rotated 5.64 degrees in a clockwise direction in its own plane. This small rotation of the wires proves useful in the wake region near the cylinder where the relative flow vector tends to come from positive α. The radius line to the center of the sensor measures 75.57 cm for arm I and 75.76 cm for arm II. The difference of 1.9 mm was due to individual differences between x-array probes.

The origin of the coordinates for the experiment is taken to be the center of the cylinder. However, in practice, the physical origin of the two-dimensional traverse was used, and equations (2.1) (2.2), and (2.3) determine the coordinates of the data relative to the cylinder origin.

$$X = X_T + 28.61 - R \sin\phi_N \quad \text{(cm)} \tag{2.1}$$

$$Y = Y_T - 105.00 + R \cos\phi_N \quad \text{(cm)} \tag{2.2}$$

$$\phi_N = -86.31^\circ + (180^\circ/128)(N-1) \; ; \; N = 1, 2, \ldots 128 \tag{2.3}$$

One of the most useful features of the flying hot wire is that it is self-calibrating in pitch. Each time the arm rotates in a uniform flow, the x-array sensor is subjected to a wide range of relative flow angles. The range of angles and where they occur depends on the parameter $K = \omega R/U_\infty$, the ratio of the tip speed to free stream speed. The relative flow vector normalized by U_∞ is shown in Figures 2.4b and 2.4c where the uniform stream is represented by the rotating unit vector. Figure 2.4c is helpful in understanding how the relative flow angle α and magnitude U_r vary

as the arm rotates when K is positive and less than 1. As the unit radius moves in a counterclockwise direction, α and ϕ vary from 0 degrees to π or $-\pi$ and back to 0 degrees. On the upper part of the circle, α varies more slowly than ϕ, and on the lower part, α varies more rapidly than ϕ. When K is larger than 1 (Figure 2.4b), α swings continuously between some positive value less than $\pi/2$ and its complement, as the unit vector (the free stream) moves in a circle (see also Figure 2.4d). From these figures it follows that when the arms rotate in a uniform stream,

$$\tan \alpha = \sin\phi/(\cos\phi + K) \; ; \; \begin{matrix} \phi \in (-\pi, \pi) \\ \alpha \in (-\pi, \pi) \end{matrix} \qquad (2.4)$$

and

$$\frac{U_r}{U_\infty} = (1 + K^2 + 2K\cos\phi)^{\frac{1}{2}} \; ; \; K = \omega R/U_\infty \quad . \qquad (2.5)$$

Equations (2.6) and (2.7) are used to transform from flying to fixed coordinates when the flow vector relative to the sensor (components Ux_r, Uy_r) is known. The usual convention is used, where 1 denotes the downstream direction, and 2 the lateral direction.

$$U_1 = (Ux_r - R\omega)\cos\phi + Uy_r \sin\phi \qquad (2.6)$$

$$U_2 = -Uy_r \cos\phi + (Ux_r - R\omega)\sin\phi \qquad (2.7)$$

Notice that positive Uy_r is defined as motion toward the center of rotation so as to be consistent with the sign convention for α.

2.4 Probe and Wake Interference

The flying hot wire represents a potentially large disturbance to the flow. As the arm rotates in a uniform stream, the sensor may pass through particles of fluid which have come into contact

with some part of the moving arm at an earlier time. This interference problem can be treated in terms of a model which assumes that streamlines are straight and horizontal and that fluid particles which contact the arms are thereafter convected with the free stream velocity. In this discussion ϕ is chosen to be in the range $0 < \phi < 2\pi$ where $\phi = 0$ occurs when arm I (open points in Figure 2.5b) is at top dead center.

Referring to Figures 2.4d and 2.5a it is clear that there can be interference only for $\pi \leq \phi \leq 2\pi$ since for $0 < \phi < \pi$ contaminated fluid particles are always convected away from the boundary of the circle traced out by the probe tip. Interference for $3\pi/2 \leq \phi \leq 2\pi$ can only occur for angles that are such that the sensor is passing through the wake produced by portions of the arm which have passed through this quadrant at some earlier time. Interference with the upstream edge of the wake produced along a line of constant y will define the maximum value of ϕ for which there will be this kind of interference. Similarly, this sort of wake catching interference can occur in the lower right hand quadrant ($\pi < \phi < 3\pi/2$) for high rates of rotation ($K > 2.973$).

Figure 2.5a indicates regions of interference for $0 < K < 2$ (negative values of $(d\phi/dt)$ were never used). Figure 2.5b indicates the path of the flying arm as it would be viewed in a frame of reference in which the fluid is at rest. In this frame the arm moves from right to left (toward negative x). A point along the arm at a radius, r, follows a cycloidal path which is curtate if $r\omega/U_\infty < 1$ and prolate if $r\omega/U_\infty > 1$. The parametric

equations of the trajectory traced out by such a point on arm I are

$$x = \frac{U_\infty}{\omega}\phi - r\sin\phi \tag{2.8}$$

and

$$y = r\cos\phi \ . \tag{2.9}$$

Differentiate equations (2.8) and (2.9) to find the velocity of the point in the chosen frame of reference.

$$\dot{x} = -U_\infty - r\omega\cos\phi$$

$$\dot{y} = -r\omega\sin\phi$$

At any time when $\pi/2 < \phi < 3\pi/2$, there will be one point along the arm, at a radius r_o, for which the instantaneous direction of motion is tangent to the cusp shaped envelope of arm positions (marked by small solid dots in Figure 2.5b) and hence along the direction of the arm itself. This condition implies that

$$\tan\left(\phi - \frac{\pi}{2}\right) = \frac{\dot{y}}{\dot{x}} = \frac{k_o\sin\phi}{1+k_o\cos\phi} \tag{2.10}$$

where $k_o = r_o\omega/U_\infty$. Solving equation (2.10) for k_o, one obtains the result that

$$k_o = -\cos\phi \quad . \qquad \frac{\pi}{2} \le \phi \le \frac{3\pi}{2} \tag{2.11}$$

When $K = R\omega/U_\infty$ is greater than 1, r_o must be such that $r_o\omega/U_\infty \le 1$. When $K < 1$, r_o must be such that $r_o\omega/U_\infty \le K$. In either case, r_o represents the point along the arm which, at a given value of ϕ, lies on the envelope of arm positions. The parametric equations of the envelope become

$$x_e = -\frac{U_\infty}{\omega}\phi' + \frac{U_\infty}{\omega}\cos\phi'\sin\phi' \tag{2.12}$$

and $$y_e = -\frac{U_\infty}{\omega}\cos^2\phi' \quad . \tag{2.13}$$

Interference begins when the position of the sensor (r = R) coincides with the envelope of arm positions. In Figure 2.5a, one rotation of the arm at a fixed value of K > 0 can be described by a horizontal line directed from left to right. For K < 1, interference occurs beginning at the point A in Figure 2.5a, in the range $\pi < \phi < 3\pi/2$, where the probe enters the wake currently being laid down by its own arm. Equating (2.12) and (2.13) to (2.8) and (2.9), respectively, with r = R and $\phi = \phi'$, results in the boundary of the slant shaded region on the right side of Figure 2.5a for K < 1.

$$K(\phi) = -\cos\phi \quad \begin{cases} K < 1 \\ \pi < \phi < 3\pi/2 \end{cases} \tag{2.14}$$

For K > 1, interference occurs beginning at point B in Figures 2.5a and 2.5b, in the range $\pi < \phi < 3\pi/2$ where the probe enters the wake previously laid down when its own arm passed through the quadrant $\pi/2 < \phi < \pi$. At the position $\phi = \pi$, the outer part of the arm is receding faster than its own wake since $\omega r > U_\infty$; however, the probe must eventually encounter the wake from the inner part of the arm. Equating (2.12) and (2.13) to (2.8) and (2.9), respectively, with r = R, one obtains

$$-K(\phi)\sin\phi - \phi = \sin\phi'\cos\phi' - \phi \quad \begin{cases} \text{all } K \\ \pi < \phi < 3\pi/2 \end{cases} \tag{2.15}$$

$$-K(\phi) = \cos^2\phi' \quad . \tag{2.16}$$

The boundary of the slant shaded region on the right side of Figure 2.5a for K > 1 is found by allowing the parameter ϕ' in

equations (2.15) and (2.16) to vary from $\pi/2$ to π and solving the resulting equations for ϕ and K numerically.

The most important type of interference occurs in the upper rear quadrant of a revolution ($3\pi/2 < \phi < 2\pi$) beginning at $\phi = 270^{\circ}$ and ending at the point C in Figure 2.5a or 2.5b where the rearward arm passes out of the wake of the forward arm. Past positions of the trajectory of arm II are given by

$$x = R\sin\phi' - \frac{U_\infty}{\omega}\phi' \qquad (2.17)$$

$$y = -R\cos\phi' \quad . \qquad (2.18)$$

Coincidence in y (equations (2.18) and (2.9) with r = R) requires that $\phi' = \pi - \phi \pm 2n\pi$, n = 0, 1, 2.... Coincidence in x with n = 1 defines the interference boundary,

$$K(\phi) = \frac{\frac{3\pi}{2} - \phi}{\sin\phi} \qquad \begin{cases} \text{all } K \\ 3\pi/2 < \phi < 2\pi \end{cases} , \qquad (2.19)$$

which is shown at the left in Figure 2.5a.

For large values of K (K > 2.973) interference can occur in the range $\pi < \phi < 3\pi/2$ where the lower loops of the prolate cycloids in Figure 2.5b intersect each other; but such large values of K are outside the expected range of the flying hot wire.

As a practical matter in the calibration of hot wires, K was kept less than 0.5, thereby avoiding wake interference over most of the upper half revolution and also putting the useful changes in α ($-45^{\circ} < \alpha < 45^{\circ}$) in the upper part of the probe arc. Experimental evidence indicates that wake interference in the upper half revolution is only important for frame numbers less than 35.

2.5 The Phase-lock Servo

It was considered essential that the speed of the flying hot wire be held very constant, even in the face of the rather large torque disturbances exerted by the flow. Large torque changes on the order of 70-110 newton-cm at twice the rotation frequency of the rotor occur when the arms move from a position where they are aligned with the flow ($\phi = 0$) to a position where one arm is up moving against a large relative velocity of 4000-5000 cm/sec. A phase-lock servo was developed to satisfy this requirement. In essence, a phase-lock servo is a phase-lock loop where the VCO has been replaced by a DC motor which acts as a mechanical low pass filter whose time constant is determined by its inertial load. Phase-lock servos have traditionally been used to control low inertia loads such as tape drives, and the large inertia of the flying hot wire (14 newton-cm-sec) presents something of a problem from the standpoint of both stability and the power required to precisely control this mass.

Another troublesome feature of phase-lock loops is that they can lock on to harmonics of the input signal. It was felt that the phase-lock servo for this experiment ought to be designed to lock reliably at the desired frequency without a lot of adjustments or tuning; that is, operated by a single switch. To accomplish this, a feature was incorporated into the phase detector whereby a signal proportional to the error in frequency between input and output is added to the phase error signal. Lock is only achieved when both

errors are driven to zero.

Strictly speaking, a phase-lock servo is not a velocity servo but a position servo. A 256-tooth precision gear is used to encode the angular position of the DC motor. A magnetic pickup, Electro model 58405, senses the passage of a gear tooth past its pole piece as the shaft rotates. This particular model is equipped with a square wave output and gives a clean pulse train, 256 per revolution, as the shaft rotates. The 256-tooth gear is attached to the hub mounting flange, the edge of which has a single notch which is sensed by another model 58405 pickup, and serves as a one-pulse-per-revolution zero indicator (see Figure 2.2 for the location of the 256-tooth gear and notched hub mounting flange). The signal from the 256-tooth gear serves as the fedback input to the phase detector. The external control input to the phase detector originates as a 200 kHz signal coming from a preset counter in the data acquisition system. A series of decade up/down counters (SN74192) is used to divide this signal by a preselected number between 1 and 999. The phase detector compares this divided signal with the pulse train coming from the 256-tooth motor shaft encoder and produces an error signal proportional to the phase difference between the two. In the out of lock condition, this signal also contains a component proportional to the frequency difference, as described earlier.

The error signal is filtered by an active filter consisting of an operational amplifier hooked up like an analog integrator; that is, with an input resistor and feedback capacitor, but with an additional resistor in the feedback path in series with the capacitor.

This resistor serves to insert a lead term into the open loop transfer function, thus helping to stabilize the loop which contains two integrations. For the inertial load of the flying hot wire, the motor time constant is about 10 seconds. In order to maintain strong locking characteristics, the loop gain must be kept high. This requirement has the effect of making the motor look like a third integrator. In other words, with large loop gain, the inverse of the motor time constant is small compared to the unity gain crossover frequency of the open loop transfer function. Thus, it contributes nearly 90 degrees of phase lag at the crossover frequency. To stabilize the loop, a lead-lag compensation network was introduced between the phase detector and low pass filter, giving the open loop transfer function a stable phase margin of about 45 degrees at crossover. The output of the loop filter controls a power amplifier (model 800PRA built by Control Systems Research, Inc., capable of 50 volts and 20 amps of bipolar operation) which drives the motor.

A hardlocked servo like this controlling a large inertial load treats the DC motor rather harshly. The control signal to the motor has an AC component which is a fairly large amplitude sawtooth constantly pushing the motor hard forward and then hard back to maintain the position of the arms. The arms effectively filter this signal so that no undue motion is applied at the tip. However, under certain operating conditions, a resonance condition occurs which causes the motor to give off a high pitched whine. This resonance has an observable effect on the hot wire signals, but

it is not known whether the cause is mechanical motion of the wire or electrical noise induced by the resonating motor armature. This problem is not a serious one, and the rather narrow band resonance condition (encoder frequency ~862 ±50 Hz) is easily avoided. In practice, stable lock is achievable for rotor speeds of about 1-10 revolutions/sec up to a tunnel dynamic pressure of 15 lbs/ft^2 (3300 cm/sec).

In the locked condition the average speed of the arms is as stable as the frequency of the controlling oscillator. The instantaneous speed varies about one cm/sec due to torque perturbations from the flow.

2.6 The Intermittency Meter

Intermittency is a real property of turbulent flows; the turbulent interface is sharp enough so that points in the flow can usually be thought of as either turbulent or non-turbulent. Measuring this property is another matter, however, and usually tends to be a somewhat subjective process.

There is some advantage in using an x-array for this purpose, because when one wire is sensitive to velocity but insensitive to changes in angle, the other is sensitive to angle but insensitive to velocity. When a laminar-turbulent interface is encountered, one wire or the other should show it, no matter what the flow angle.

Figure 2.6 shows how intermittency is determined. The two hot wire signals are differentiated and then added. A bandpass filter is used to remove high and low frequency components. The

effect of the differentiators is to weight the higher frequencies within the band pass of the filter with a 6 dB/octave positive slope. The filtered signal is rectified and fed into a comparator with an adjustable level. The output of the comparator is a series of pulses of variable width whenever the input signal exceeds the comparison level. Each time the flying hot wire passes through turbulent fluid, a burst of pulses is produced. This is fed into a retriggerable one shot whose output stays high as long as the time interval between input pulses is less than the selected pulse width of the one shot.

One of the sources of error in this circuit is that when the sensor leaves the zone of turbulence the retriggerable one shot remains on for a time equal to its preset pulse width (about 0.5 milliseconds). There is probably no way to correct the data for this error, since the intermittency signal was only sampled at intervals of about 1 millisecond.

Figure 2.6 also shows typical hot wire traces from two wires of the same x-array in the wake of the cylinder. The corresponding intermittency output is also shown. In this picture, the voltage E3 has been added to the intermittency signal in order to show clearly when the hot wire signal causes the intermittency meter to change state.

2.7 The Vortex Trackers

The phase of the vortex shedding was sensed by a fast sensor (Pitran model PT-L2) measuring model surface pressure. Another source of phase information was an inclined hot wire located above

the wake of the cylinder about 16 diameters downstream. Both signals were bandpass filtered, and the resulting signal was tracked by a phase-lock loop (NE 565) whose center frequency was set to the expected vortex shedding frequency (~ 37 Hz). During the experiment, the shedding signal very rarely exceeded the tracking range of the phase-lock loops (25-50 Hz). A ramp signal synchronized with the vortex shedding was produced by amplifying the square wave output of the phase-lock loop and using its positive edge to discharge the feedback capacitor of an analog integrator whose input was a constant voltage. The hot wire and Pitran ramps were sampled along with the wake hot wire signals and combined into a single computer word before being recorded.

2.8 Data Acquisition and Instrumentation

Six channels of constant temperature anemometry based on a design by Perry and Morrison (Ref. 8) were built for this experiment. Minor changes were made to modernize the circuit with new, low drift, fast response, uncompensated amplifiers (Precision Monolithics OP-05). Modified Disa 55A38 x-array hot wire probes were used for the measurements.

Data taken during the cylinder experiment fall into three categories:

i) Calibration and benchmark runs - These runs were made with the horizontal traverse at 522 mm and the vertical traverse at 36 inches (the highest position). During calibration runs, the cylinder was removed and tunnel dynamic pressure (Q_∞) and arm tip speed (ωR) were varied.

Benchmark runs were made with the cylinder installed and served as a check on the wire calibrations. For both types of runs, data were retained over all 128 frames of the upper half revolution.

ii) Wake data runs - These runs consist of phase related data in the wake of the cylinder with the traverse at various positions (Figure 3.3). Data were retained at 78 frames in the upper half revolution.

iii) Runs with the arm not rotating - These are miscellaneous runs which were made to measure such quantities as model surface pressure, tunnel dynamic pressure along the calibration arc, etc.

The central element in the instrumentation is a computer data acquisition system. Data are digitized by a 16-channel Preston A/D converter (ADC) with a resolution of 14 bits plus sign, capable of conversion rates as high as 500,000 words/sec on one channel. The computer is an HP 2100 minicomputer with a disc operating system and 32K of core memory. The basic computer word is 16 bits (including sign). Data from the ADC are left-justified in memory, leaving the last bit available as a comment bit. Data are written on magnetic tape in phase encoded format with a density of 1600 bits per inch. The entire system is mounted on air bearings which allow it to be easily moved from one experimental site to another where it may be used by a single person running an experiment. Hence the name "Solo System".

Data from the ADC are processed in the computer by one

of three available programs, one for each of the previously listed categories. Each of the data acquisition programs is a self-contained stand-alone program which does not require the system for its operation, and hence can utilize the full core in order to efficiently meet the rather severe data requirements of the flying hot wire.

Data acquisition is slaved to the position of the flying arm by using, as the fundamental time base for the experiment, a signal which originates in a magnetic pickup (Electro model 58405) mounted in close proximity to a 256-tooth precision gear on the rotor shaft (Figure 2.2). The output of the magnetic pickup is a square wave encoder signal which serves two essential purposes. The first is to provide the feedback position signal required by the phase-lock servo which drives the flying arms at a constant speed. The second is to control the timing and position of the hot wire measurements.

The circular trajectory of the flying hot wire has a nominal diameter of 151.3 cm and a circumference of 475.3 cm. Therefore, digital data are acquired at 256 points (frames), spaced 1.85 cm apart, around the arc. This spacing was felt to be sufficient for resolving the shape and structure of vortices having a size comparable to the 10.137 cm diameter of the cylinder. It was decided early on that data from the lower half revolution where the arm passes the streamlined strut would be of no use. Therefore all recorded hot wire data are restricted to frame numbers 1-128. Phase related data are restricted still further to a set of frames in the upper half revolution specified by two program parameters,

NSAVE and NSKIP.

For a given x-array, the two hot wire voltages are measured 5 μsec apart. This time interval corresponds to a difference in probe position of about 0.2 mm, which is negligible, especially as the frequency response of the hot wires (20 kHz) limits the resolution of the wires to fluctuations having a period greater than 50 μsec.

Appendix A gives further details about data acquisition and control.

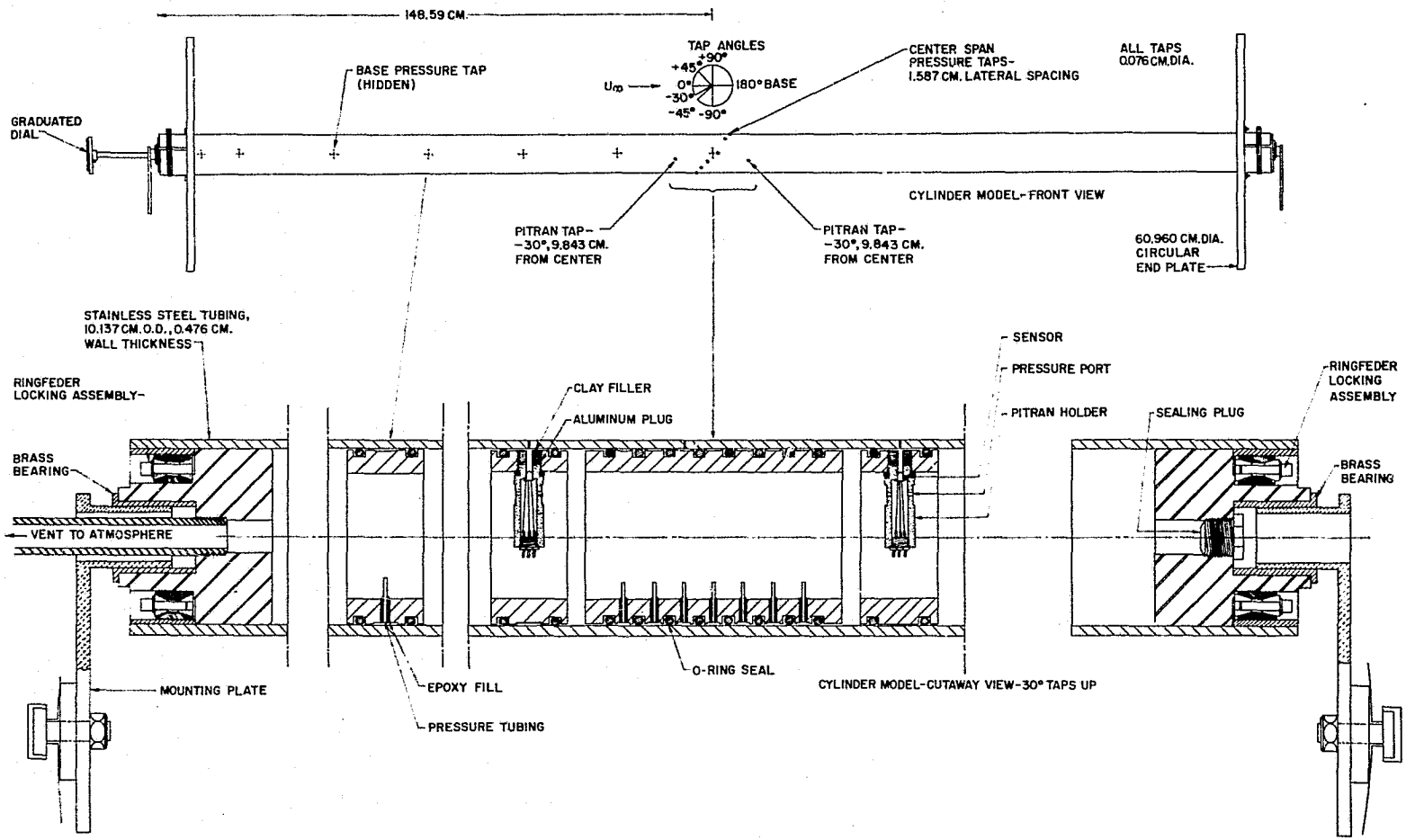

Figure 2.1 A detailed drawing of the cylinder model

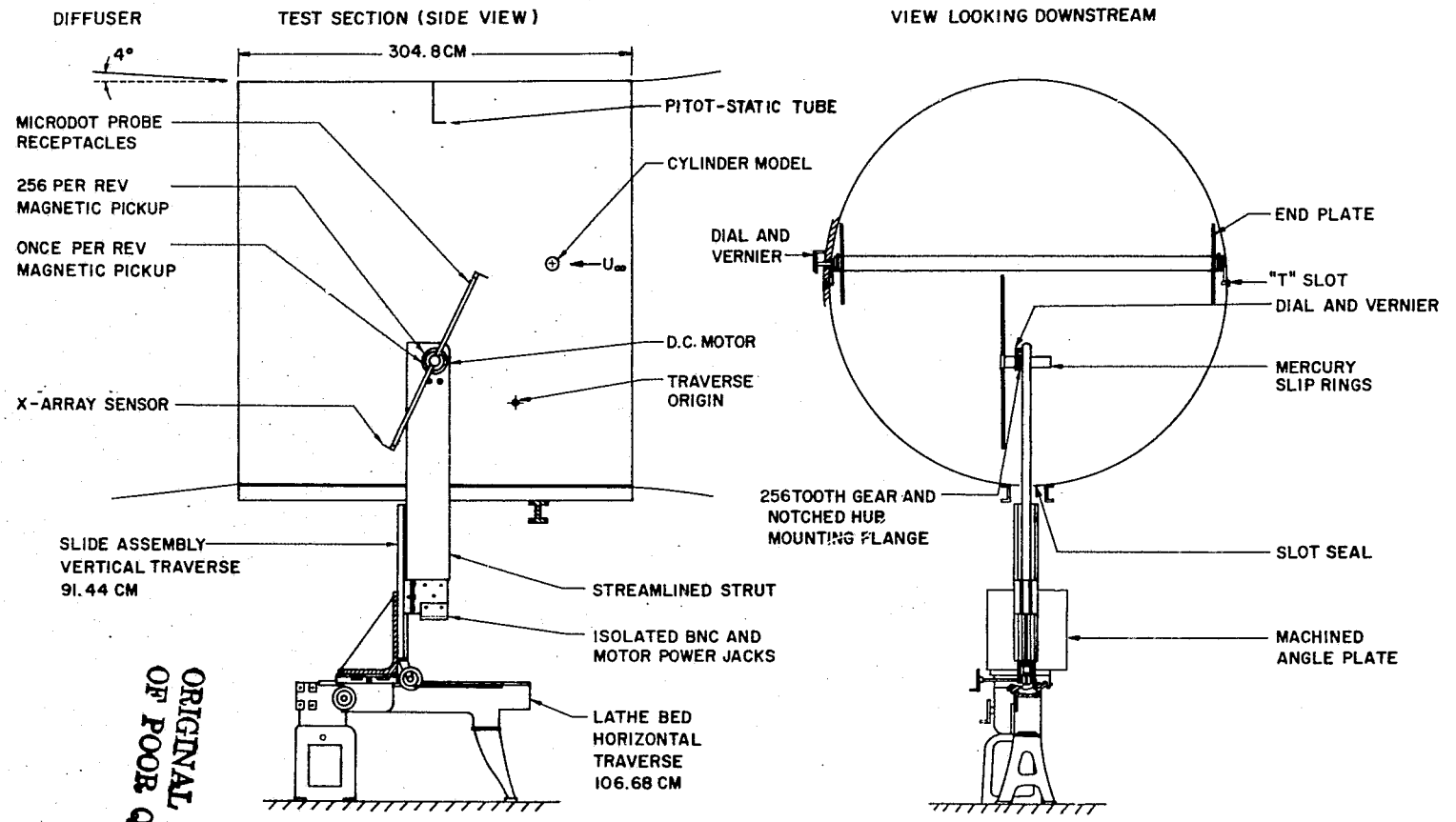

Figure 2.2 The configuration of the flying hot wire apparatus in the GALCIT 10-foot wind tunnel.

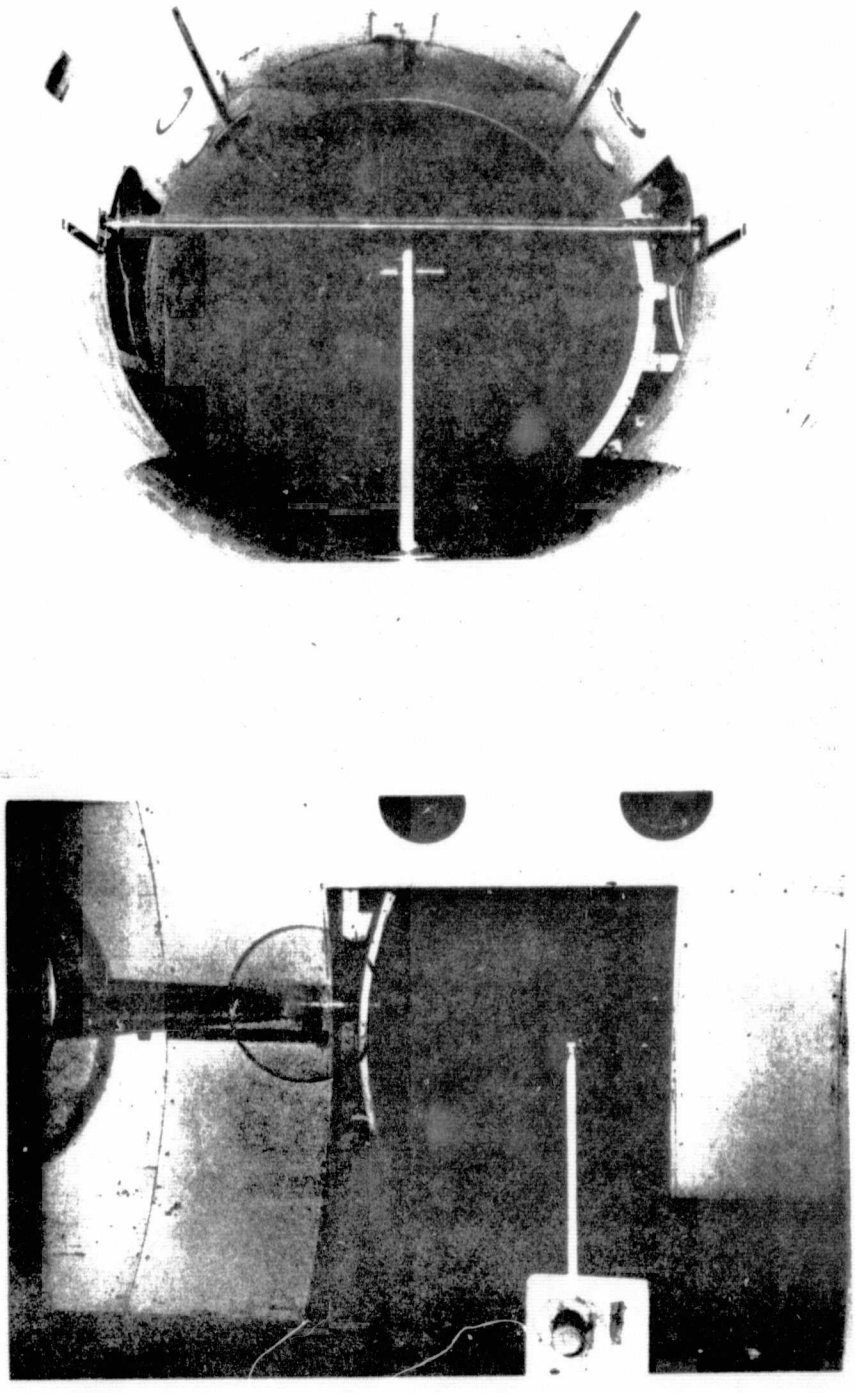

Figure 2.3 Two photographs of the flying hot wire apparatus. The view from the side shows an x-array probe and holder. The view looking downstream shows the cylinder model.

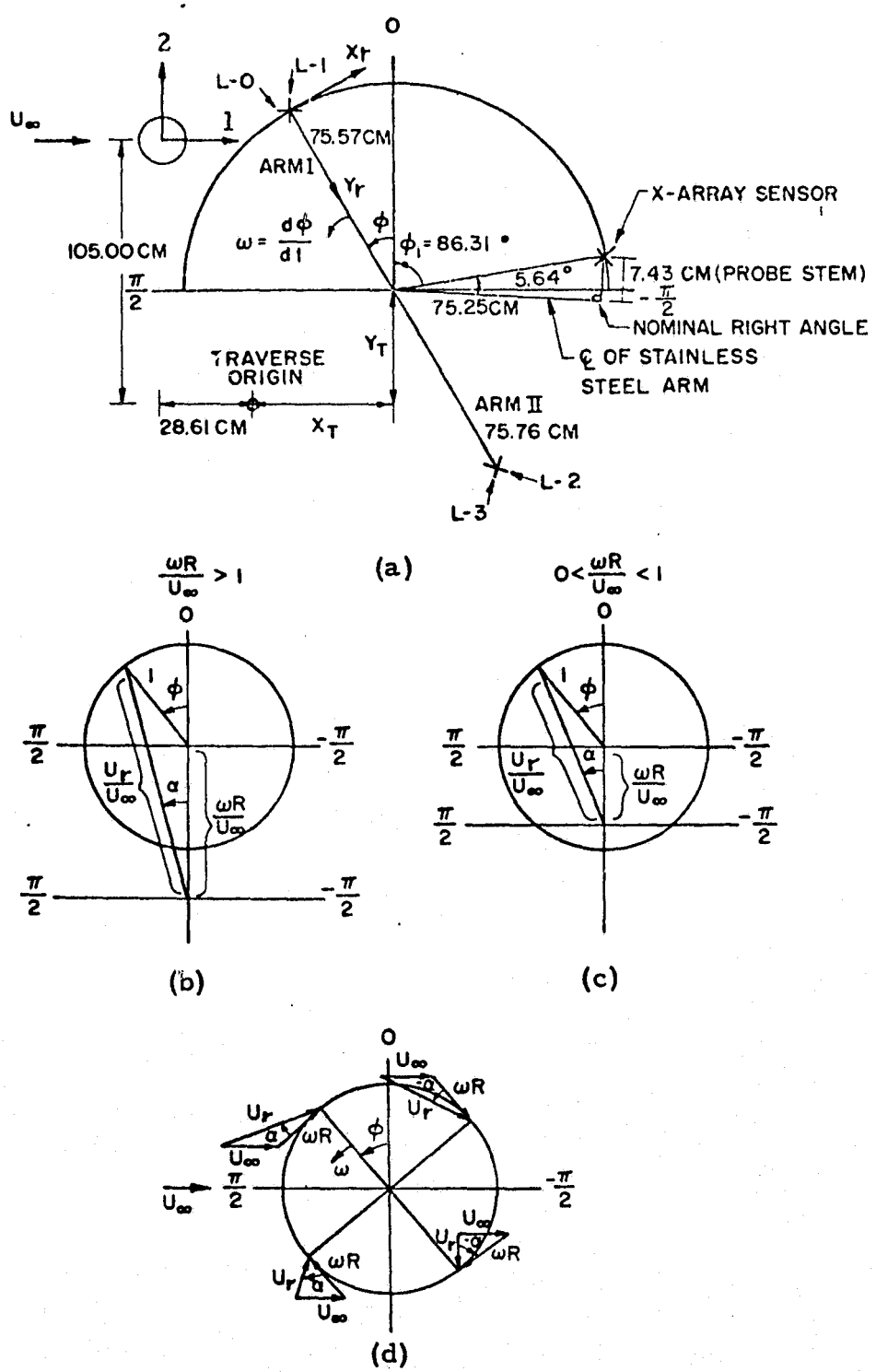

Figure 2.4 The geometry of the flying hot wire and constructions of the relative velocity vector.

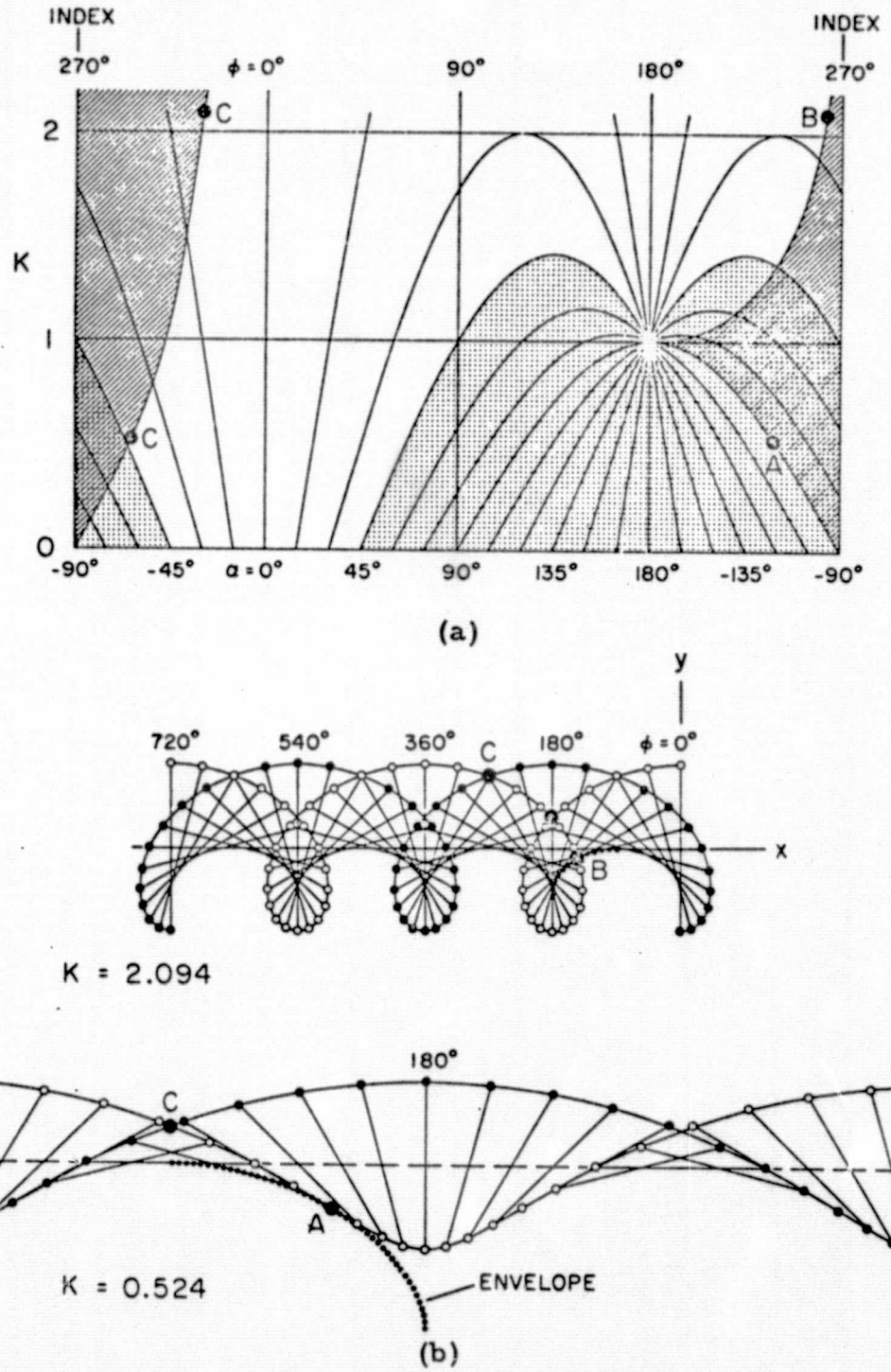

Figure 2.5 A plot of a) lines of constant flow angle, α, for various ϕ and K with regions of probe interference indicated; (dot shaded regions indicate where the relative flow angle is $\geq 45^{\circ}$ and slant shaded regions indicate probe interference) b) the cycloidal trajectory traced out by the rotating arm at two values of K.

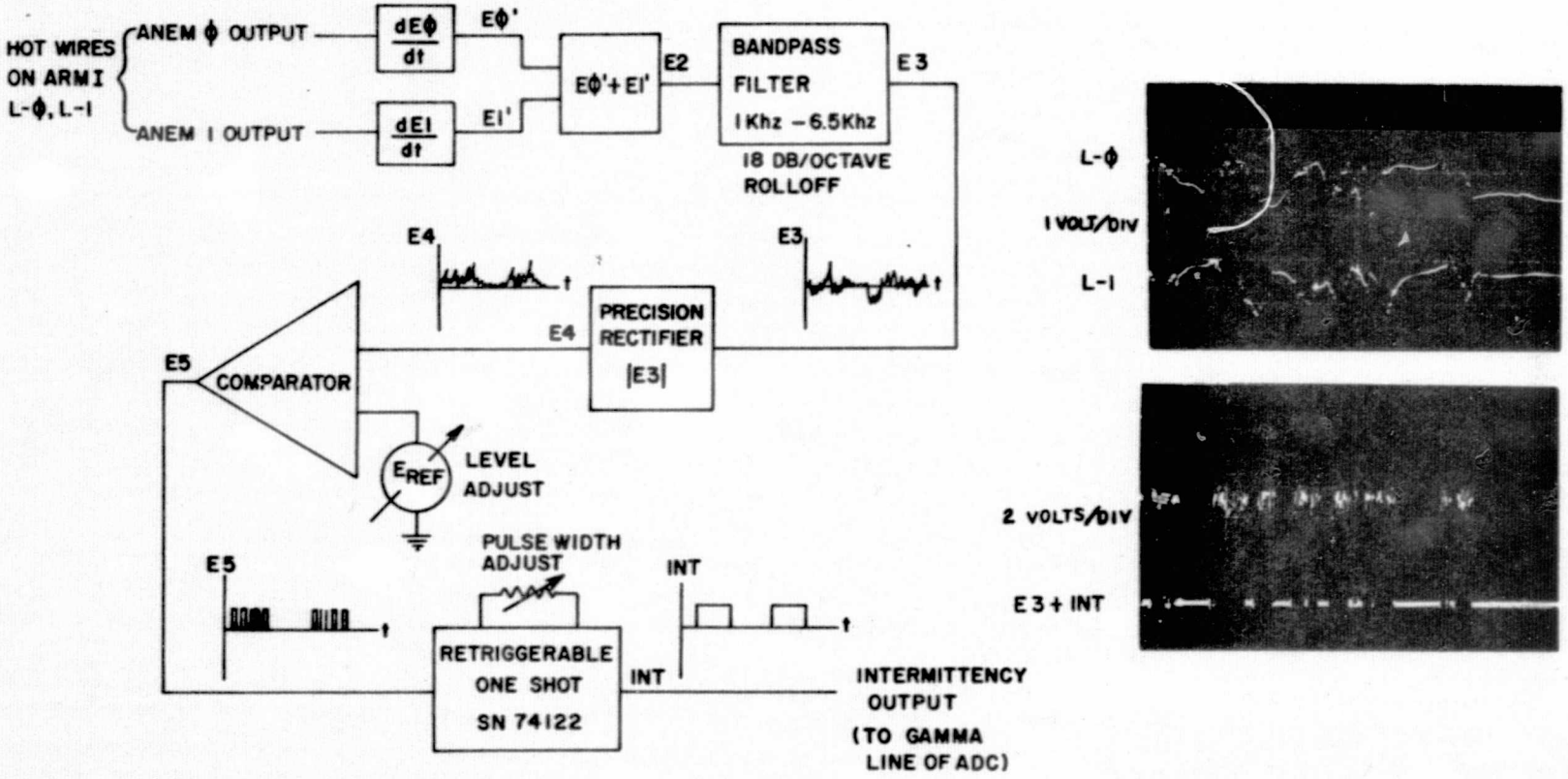

Figure 2.6 A diagram of the intermittency meter with typical input and output wave forms.

III. THE EXPERIMENT

3.1 Tunnel and Apparatus Configuration

Figure 2.2 indicates the configuration of the flying hot wire apparatus in the GALCIT 10-foot wind tunnel. The cylinder was located with its center 15.24 cm above the centerline and 60.96 cm downstream of the leading edge of the test section. No unusual procedures were used to prepare the wind tunnel for the cylinder experiment and no attempt was made to use screens or other devices to improve the quality of the free stream flow. The free stream turbulence level ($\sqrt{\overline{U''^2}}/U_\infty$) under these conditions was found to be less than 0.6 percent.

The streamlined strut and flying hot wire assembly protruded into the test section through a sealed slot along the floor. The strut was attached to the two-dimensional traverse which was in turn bolted to the concrete floor below the test section. Tufts were attached near the leading edge of the cylinder end plates to look for areas of separated flow. None were observed.

The zero position of the rotor was determined using a level and an Optron proximity sensor (model OPB 253) on arm I. This device consists of a light emitting diode (LED) and a photo transistor mounted in a flat plastic case in the shape of a trapezoid. The LED and phototransistor axes are aligned along the two non-parallel sides of the trapezoid. The two optical devices illuminate and view along lines which intersect about a quarter of an inch from the light source. When a reflective surface is moved toward the read head, the output voltage peaks as the surface reaches the intersection and

falls off as the distance to the surface is further decreased. Using the level, the arms were set in a horizontal position. With arm I downstream, the vertical traverse was used to move the optical read head past a strip of dull black tape with a narrow slit which exposed a thin section of reflective tape underneath. When the output was a maximum, the vertical traverse was locked in position, and the arms started rotating. With the arm rotating at an encoder frequency of 1026 Hz (thumbwheel divide switch set at 195), the peak in the Optron output (corresponding to the horizontal position of the arms) occurred 2333 μsec after the positive edge of the zero pulse. The first positive edge of the encoder pulse occurred 930 μsec after the zero pulse, i.e., 1403 μsec before the arms are horizontal. Thus, taking probe offset into account, the first frame of data occurs when the probe angle $\phi_1 = -86.31^\circ$ (see Figure 2.4a).

Table 1 indicates ADC channel assignments. ADC channel 4 was hooked up to a voltage standard throughout the experiment. The standard was set at 5.000 volts and served as a check to see if the data acquisition system was functioning properly. In the months following the experiment, this standard served as a valuable tool for diagnosing several isolated anomalies in the data. A Pitot-static tube attached to the ceiling of the test section measured tunnel static and dynamic pressures. An electronic thermometer measured tunnel temperature. The data system averaged these quantities over each revolution of the flying arms. During the experiment, the horizontal traverse was read in millimeters; the vertical traverse, however, was read in inches since the dial on

the Gilman slide assembly was graduated in the English system.

3.2 Measurement of Flow Properties

Pressures were measured in the cylinder experiment using two Barocel electronic manometers. Model 511 sensors with a range of 0-100 mm Hg were used. The manometers have a full-scale output of 10 volts and are linear to better than 0.5 percent over a wide dynamic range.

Tunnel dynamic pressure was measured using a pitot-static tube fixed midway along the ceiling of the test section and protruding about twelve inches into the airstream.

Throughout the experiment, the atmospheric pressure, P_{atm}, and wet and dry bulb temperatures were recorded at least once a day. Wet and dry bulb temperatures are used to find the vapor pressure of moisture in the air, H, which tended to remain fairly close to 10 mm Hg.

The recorded atmospheric pressure varied much more than expected. This variance was probably the result of faulty barometer readings by an inexperienced technician. These data were discarded, and the atmospheric pressure recorded by the tower at Los Angeles International Airport was used after corrections were made (assuming an adiabatic atmosphere) for the altitude difference between LAX and the 10-foot wind tunnel.

Tunnel static pressure, P_∞, which was always slightly below atmospheric pressure, was taken from the static port on the pitot-static tube used to measure Q_∞. Tunnel temperature, T_∞, was measured using an electronic thermometer (National model LX5606)

mounted on the wall of the test section, close to the centerline, approximately 35 cm forward of the downstream edge. During wake data runs when Q_∞ was held at 5 lbs/ft^2 (see footnote, p. 9), T_∞ tended to vary less than one degree away from a typical value of 24°C. The largest temperature changes, on the order of several degrees centigrade, occurred during calibrations. These variations were caused by the power input to the flow by the fan at increased values of Q_∞. The worst-case temperature changes were about 5° C and represent changes in viscosity of about 1.3 percent and changes in Reynolds number on the order of 3 percent.

3.3 Choice of Tunnel Speed, Arm Speed and Reynolds Number

A variety of different considerations entered into the choice of Reynolds number for the final test condition of the cylinder experiment. The most important consideration was to keep well below the critical Reynolds number so that the boundary layers on the cylinder would remain laminar up to the final fluctuating separation point. This condition contemplates the eventual use of the data as a test case for advanced calculation codes. Once this condition was imposed on the experiment, other factors then entered into the decision. For a given model size, chosen to be compatible with the size of the tunnel, high speeds are preferred. On the other hand, a high tunnel speed leads to difficulties with hot wire breakage, with decreased wire sensitivity, and with large dynamic loads and/or deflections of the model or the flying arm or both.

Another consideration was the need to calibrate hot wires at low speeds. The best adjustment of the fan blades allowed stable

operation in the range of velocities from 600 to 4000 cm/sec (dynamic pressures from 1/2 to 20 lb/ft^2 (see footnote, p. 9)) but not at lower velocities. The minimum locked tip speed of the arm was about 450 cm/sec, so that the minimum relative velocity of the flow at α = 0 (top dead center) was about 1400 cm/sec. The effect of this limitation was to influence the decision as to cylinder Reynolds number toward a high value in order to bring the range of expected relative flow velocities within that covered by the calibration.

A high rotation rate for the flying arm means decreased hot wire sensitivity, increased disturbance of the basic flow, increased interference from the wake of the leading arm, higher dynamic loads, and less time for on-line data processing. Depending on tunnel speed, demands on the phase-lock loop servo system which drives the rotor may become severe at high rotor speeds. In practice, the speed range available in still air is from about 50 rpm to about 700 rpm (tip speeds from 370 cm/sec to 5300 cm/sec). The lower limit is determined in part by dropouts in the ENCODER pulse train that occur when the gear teeth pass the magnetic pickup too slowly. The upper limit is determined by available power. This range is shortened, mainly at the upper end, when the tunnel is running. The inability of the bipolar servo power amplifier to provide adequate power when the torque is high may cause loss of lock.

A small ratio of tip speed to tunnel speed K minimizes contamination of the flow by the wake of the preceding rotor arm

and simultaneously moves the useful pitch-angle range (relative flow direction less than ±45 degrees) toward the top of the rotor arc. This effect is desirable during wire calibrations, although it makes the achievement of a large speed range more dependent on low-speed tunnel operation. Both the upper and lower limits on tunnel speed are determined by the fixed blade setting for the tunnel fan, and operation near the lower limit is subject to poor speed regulation of the fan motor. During the actual measurements in a turbulent flow, on the other hand, a larger value of K is desirable, because it minimizes the probability that the instantaneous pitch angle in regions of high turbulence level will be outside the range of sensitivity of the wires.

One of the most important considerations in the choice of cylinder Reynolds number was the regularity of the vortex shedding process. Tunnel Q_∞ was varied over a wide range, and the Pitran sensor was positioned at several angles to the flow. In general, the signal is relatively clean, with the amplitude of the time varying part increasing as the angle is varied away from the forward stagnation point (cylinder angle equals 0^o). For angles larger than about 80^o, the signal becomes fairly noisy due to turbulence in the separated zone (see Figure 3.1). Throughout the range of conditions observed, the signal was characterized by a considerable amount of amplitude modulation. This modulation may be due to three-dimensional effects which occasionally give rise to a condition more akin to buffeting than vortex shedding. Whether this condition was caused by the finite length of the cylinder (perhaps a periodic

variation in the correlation length of the vortex shedding) or is a fundamental aspect of the flow is unknown. The condition becomes more accentuated as the Reynolds number is increased. Above a Reynolds number of 200,000 the amplitude modulation begins to take on the character of discrete jumps in the DC level of the Pitran voltage (upper left, Figure 3.1) The flow at this Re may be jumping between two states representing subcritical and supercritical pressure distributions, lingering longer and longer periods of time in the supercritical state as the Reynolds number is increased.

For the wake measurements the Pitran sensor was positioned 65^{o} away from the forward stagnation point. Some of the low frequency modulation and noise was removed with a bandpass filter before the signal was put into the vortex tracker. The active volume of the Pitran pressure port was small, 0.07 cm^3, and linearity of the transfer function between pressure and voltage fluctuations was checked by the constancy of $\sqrt{\overline{E_p'^2}}/Q_\infty$ at several values of Q_∞ (shedding frequency).

Figure 3.2 shows measurements of the mean pressure profile around the cylinder at various Reynolds numbers in the range from 50,000 to 300,000. Evidence of the critical Re drag crisis begins to appear at Re = 239,000. The pressure profile shown by solid points in Figure 3.2 represents the operating condition finally chosen for the wake measurements. The Reynolds number based on cylinder diameter (10.137 cm) and tunnel velocity (2120 cm/sec) (uncorrected for blockage) was about 140,000 (ν = 0.1535 cm^2/sec at a T_∞ of 24^{o}C). The Strouhal number was equal

to 0.179 (shedding frequency 37 Hz) and the drag coefficient was 1.227.

3.4 Hot Wire Calibrations

The operating point of the hot wire anemometers was set by whirling the arms at a high velocity with the tunnel off so that the speed relative to the sensors fell in the middle of the range of expected velocity fluctuations (encoder frequency 2127 Hz, 8.3 revs/sec - tip speed, approximately 4000 cm/sec). An internal square wave was used to optimize the damping and frequency response. The bandwidth inferred from this test was usually around 20 kHz.

The probe used in this experiment was a modified version of the DISA 55A38 miniature x-array probe.* The wire was platinum plated tungsten 5 μm in diameter. The temperature coefficient of resistivity of this material, σ, is approximately $0.0036^{\circ}C^{-1}$. The overheat ratio (the ratio of hot to cold resistance of the wire R_w/R_∞) used for the measurements was about 1.45. Wire temperature is computed using

$$T_w = T_\infty + \frac{1}{\sigma}\left(\frac{R_w}{R_\infty} - 1\right) \quad . \tag{3.1}$$

R_∞ is the resistance of the wire at the reference temperature T_∞.

---

*Hot wires were labelled as follows. Referring to Figure 2.4a, wire L-ϕ (last channel minus ϕ) is the wire on arm I which is exposed to nearly normal flow at $\phi \sim -90^{\circ}$. Wire L-1 (last channel minus 1) is the one exposed to nearly normal flow at $\phi \sim +90^{\circ}$. Wire L-2 is on arm II oriented like L-ϕ. L-3 is oriented like L-1. ADC channel assignments (Table 1) were as implied by the labels.

Table 2 lists the various hot and cold wire resistances and temperatures used in the experiment.

Several probes were calibrated during the experiment and a system was adopted for labelling probe sets. All four wires constitute a wire set. For example, if wire L-2 of wire set 3 breaks and the probe on arm II is replaced, then this and the old, still unbroken probe on arm I are renamed wire set 4. Calibrations were labelled such that the first calibration of wire set 5 would be 5-1, the second 5-2, and so on.

All calibrations were carried out with the tunnel empty, the x-traverse at 522 mm and the y-traverse at 36 inches. Benchmark runs were made with the cylinder installed and the traverse in the same position, and served as a periodic check on the calibration.

Q_∞ and ωR (arm tip speed) were varied during the calibrations in such a way as to give approximately uniform increments of the square root of the relative velocity at $\alpha = 0$, while maintaining a K less than 0.5. This increases the density of points on the upper part of the King's law curve, where the sensitivity of the wires starts to fall off, and errors are most critical.

The resonance condition mentioned in section 2.6 (phase-lock servo) was observed during several calibrations when the thumbwheel divide switch was set to 232 (arm speed 3.37 revs/sec). Data taken at this setting were later discarded.

3.5 Wake and Calibration Data

Wire sets 1, 2, and 3 all broke before any useful data could be taken with them. All the wake data were taken with wire sets 4 and 5.

Wires L-2 and L-3 of wire set 4 broke during calibration on tape 11. However, the decision was made to continue to take data with just two good wires since they were the only two left at the time. As it turned out, the data on tape 11 had to be discarded due to a hardware problem with the ADC. This is not serious, however, since tape 30 contains a fairly extensive set of benchmark runs with wire set 4. In addition, tapes 12, 14, 16, 18, 20, and 22 also contain benchmarks. See Table 3 for a list of the data tapes produced during the experiment.

Wire set 5 was calibrated on tape 31 and again on tape 59. In addition, tapes 35 and 58 contain fairly extensive benchmarks.

The program used for calibration and benchmark runs saved the hot wire data over all 128 frames of the upper half revolution.

Wake data is contained on tapes 12-29 (wire set 4) and 31-57 (wire set 5), with each tape devoted exclusively to only one trajectory. Figure 3.3 indicates the trajectories used in the experiment with their corresponding tape numbers. All the wake data was taken with NSAVE equal to 78. NSKIP varied from tape to tape as indicated in Figure 3.3.

The data volume was not a free parameter of the experiment. A reasonably smooth variation of mean velocity can be

obtained with a population of perhaps 500 samples. An acceptable dispersion in products of velocity fluctuations, however, requires a larger population of perhaps several thousand samples. In the cylinder experiment an early decision was made to divide each vortex shedding cycle into 16 phase intervals, and to accumulate a sufficient population of samples in each phase interval, so that dispersion would be small (1 %, say) in the mean velocities and intermittency, moderate (5%, say) in the double velocity correlations and at least acceptable (25%, say) in the flatness factors and triple velocity correlations.

In practice, with two wire arrays working, the flying arm made 16,384 revolutions, yielding two independent populations of 1024 samples per frame and phase (about 1 hour of tunnel time; about 1400 feet of tape in 4 data files of 4096 revolutions each). If only one wire array was working, data were recorded for 24,576 revolutions to obtain a single population of 1536 samples (about 1.5 hours of tunnel time; about 2100 feet of tape in 6 files of 4096 revolutions each). There were 27 tapes of the first kind and 18 of the second kind. The data base therefore includes about 103,000,000 voltage pairs or velocity vectors. Also recorded were about 170,000,000 words of phase information and perhaps 60,000,000 words of hot wire calibration data, pressure data and miscellaneous information. The total data base is therefore about 435,000,000 computer words.

All wake data were taken with the thumbwheel switch dividing the 200 kHz control signal to the phase-lock servo set to 172

(encoder frequency 1162.79 Hz, average tip speed 2159.56 cm/sec).

Figure 3.4 shows a photograph of typical hot wire traces during one full revolution of the arm. The leftmost part of the picture corresponds to $\phi = -90^{o}$ with the sensor in the wake of the hub. It moves up through the hub wake, into the free stream, then into the cylinder wake where it encounters several vortices, then out and down, through the flow disturbance of the strut.

Table 3 lists the data by tape number along with the associated program type, x_T and y_T traverse positions, and nominal tunnel Q_∞ setting.

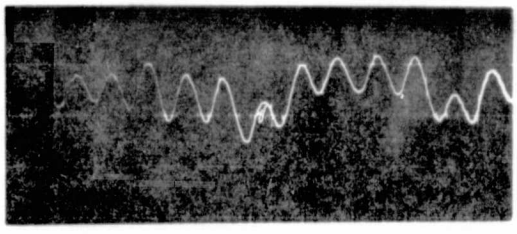

Pitran tap at 30°
unfiltered
dynamic pressure - 15 lbs/ft^2
horizontal - 20 ms/div
vertical-- 0.1 volts/div

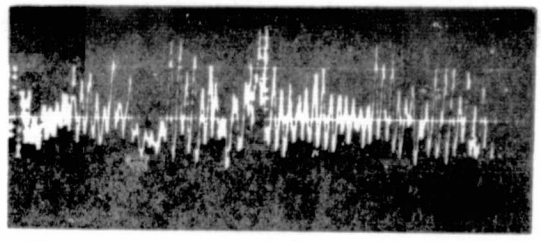

Pitran tap at 150°
unfiltered
dynamic pressure - 15 lbs/ft^2
horizontal - 100 ms/div
vertical - 0.1 volts/div

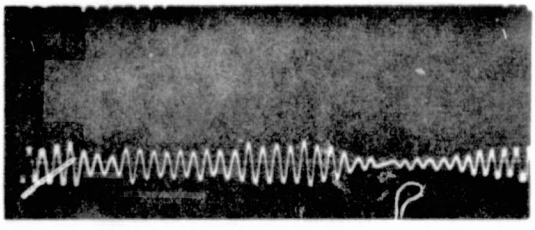

Pitran tap at 30°
filter 25-63 hz
dynamic pressure - 5 lbs/ft^2
horizontal - 100 ms/div
vertical - 0.02 volts/div

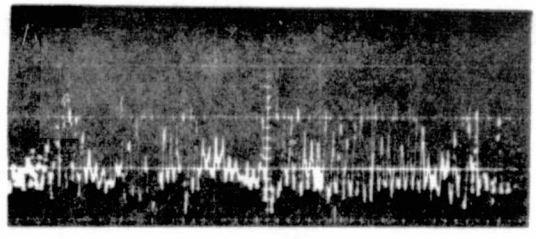

Pitran tap at 150°
unfiltered
dynamic pressure - 5 lbs/ft^2
horizontal - 200 ms/div
vertical - 0.05 volts/div

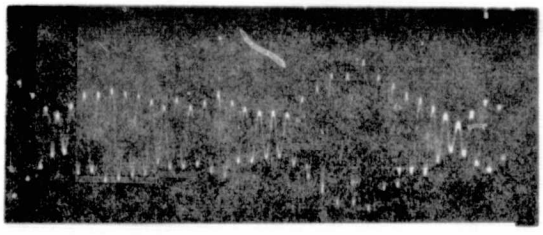

Pitran tap at 65°
unfiltered
dynamic pressure - 5 lbs/ft^2
horizontal - 100 ms/div
vertical - 0.02 volts/div

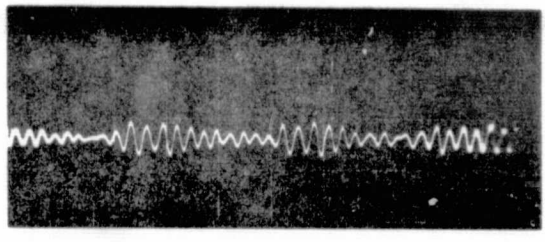

Pitran tap at 20°
filter 25-63 hz
dynamic pressure - 5 lbs/ft^2
horizontal - 100 ms/div
vertical - 0.02 volts/div

Figure 3.1 The Pitran surface pressure signal under various conditions.

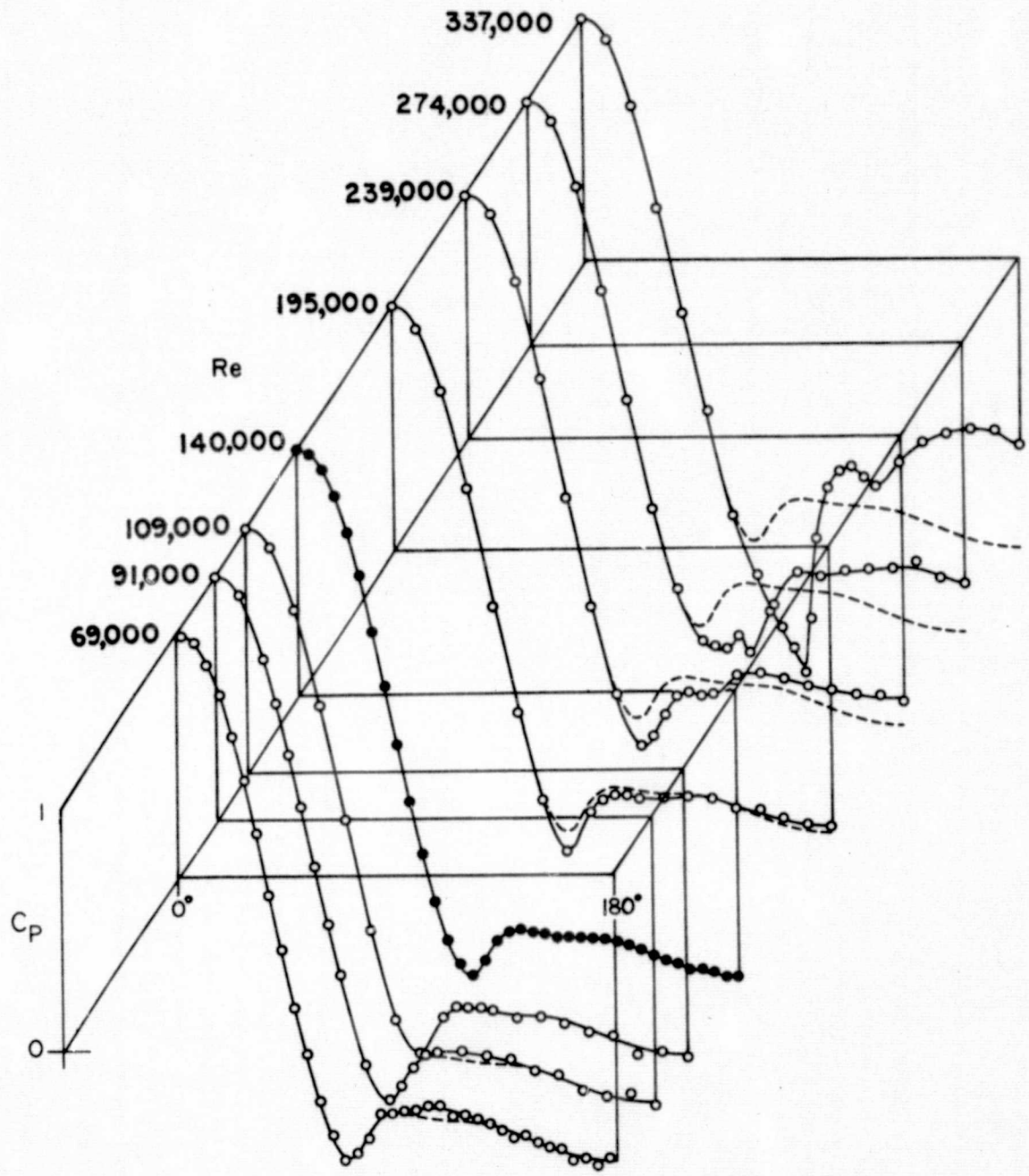

Figure 3.2 Model surface pressure distributions measured at various Reynolds numbers.

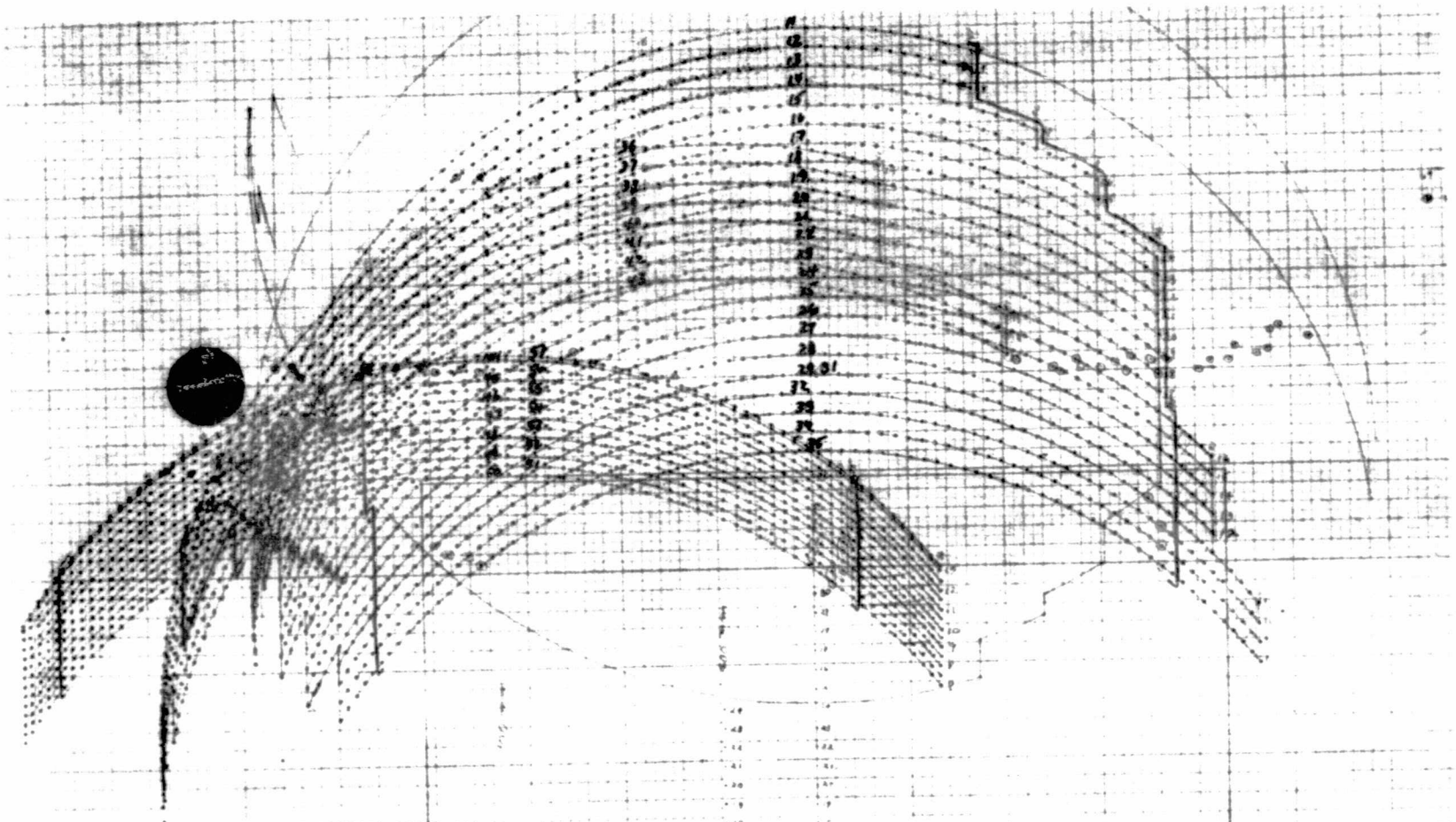

Figure 3.3 A diagram of the arcs along which phase related data were taken in the wake of the cylinder, with their associated tape numbers.

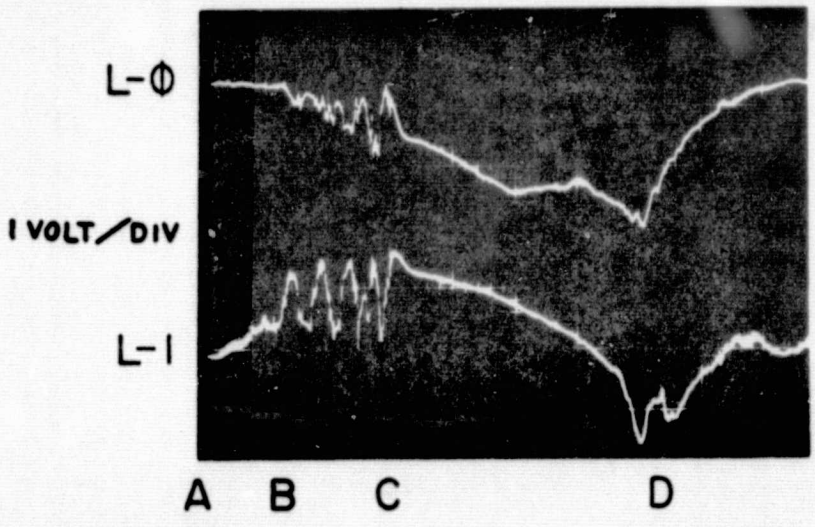

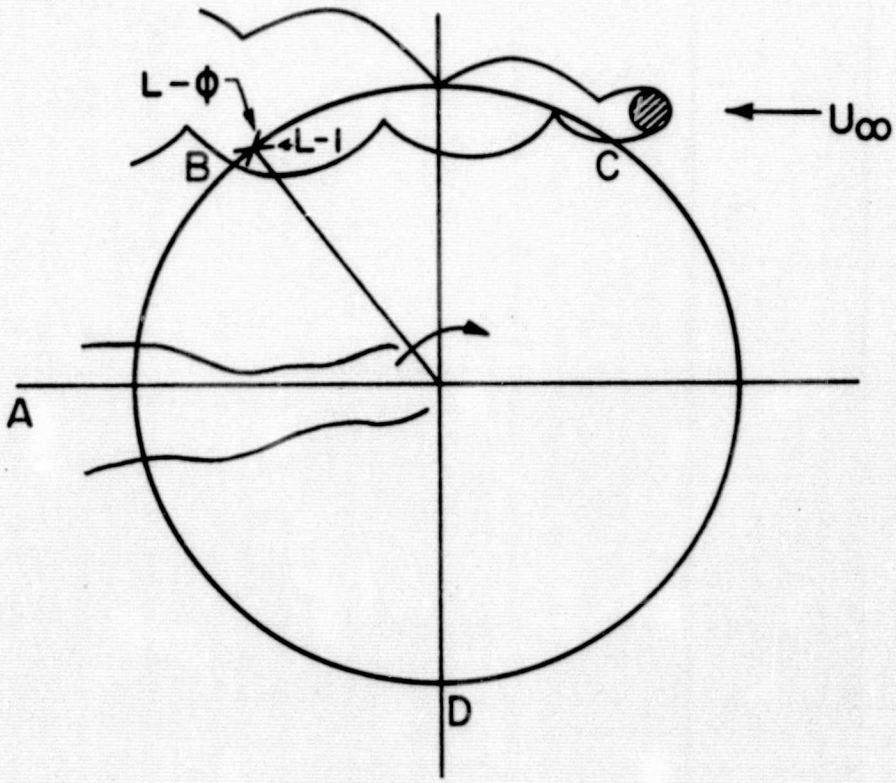

Figure 3.4 A photograph of signals from the two wires of an X-array during one full revolution of the whirling arms.

IV. THE REDUCTION OF DATA

4.1 General Comments about the Data

As described earlier, the total data base amounts to approximately 435 million words, about one third of which are hot wire signals in the wake of the cylinder. Most of the remaining words are the ramp signals and pressure and temperature data. The rest of the data consists of hot wire calibrations and other miscellaneous information.

In general, the quality of the data is very good. There are several parity errors on the tapes which are of no consequence. The first revolution of tape 22, file 7, has a format error which could have occurred if the $\overline{\text{HOLDOFF}}$ signal (see Appendix A) was already true when the run button was pushed to start the data file. Tapes 11 through 24 mistakenly had ADC channel 6 connected to cylinder tap #4 instead of P_{atm}-P_{∞}. The manually recorded value of P_{∞} was used to remedy this error.

Sometime after the cylinder experiment, as the data were being closely examined, it became apparent that there was an intermittent problem with the data acquisition. The Analogic voltage standard on channel 4 (last channel -7) was extremely useful in pinpointing when the problem occurred. On more than 95 percent of the files recorded, all of the maximum and minimum voltages sampled on the Analogic voltage standard (averaged over one revolution-256 samples) were within one count (0.3 mv) of 5.000 volts. Occasionally however, the Analogic voltage fluctuated wildly. When these fluctuations occurred, incorrect values were

also recorded on other channels. This problem occurred on tapes 12, 13, 17, 18, 25, 34, 38 and 48. It was possible to incorporate diagnostic procedures into the data reduction process in order to isolate and eliminate abnormal data and the data on all anomalous tapes have been salvaged.

Several months after the experiment the problem was finally traced to an intermittent hardware problem in the ADC.

4.2 Pressure Coefficients

All pressure results presented are nondimensionalized by the tunnel dynamic pressure measured by the pitot-static tube fixed to the ceiling of the test section, $Q_{\infty\,\text{fixed}}$. Units for the nominal tunnel dynamic pressure as set by the tunnel operator are reported in lbs/ft^2. Units for all other pressures are in mm Hg. No attempt was made to correct pressure coefficients for tunnel blockage effects, since this is, itself, a poorly understood problem for such a strongly Reynolds number dependent flow. Due to the small variation in Q_∞ across the tunnel, the pressure coefficients reported here are slightly high. For example, the pressure coefficient at the forward stagnation point of the cylinder is 1.019 instead of the ideal 1.000.

4.3 The Assignment of Phase Information to the Data

There were two sources of information about the phase of the vortex shedding cycle; the Pitran sensor responding to model surface pressure, and an inclined hot wire located 16 diameters downstream of the cylinder, 3 diameters above the wake centerline.

Figure 4.1 shows photographs of the Pitran signal with its associated (synchronized) ramp. The peak voltage of the ramp depended on the cycle time of the vortex shedding and tended to stay between 5 and 8 volts during the experiment. At a shedding frequency of 37 Hz and an encoder frequency of 1163 Hz, the number of frames (or samples) per shedding cycle averaged around 31.

The two ramps, combined into a single computer word, were recorded over the entire revolution, giving a continuous time series over each data file. Combining the two ramps into one computer word (see Appendix A) reduced the resolution to 1 part in 128, which is more than sufficient to resolve the phase to 1 part in 16.

Figure 4.2 shows how the phase was computed from ramp data. Each ramp considered as a function of the frame number (equivalent to time since the speed of the arm was constant) was extrapolated to zero. The intercept or origin for the ramp cycle was defined to an accuracy of one octal place (i.e., 1/8 of the period between frames). The interval from one ramp origin to the next was divided into 16 equal sub-intervals, and a phase in the form of an integer (i.e. 1, 2, ----15, 16) was assigned to each frame between origins.

An initial pass through the data was made to determine the intermittency factor at constant phase from the last bit in the data words. The Pitran ramp was used without any attempt being made to modify, compensate or discriminate against data taken when the period of the vortex shedding cycle (ramp) varied widely away from the averge value of 26.65 msec. The results of this

operation on the intermittency factor were pleasing enough; however, the only area of the flow where the intermittency factor, γ, reached 1 was in the base region of the cylinder. Several operations to reduce the dispersion in the intermittency were attempted with the object of trying to approach $\gamma = 1$ in the middle of each vortex. The basic approach was to look for an optimum condition on the properties of the Pitran signal (which is present and statistically the same for all tapes). The result of this operation was that the simplest approach is the best. The best phase is that assigned according to the local state of the Pitran ramp at the time of each sample, regardless of the streamwise probe position. Some improvement is gained by restricting the acceptable length of the shedding cycle but not enough to offset the disadvantages of the accompanying decrease in sample population. The downstream hot wire gave substantially degraded results for γ when it was used to assign phases, and has essentially been discarded. All results presented in this thesis are therefore based on phases assigned using the Pitran ramp.

4.4 Hot Wire Calibration Procedure

Hot wires were assumed to follow King's law in the form of equation (4.1)

$$Nu = A' + B'(Re_{\perp})^{n} \qquad (4.1)$$

where Nu is the Nusselt number and $Re_{\perp}$ is the Reynolds number based on the component of fluid velocity normal to the wire.

If fluid properties (ρ, μ, k) are based on the wire temperature T_w and a linear dependence on $T_w - T_\infty$ is assumed, equation

(4.2) results;

$$\frac{E^2}{T_w - T_\infty} = A + B(U_\perp)^\eta \tag{4.2}$$

where E is the anemometer output in volts, T_∞ is the gas temperature in ^oC, and $U_\perp$ is the velocity component normal to the wire in cm/sec. Since the fluid properties are not part of the picture, the dimensioned quantity $E^2/\Delta T$ will still be termed "Nusselt number" for lack of a better phrase.

Referring to Figure 4.3, consider $U_\perp$ for two inclined wires.

$$U_{\perp o} = Ux_r \sin\beta_o - Uy_r \cos\beta_o = Ux_r \sin\beta_o (1 - \cot\beta_o \tan\alpha) \tag{4.3}$$

$$U_{\perp 1} = Ux_r \sin\beta_1 + Uy_r \cos\beta_1 = Ux_r \sin\beta_1 (1 + \cot\beta_1 \tan\alpha) \tag{4.4}$$

Substituting equations (4.3) and (4.4) into equation (4.2) and absorbing $(\sin\beta)^\eta$ into B one obtains the following:

$$N_o \equiv \frac{E_o^2}{T_{wo} - T_\infty} = A_o + B_o(Ux_r(1 + C_o \tan\alpha))^{\eta_o} \tag{4.5}$$

$$N_1 \equiv \frac{E_1^2}{T_{w1} - T_\infty} = A_1 + B_1(Ux_r(1 + C_1 \tan\alpha))^{\eta_o} \tag{4.6}$$

A, B, η and C are constants, around 0.2, 0.01, 0.5 and 1.0, respectively, which are independent of Ux_r and α. Rearrange equations (4.5) and (4.6) to form

$$G_o \equiv \left(\frac{N_o - A_o}{B_o}\right)^{1/\eta_o} = Ux_r(1 + C_o \tan\alpha) \tag{4.7}$$

and

$$G_1 \equiv \left(\frac{N_1 - A_1}{B_1}\right)^{1/\eta_1} = Ux_r(1 + C_1 \tan\alpha) \tag{4.8}$$

which are explicitly solvable for Ux_r and α (or Uy_r).

The technique for converting Nusselt number pairs (N_o, N_1)

to velocity pairs (Ux_r, Uy_r) used the measured data and equations (4.7) and (4.8) (with suitably determined calibration constants to produce a first approximation to (Ux_r, Uy_r). The final values of (Ux_r, Uy_r) were determined by applying a correction to compensate for systematic errors in the fit of equations (4.5) and (4.6) to the calibration data (See appendix C for additional details).

The most serious complicating factor in the calibration process came from changes in A and B resulting from hot wire drift with time. To compensate for drift, a technique for interpolating calibration constants between data tapes was adopted which relies on the self-calibrating feature of the flying hot wire and the fact that nearly all of the arcs used for wake measurement include substantial portions where the wires were well outside the turbulent flow. The result of this process was a unique set of calibration constants A, B, η and C for each data tape. These constants are listed in Table 6.

Generally, the calibrations listed in Table 6 give good results. Points where different trajectories cross give nearly the same velocity vector in most cases. The two independent x-arrays of wire set 5 yield results for the mean flow which are practically indistinguishable.

The only tapes which still show major disagreement are tapes 24 through 28. These trajectories lie almost entirely inside the wake (see Figure 3.3), and, therefore, the only frames which are not in the turbulent flow are at the extremities of the arc where the relative flow angle is severe.

4.5 The Sorting Operation and Inversion of King's Law via Lookup Tables for Ux_r and Uy_r

As mentioned earlier, the data base includes about 103,000,000 voltage pairs or velocity vectors. The approach to the data processing was predicated on the fact that there was never any serious intent to run through the inverse King's Law operation 103,000,000 times. It was necessary to develop methods which would reduce the data processing task by at least one order of magnitude while at the same time preserving the populations in sufficient detail so that further processing of the statistical data would be practicable. The purpose of this section is to give a general description of these methods.

The key to data compression is the use of a discrete lookup table for the inversion of the hot wire data. As already described, the basic data set for each data frame and phase is a population of 1024 voltage pairs for each of the two wire sets (or when only one set was working, 1536 wire pairs). In a highly turbulent region, the two squared wire voltages may vary by ±40 percent. A relatively coarse two-dimensional grid in Nusselt number space at, say, two percent intervals would be quite adequate for constructing a two-dimensional distribution in coordinates N_o, N_1 (or N_2, N_3 for wires L-2, L-3).

Expressed in terms of the thermometer output voltage (0.1 volts/^oC), (T_w-T_∞) would be equivalent to about 15 volts. E varies between 5 and 8 volts; therefore, $E^2/\Delta T$ varies from 2 to 7 volts, or when expressed in the integer ADC format (10 v range,

32768 least counts plus sign), is a number between 6000 and 21,000. The weight of the least significant bit (LSB) or least count is 0.3 millivolts. Thus, if an interval in N (0 or 1) represents 256 least counts (78 millivolts), then the range of N is measured by about 60 such intervals. Twenty-five intervals would be sufficient to cover a ±20 percent variation in N while providing ample resolution to define a one-dimensional distribution function. In two dimensions, (N_o, N_1), an array of 25 x 25 = 625 cells is adequate to contain a population of 1024 samples, and there is no need for finer resolution of a population which represents a highly turbulent flow. However, when the population represents a low turbulence region, finer resolution may be required to obtain acceptable values for moments of the distribution. Therefore, the procedure followed was to take a resolution of 256 least counts (78 millivolts) as standard. If the required array had fewer than 64 cells at this resolution, the resolution was doubled to 128 least counts (39 millivolts), and if the array still had fewer than 64 cells, the resolution was again doubled to 64 least counts (19 millivolts). Thus, the best obtainable resolution in $E^2/\Delta T$ is about 5 parts in 1000, corresponding to a resolution in voltage of about 2 parts in 1000.

Because the constants in King's law are different for each tape, the inversion of Nusselt number pairs (N_o, N_1) to velocity pairs (Ux_r, Uy_r) must proceed on a tape-by-tape basis. Obviously, each tape will contain a maximum and minimum measured value of $E^2/\Delta T$ for each wire for a given frame and phase. The minimums are truncated so as to be evenly divisible by 64 and are used to

form the origin of the array, labelled MIN0, MIN1 on three typical arrays shown in Figure 4.4. The maximums are used to define the dimensions of the array as well as the required resolution (256, 128 or 64 least counts). Any voltage pair measured at a particular frame with a particular phase can be assigned to a cell in the appropriate array by simply incrementing the population of that cell. The smallest value of $N_o = E_o^2/\Delta T$ ever measured on any tape at any phase and frame was 6784 (after truncation to an integer multiple of 64). The maximum N_o ever measured was 20352. For N_1 these numbers were 6400 and 19,456, respectively.

The King's law inversion was, therefore, performed only once for each tape by inverting the (N_o, N_1) pair corresponding to each node of a master array with an origin at (6784, 6400) and dimensions of 256 units (64 counts each) in N_o and 240 units (64 counts each) in N_1. This is an array which is large enough to contain any (N_o, N_1) pair ever measured, and thus, of course, will contain any pair on a given tape.

Due to the nonlinear relation between (N_o, N_1) and (Ux_r, Uy_r) the mapping of a square grid in (N_o, N_1) space onto (Ux_r, Uy_r) space will not result in a square grid in Ux_r and Uy_r. So in practice, the result of the King's law inversion of the master array is actually two arrays: a 256 x 240 array of Ux_r's and a 256 x 240 array of Uy_r's.

Since the coordinates (N_o, N_1) of the origin of each sorted array are multiples of 64, an array corresponding to a particular frame and phase for which the resolution was either 128 or 256

least counts will overlay the master array in such a way that the center of a cell of the smaller array will correspond to a node of the master array. The indices of the node then represent the address of the appropriate velocity components in the Ux_r, Uy_r arrays. For arrays with a resolution of 64 least counts, the corners of each cell correspond to nodes in the master array, and velocities assigned to the cell are computed by taking the average of the velocities at the four nodes. In fact, for arrays with resolutions of 256 and 128 least counts, velocities were computed by averaging the velocity corresponding to the central node with those corresponding to the four neighboring nodes. Averages and statistical information at each frame and phase are obtained via the table lookup procedure for velocities just described (the velocities Ux_r and Uy_r are transformed to absolute coordinates using equations (2.6) and (2.7)) with appropriate weighting for each cell population.

Notice that while the master array always corresponds to the same values of N_0 and N_1, the Ux_r and Uy_r arrays will be unique to each tape since the calibration constants change from tape to tape. In summary, the two main elements of the data analysis are (1) sorting of data into local arrays in the coordinates N_0, N_1 and (2) the inversion of one N_0, N_1 global array for each tape into table lookup arrays for Ux_r and Uy_r. Moreover, since the tables and associated arrays for each tape are written down together as final experimental data, they remain available for further processing (for example, the calculation of higher order moments of the populations) at a later time.

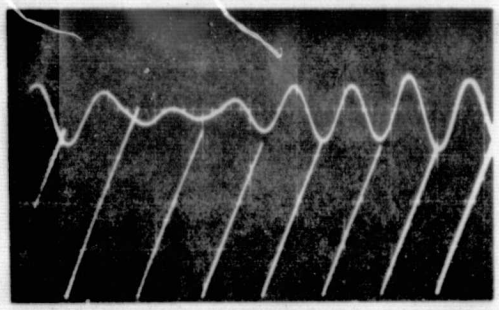

Upper-filtered Pitran signal
0.02 volts/div; 20 msec/div

Lower-Pitran ramp signal
2.0 volts/div; 20 msec/div

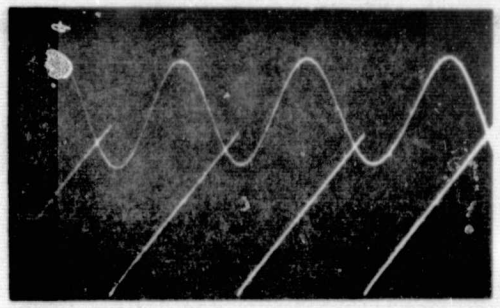

Upper-filtered Pitran signal
0.02 volts/div; 10 msec/div

Lower-Pitran ramp signal
2.0 volts/div; 10 msec/div

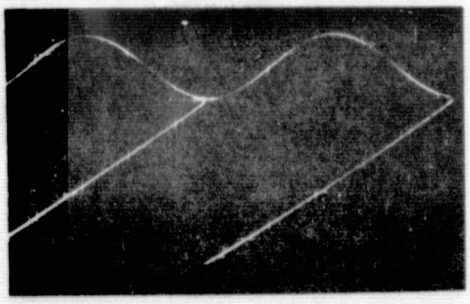

Upper-frequency standard
0.05 volts/div; 5 msec/div

Lower-Pitran ramp signal
2.0 volts/div; 5 msec/div

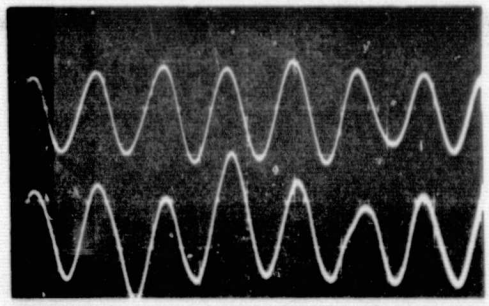

Upper-filtered Pitran signal
0.02 volts/div; 20 msec/div

Lower-unfiltered Pitran signal
0.02 volts/div; 20 msec/div

Figure 4.1 Some photographs of the Pitran pressure signal and its associated ramp.

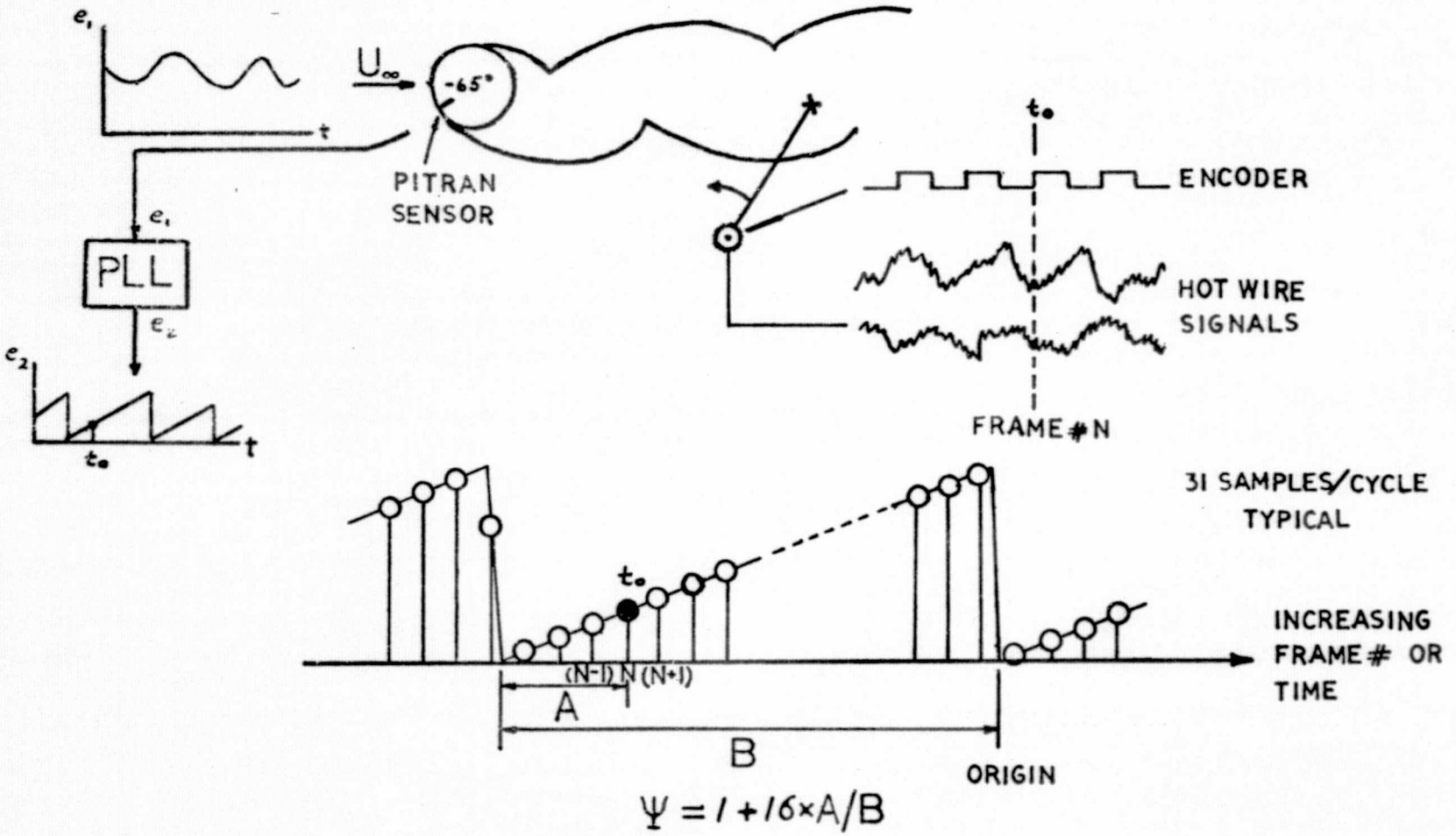

Figure 4.2 A sketch showing how ramp data were used to assign phase information to the hot wire data.

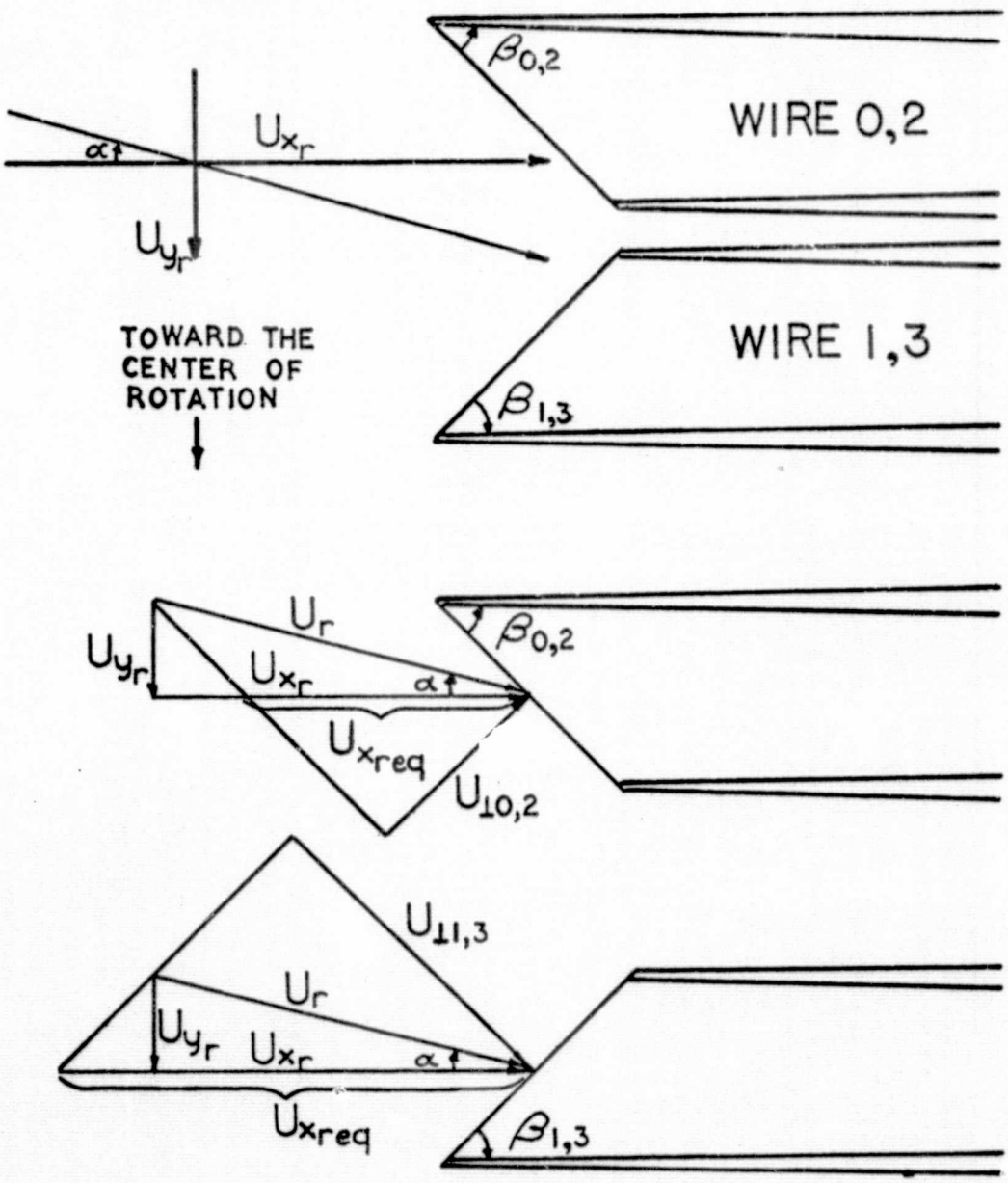

Figure 4.3 A sketch showing the choice of coordinates for two inclined wires, including the construction used to supplement data taken at $\alpha = 0$ with data taken at points along the arc where $\alpha \neq 0$.

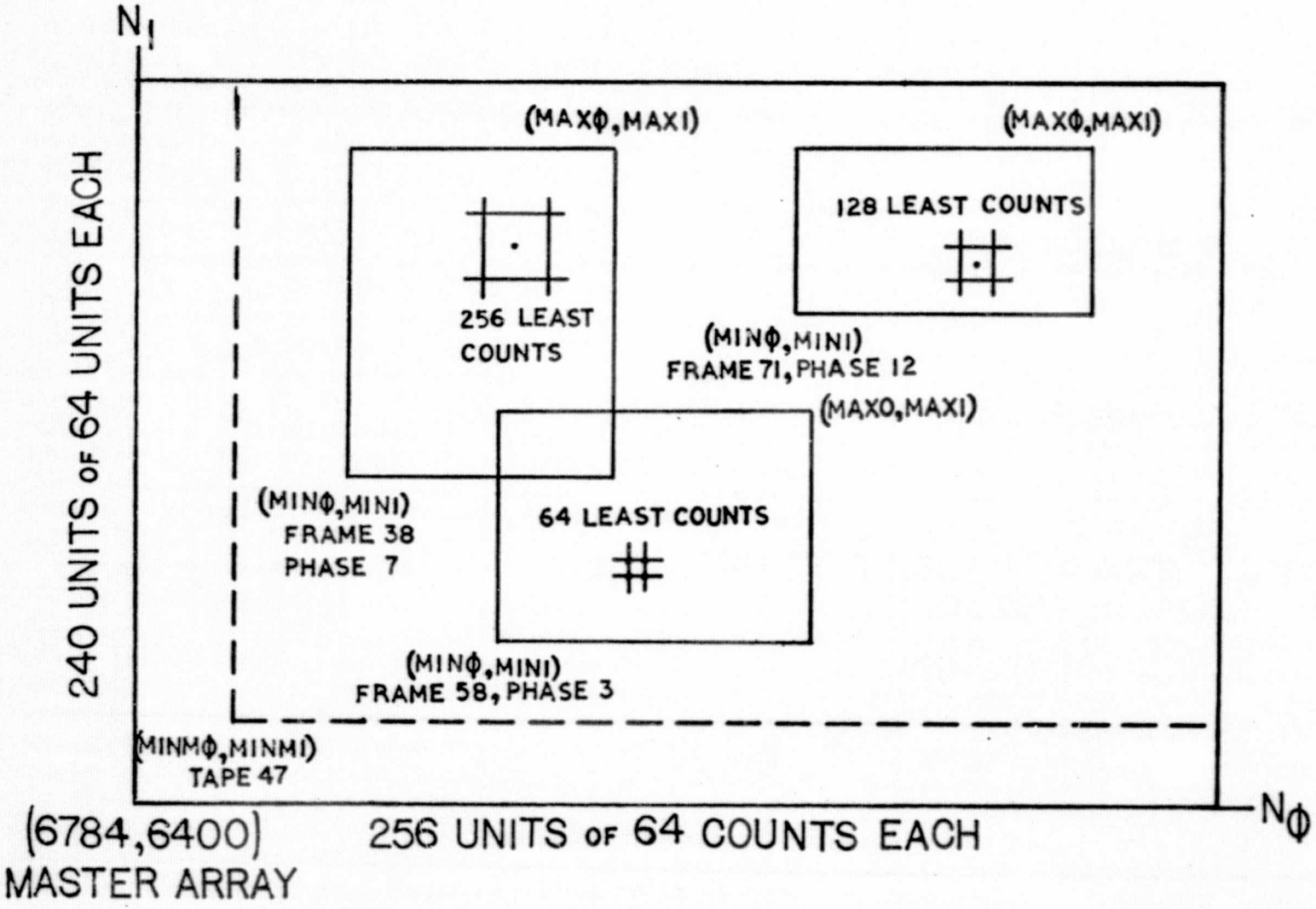

Figure 4.4 A sketch illustrating the master array and some typical sorted data arrays.

V. DISCUSSION OF RESULTS

5.1 Method of Presentation

Figures 5.1 through 5.32 show some of the results from the cylinder experiment.

With the exception of the plot of the mean flow field (Figure 5.2) and the intermittency plots (Figures 5.13a through 5.20a), all results presented in this thesis are taken from the x-wire pair on arm II, tapes 44-57. All results are therefore based on a population of 1024 sampled velocity vectors at each frame and phase*.

The field of measurement presented shows the near wake up to 6-1/2 diameters downstream of the cylinder.

Extensive use is made of the symmetry properties of this flow. The spatial symmetry of the mean flow about the wake centerline and the antisymmetric character of the vortex shedding process permit the data to be reflected to produce a coherent picture of the whole wake with data which were mostly taken below the wake centerline. For example, Figures 5.4 through 5.11 show one-half of the shedding cycle; if the second half of the cycle were to be included, Figure 5.11 would be followed by a figure produced from the same data as Figure 5.4 but with Phase 9 on top of Phase 1 and with the sign of each U_2 component reversed. It was only possible to make fairly cursory checks of the wake symmetry

*Data from the other x-array and other tapes will be included in the form of magnetic tape(s) or punched cards in a package which will eventually be sent to NASA Ames for use as a test case for advanced calculation codes on separated flow.

at the time of the experiment. However, the results indicate that the wake centerline deviated very little from the geometrical centerline of the cylinder.

The enormous yield of information from this experiment presented a very difficult problem of deciding what results to present and how to present them. It was felt that the presentation should stick as closely as possible to the actual measurements along the data arcs. As a result of this, some of the plots may not be as pleasing to the eye as they might have been if the measurements had been first interpolated onto a square grid. This is particularly true in regions near the wake centerline where the reflected data overlap. Figure 5.2, which shows the mean velocity vectors measured along the data arcs, looks particularly busy. In fact, if one looks obliquely along the long dimension of this figure, it becomes apparent that it is actually composed of vectors measured along three distinguishable sets of arcs corresponding to tapes 31-35, 36-43, and 44-57 (see Figure 3.3), which have been reflected about the wake centerline. While it has its disadvantages, this approach to the presentation of the results presents a truer picture of the agreement or disagreement between measurements at redundant or overlapping points in the flow.

An interpolation procedure was used between points in the overlapping areas of actual and reflected data to produce the three-dimensional plots of Figures 5.21 through 5.26. Since all the data points along the arcs of tapes 44 through 57 have the same x coordinate, it was only necessary to interpolate along the

y direction.* The leftmost and rightmost points plotted at each frame lie in the plane z = 0 and may be used in conjunction with the scale provided on each plot to get quantitative information from the plots. It should be noted that the curves plotted in these figures begin with frame 48 (at X/D ~ 6.4) and end with frame 87 (X/D ~ -0.4). The lines connecting curves at adjacent frame numbers are at constant values of Y/D, 0.5 inches apart. The nodes of the mesh were inserted to enhance the three-dimensional effect of the figures and do not represent actual measurement points.

Figures 5.13b through 5.20b indicate points in the flow where the absolute value of the vorticity, ω, (normalized by U_∞/D) was greater than 0.2. The numbers on the plot were obtained by first multiplying the normalized vorticity by 10 and rounding to produce an integer which was then plotted. The solid lines on these plots were drawn in by hand to outline regions where the absolute value of $\omega D/U_\infty$ was greater than 1.7.

Figure 5.27b plots numbers derived by multiplying $\tilde{U}_1\tilde{U}_2/U_\infty^2$ by 100 and rounding to produce an integer. For example, the number 10 at X/D = 1.9, Y/D = -0.4 represents $\tilde{U}_1\tilde{U}_2/U_\infty^2 = 0.1$ at that point in the flow at phase 15 of the shedding cycle. The

*Data in the overlapping region exists at y coordinates corresponding to the actual data at a particular phase and at the negative (when reflected) of each of these y coordinates for the opposite phase. Each of these points was assigned two numbers; the first was the measurement at the point for the phase in question, the second was found by a linear interpolation between surrounding points at the opposite phase. The point actually plotted was simply the average of these two numbers.

solid lines in this plot delineate points where $\tilde{U}_1\tilde{U}_2/U_\infty^2$ was greater than 0.01. The dashed lines enclose regions where $\tilde{U}_1\tilde{U}_2/U_\infty^2$ was less than -0.01.

5.2 Mean Flow Field

Figure 5.1 is a plot of the surface pressure distribution around the cylinder. The open points represent a long time average of the pressure at each point. The solid points show the maximum and minimum that occurred when the pressure was averaged over a quarter of a second (about 9 shedding cycles). The vertical lines show the maximum and minimum instantaneous pressure ever measured out of a population of several thousand points.

The mean pressure distribution is typical of what has been measured before, and indicates subcritical behavior at a Reynolds number of 140,000. Separation of the surface boundary layer occurs approximately 85 degrees away from the forward stagnation point with a base pressure coefficient of -1.21 and a drag coefficient of 1.23. Adequate two-dimensionality of the mean properties of the flow at this Reynolds number was indicated by the base pressure coefficient which varied less than 2 percent along the span of the cylinder (aspect ratio $\sim$ 29:1). The unsteady limits of the base pressure give better insight into the uproar that occurs in the near wake and show that the instantaneous base pressure coefficient can go as low as -3.5. It is interesting to note the lack of variation in C_p at the forward stagnation point. The symmetry of the flow upstream of the cylinder seems to be unaffected by the energetic unsteady motions in the near wake.

Figure 5.2 shows the mean velocity field. This figure is composed of reflected measurements along three distinct sets of arcs each denoted by a different symbol for the head of the velocity vector (see also Figure 3.3). Using the fact that vectors near the downstream end of the plot outside the wake are to a good approximation equal to the free stream velocity, one can get quantitative information about how the mean wake is behaving. Several curves connecting the heads of arrows have been drawn to indicate the velocity defect of the wake.

The most striking feature of Figure 5.2 is the small size of the mean separation bubble. In fact, the bubble is so small that very few experiment points fell inside the zone of recirculating flow. The mean closure point is not very well defined but appears to be about 1.1 diameters behind the cylinder center. There are really no other measurements of this flow available for comparison. Castro (Ref. 4) measured the separation bubble behind two-dimensional porous flat plates using a time of flight probe. For the case of zero porosity, he found the bubble length to be about 2.3 plate heights long. However, the two flows differ markedly. In particular the drag coefficient of the flat plate is nearly twice that of the cylinder, giving rise to a substantially wider wake. If the length to width ratio of the bubble (measured from the cylinder center) is used as a basis for comparison, agreement between the two flows is better (about 1.3 for the flat plate and 1.1 for the cylinder).

Roshko (Ref. 12) measured the static pressure distribution

in the wake of a cylinder at a Reynolds number of 14,500. The results of his experiment indicated bubble closure around 2 diameters downstream of the cylinder center. Again a comparison is difficult because of the wide discrepancy in Reynolds numbers between the two experiments and the difficulty in interpreting static pressure measurements in such a wildly fluctuating flow. The effect of change of Reynolds number on the behavior of the shear layers separating from a circular cylinder has been studied by Schiller and Linke (Ref. 14) in the range $5000 < Re < 15,000$, and their results, as well as those of Bloor (Ref. 3), can be interpreted as indicating a trend toward shorter bubble lengths with increasing Reynolds number (see also Goldstein (Ref. 7)).

Another interesting feature of Figure 5.2 is the very rapid decay of the wake defect velocity. Within 1.4 diameters of the cylinder center, the mean centerline velocity has recovered to 30 percent of the free stream velocity; by 6 diameters, the centerline velocity has recovered to 80 percent of the free stream velocity. Figure 5.3 is a plot of $\Delta U_{\text{℄}}/U_\infty$ versus X/D. The rapid decay of $\Delta U_{\text{℄}}/U_\infty$ is further evidence of very powerful motions occurring in the near wake, which rapidly mix fluid together from opposite sides of the cylinder in a cateract of turbulent vortex formation.

Figure 5.2 bears a striking resemblance to the streakline pictures of low Reynolds number flow past cylinders found in many textbooks. Prandtl and Tietjens (Ref. 9) show a photograph (p. 302, Figure 58, Dover 1957) of the flow at Re = 9 which

strongly resembles Figure 5.2.

One last feature of Figure 5.2 which bears mentioning is the slight overshoot in the velocity profile near the separation point. The velocity here agrees well with the measured 90 degree pressure coefficient. The overshoot decays rapidly and, by an X/D of 1.0, is gone completely.

5.3 Flow at Constant Phase

The basis for the technique of ensemble averaging at a constant phase is that this flow repeats itself periodically. Imagine sampling at some point in the flow when the shedding vortices are at some known position. Now wait one cycle until the vortices are again at the same position; take the next sample. Do this many times to build up a large population. The common property of the samples in this population is that they represent the random and regular behavior of the flow at the point in question with the vortices frozen in some average position. Fluctuations away from the mean in this population come from two sources: the random fluctuations due to the turbulence superimposed on the large scale vortices, and fluctuations due to the fact that not every vortex which is shed is exactly the same; there is dispersion. Evidence concerning the importance of the second source of fluctuations can be found in some of the results of the cylinder experiment and will be discussed shortly. With this in mind, the rest of the discussion of results will nonetheless refer to fluctuations away from the mean at constant phase as being due to background turbulence.

It was shown in the introduction that, for periodic flows,

the globally averaged Reynolds stress can be broken up into two parts, the contribution from the large scale periodic motion and that due to the background turbulence (equation 1.20). Equation (1.18) indicates that hybrid terms such as $\tilde{U}_j(\partial\bar{U}_i/\partial x_j)$ and $\bar{U}_j(\partial\tilde{U}_i/\partial x_j)$ participate in the transport of momentum at any given phase of the large scale motion. In the global average of this equation these terms average to zero. With equation (1.18) in mind, quantities such as $\tilde{U}_i\tilde{U}_j$ and $\langle U_i'U_j'\rangle$ will be hereafter referred to as the instantaneous Reynolds stress due to the large scale motion and the instantaneous Reynolds stress due to the background turbulence, where the word instantaneous takes on the special meaning of an ensemble average at constant phase.

Figures 5.4 to 5.11 show the flow field at eight phases during the first half of the shedding cycle. In b) of each of these figures the velocity vectors correspond to a frame of reference in which the cylinder is fixed. The data here are not complete enough to see precisely what is going on very close to the cylinder, but it would appear that two streamline patterns are possible. These are sketched in Figures 5.12c and 5.12d. Figure 5.12d shows a pair of waving Foeppl vortices with a moving closure point, and might correspond to the flow pattern shown in Figure 5.6b where evidence of closure may be seen at X/D = 1.0, Y/D = -0.5. Figure 5.12c shows one separation streamline reattaching on the base of the cylinder while the other heads off toward positive X. Again, the streakline pictures of the flow around cylinders are helpful. In his book, Batchelor (Ref. 1) includes a photograph (Figure 5.11.3)

made by L. Prandtl in 1927 which shows a streamline pattern similar to Figure 5.12c. Figures 5.4b, 5.8b, 5.9b, 5.10b, and 5.11b seem to fit case (c) in Figure 5.12, while Figures 5.5b, 5.6b and 5.7b fit case (d) in Figure 5.12. In Figure 5.5b a saddle indicating closure has begun to appear at X/D = 0.9, Y/D = -0.5. As evidence of the saddle continues to develop, the flow outside the saddle begins to acquire the appearance of a cusp until by Figure 5.8b the separation streamline from below the cylinder appears to have turned inward toward the cylinder base.

In the rest frame of the cylinder the flow takes on the character of a wave with a wave length equal to approximately 4.3 diameters and wave speed equal to about 1600 cm/sec (based on a shedding frequency of 37 Hz). In (a) of Figures 5.4 through 5.11 the same wave speed has been subtracted from the horizontal component of each velocity vector to give the flow field as it would be viewed in a frame of reference moving (approximately) with the vortices. There is obviously some distortion of the vortices in this operation since they do not all move with the same velocity. However, the vortex centers shown approximate the actual centers (based on the peak in the instantaneous vorticity) fairly well. The streamlines in the view moving with the vortices form a pattern of centers and saddles which are reminiscent of some of the photographs of streaklines in Karman vortex streets found in textbooks, although the ratio between the lateral and longitudinal vortex spacing is only about 0.1 (compared to the von Karman value of 0.281). Figure 5.12a is a sketch of the instantaneous streamlines .

corresponding to Figure 5.4a. Notice that, in this frame of reference, the forward stagnation point must move upstream of the cylinder.

To understand where fluid particles are going in Figures 5.4a through 5.11a, it is helpful to estimate how far the fluid moves between phases. The free stream velocity was 2120 cm/sec. The time between phases was 1/16 of 1/37 of a second or about 1.7 msec. A fluid particle moving at the free stream velocity would therefore move about 3.6 cm or about 1/3 of a cylinder diameter between phases. This works into the plots in a convenient way since the lengths of the arrows drawn on the plots are about 2/3 of the distance that a particle, traveling with the velocity represented by the arrow, would move between phases. So the plots can be looked upon either as representing the velocity field or as representing streaklines on a photograph with an exposure time equal to about 2/3 of the time between phases.

Zdravkovich (Ref. 15) studied the Karman vortex street behind a circular cylinder by photographing streaklines produced by smoke particles introduced on one side of the cylinder. He observed an "unexpected" transfer of mass across the street with smoke finding its way into vortices on the opposite side of the wake. Figures 5.4 through 5.11 clearly illustrate this same effect. The entrainment mechanism comes through dramatically if copies of Figures 5.4a and 5.13a are held up to a bright light. With the intermittency in the background, entrainment is seen to consist of deep incursions of essentially irrotational (neglecting the presence

of low level free stream turbulence) fluid into the region between the vortices. A saddle associated with the shedding vortex may be seen in Figure 5.4a at X/D = 1.9, Y/D = 1.0. This saddle represents a confluence of fluid particles coming from above the wake with fluid which has been entrained from below by the vortex forming from the lower side of the cylinder. The outstanding feature here is that the forming vortex is entraining outside fluid from over half a diameter above the cylinder while fluid from the opposite side of the wake crosses the wake axis between the vortices with a vertical velocity component on the order of half the free stream speed. Some of the fluid crossing the wake axis will end up in the forming vortex and some in the next vortex downstream. Figure 5.12b illustrates the entrainment process in terms of the rollup of material lines in the near wake.

One of the interesting phenomena which is associated with the flow over a cylinder has to do with the interaction of the separating shear layers and the concomitant cancellation of vorticity in the rolling up of the shedding vortices in an area close to the cylinder, referred to as the vortex formation region. We have already seen some evidence of this interaction in Figures 5.2 and 5.3, where the rapid decay of the wake defect velocity is shown. It is clear from the dependence of $\Delta U_{\mathfrak{L}}/U_{\infty}$ on X/D shown in Figure 5.3 that the near wake can be divided into two distinct zones which join at the end of the formation region located at X/D ~ 2.4. Bloor and Gerrard (Refs. 3 and 5) define the end of the vortex formation region to be the point where fluid from outside

the wake first crosses the wake axis. Using this definition, the end of the vortex formation region occurs at $X/D \sim 2.2$ (Figure 5.20a) which agrees well with the definition implied in Figure 5.3. It is interesting to note that the formation region extends well downstream of the mean separation bubble.

The fraction of circulation injected into the wake at one of the separation points during one shedding cycle which is carried downstream is given by (Roshko (Ref. 11))

$$\Gamma = \frac{U_\infty^2 - U_{\mathcal{L}}^2}{m^2 U_\infty^2} = \frac{1}{m^2}\left(1 - \left(\frac{U_{\mathcal{L}}}{U_\infty}\right)^2\right) \quad ; \; m = \frac{U_s}{U_\infty} \qquad (5.1)$$

where U_s is the velocity outside the boundary layer at the separation point. For the cylinder experiment m had a value of 1.45. At the end of the vortex formation region ($X/D = 2.3$) Γ has a value of 0.29; over seventy percent of the circulation injected in one side of the cylinder has been lost through cancellation and diffusion in the formation region.

It should be pointed out that cancellation implies the coming into proximity of fluid particles of opposite signed vorticity which eventually lose their vorticity through diffusion across the gradient which then exists. The results of the cylinder experiment can shed some light on the areas of the flow where fluid elements with opposite signed vorticity interact. Figures 5.13b through 5.20b are helpful in this regard. Here the vorticity was found by taking the flow field in Figures 5.4 through 5.11 and calculating the circulation about the parallelogram formed by four neighboring points on two adjacent data arcs. The circulation was divided by the area

of the parallelogram and the resulting number multiplied by $10(D/U_\infty)$. The integer which resulted after rounding was plotted at coordinates corresponding to the center of the appropriate parallelogram. The solid lines on these figures outline regions where $(\omega D/U_\infty)*10$ was greater than 17 (although due to experimental scatter it is possible to find isolated points less than 17 within the solid lines).

The process of vortex rollup refers to the rolling up of material lines in a fluid, as illustrated in Figure 5.12b, and may have no obvious connection with the instantaneous streamlines in a given frame of reference. Hence, while the flow may appear to be a wave in the frame of reference of the cylinder, there is a process of fluid rollup into discrete vortices occurring. Moving with a coordinate system which makes the flow quasi-steady helps some, and the views of the velocity field moving with the vortices show the vortex formation process fairly clearly. The best variable for viewing this process is the vorticity, since it does not suffer from lack of Galilean invariance; and, by following a given concentration of vorticity, one is, to a gross approximation, following the same concentration of fluid particles.

Figure 5.13b shows a vortex forming from the lower side of the cylinder. A region of positive vorticity is rolling up about two diameters downstream of the cylinder center. A neck of high vorticity fluid leads back toward the cylinder along the same general line as the separation streamline in cylinder fixed coordinates. Above this, coming from the opposite side of the cylinder is a smaller region of opposite signed vorticity. Some of the fluid

which enters this region will be rolled up into the forming vortex, and some will eventually form the nucleus of the next vortex. Fluid at the end of this region near X/D = 1.1, Y/D = 0.2 is carrying negative vorticity downward and back toward the cylinder at about a 60-70 degree angle as may be seen in Figure 5.4a (vortex fixed coordinates). As the vortex develops, the region of negative vorticity grows outward and downward; velocity vectors (vortex fixed coordinates) along the lower right hand portion of this region continue to point down and toward the cylinder, and by Figure 5.10a a saddle for the newly forming vortex has appeared at X/D = 1.5, Y/D = -0.9. Figure 5.19b shows the vortex center slightly less than three and a half diameters downstream trailing a tail of tenuously positive vorticity composed of fluid which is unquestionably turbulent (as evidenced by Figure 5.19a), but which has lost much of its large scale vorticity through cancellation and diffusion in the interaction with fluid plunging down from above. A comparison of Figures 5.13-5.21a and b shows bridges of fluid between the vortices composed of turbulent fluid which has lost the bulk of its large scale vorticity through cancellation and diffusion in the formation region, and the rest through more mild diffusive effects between neighboring vortices downstream of formation. Hereafter these areas will be termed "connective tissue" (the term is due to L. S. G. Kovasznay). These regions of connective tissue correspond to the saddles, or areas of confluence, described earlier in connection with entrainment.

5.4 The Anatomy of Momentum Transport

In the presentation of the Reynolds stresses, the problem of which results to present and how to present them becomes most severe. The inclusion of all of the results would entail plots for the two contributions to each of three Reynolds stresses at 17 (including global mean) phases of the motion--102 plots in all! Therefore, it was decided to limit the discussion to the results for the mean flow and the flow at one representative phase of the motion. Since similarity concepts do not apply in the near wake, all results were normalized by the free stream velocity rather than some other characteristic velocity, and no attempt was made to reduce any of the data to universal form.

Three-dimensional surfaces, all plotted to the same scale, are used to present the results for the whole field of motion (Figures 5.21 through 5.26). These have the disadvantage that small details are difficult to distinguish; therefore, results are included which show the Reynolds stresses at one downstream station (frame 56) (Figures 5.28 through 5.31). Then the aperture is closed down one more stop to focus on the history of stress at one point in the flow (frame 56, tape 53, $X/D = 4.97$, $Y/D = -0.60$). This is shown in Figure 5.32.

The naming of velocity components follows the usual convention, where 1 denotes the downstream direction and 2 the lateral direction. The sign convention which is adopted for the stress considers positive τ_{ij} as the transport of positive i momentum in the positive j direction. The reason for this choice (the usual convention puts a minus sign in front of $\overline{U_i''U_j''}$) was to facilitate the discussion which uses the terms "stress" and "momentum transport (or flux)" interchangeably.

The normalizing factor U_∞^2 will be suppressed in the following discussion.

It was shown in the introduction that the conventional Reynolds stress can be broken up into two terms

$$\overline{U_i'' U_j''} = \overline{\tilde{U}_i \tilde{U}_j} + \overline{\langle U_i' U_j' \rangle} \qquad (5.2)$$

where the overbar represents a long time average or, equivalently, an average over all phases, and '' represents a fluctuation away from the global mean. The terms on the right of (5.2) written without the overbars would represent the contribution to the Reynolds stress at a particular phase from the large scale periodic motion and background turbulence, respectively.

Figures 5.24a, 5.25a, 5.26a and 5.27b, which show the stresses contributed by large scale motion at phase (7, 15), were produced by considering the velocity field shown in Figure 5.10b as a fluctuation away from the mean (Figure 5.2). For example, $\tilde{U}_1^2$ is the square of the difference between the horizontal component of a vector in Figure 5.10 and the corresponding horizontal component of a mean flow vector in Figure 5.2. The vortex centers at this phase (referring to Figure 5.19b) are located at X/D = 1.5, Y/D = 0.1; X/D = 3.3, Y/D = -0.2 and X/D = 5.5, Y/D = 0.25.

Figure 5.24a shows a series of double peaks in $\tilde{U}_1^2$, located on either side of the wake centerline, which occur at the same downstream stations as the vortex centers. The largest value of $\tilde{U}_1^2$ is about 0.16 and occurs at X/D = 1.5, Y/D = 0.5. By referring to Figure 5.10b, one can see how the peaks in $\tilde{U}_1^2$ arise; at X/D = 3.3, the velocity of fluid above the vortex is retarded from the mean velocity,

and that below the vortex is accelerated above the mean velocity by nearly the same amount. The astonishing feature of Figure 5.25a is that $\tilde{U}_1^2$ is very nearly zero all along the measured part of the wake centerline. This remarkable result holds true throughout the shedding cycle and thus also in the global average, $\overline{\tilde{U}_1^2}$ (Figure 5.21a). This is especially surprising in view of the very rapid relaxation of $U_{\mathcal{C}\!\!\!/}$ in the first few diameters of the wake (Figure 5.3).

Figure 5.24b shows the results for $\langle U_1'^2 \rangle$ (the background turbulence) at phase (7, 15). In this figure, the peaks occur at approximately the same positions as the vortex centers. A comparison of Figure 5.24b with Figure 5.19 shows a ridge connecting the peak in $\langle U_1'^2 \rangle$ at (3.3, -0.2) to the maximum near the lower side of the cylinder. A similar connection between the peak at (3.3, -0.2) and that at (5.5, 0.25) can be seen in Figure 5.24b in the form of higher values of $\langle U_1'^2 \rangle$ at the left end of curves corresponding to frames lying between the two peaks. Note that the leftmost and rightmost points of each curve show a vertical line connecting the point to the plane z = 0 for reference purposes. The connecting ridges correspond to areas described earlier as "connective tissue".

Figures 5.25a and b show the same two views in terms of U_2. Figure 5.25b shows that $\langle U_2'^2 \rangle$, and hence $\langle U_1'^2 \rangle + \langle U_2'^2 \rangle$ (the energy of background turbulence), behaves in much the same way as $\langle U_1'^2 \rangle$ only with a somewhat larger amplitude and with the same peaks and ridges even more apparent in this view than in the previous one. Figure 5.25a shows the effect of the deep incursions

of free stream fluid, with large vertical velocity component described previously, which result in high peaks in $\tilde{U}_2^2$ (0.38 at (1.7, 0)) lying between the vortices.

The two views of Figure 5.25 show evidence that the dispersion problem mentioned in section 5.3 arising from the aperiodicity in the vortex shedding has not seriously affected the Reynolds stress due to background turbulence. If such effects were important, one might expect to see small maxima in $\langle U'^2_2 \rangle$ located at the positions of the slopes of the large peaks in Figure 5.25a where $\tilde{U}_2^2$ changes rapidly and where $\langle U'^2_2 \rangle$ is at a fairly low level. None are observed, which would imply that the technique used for averaging the flow at constant phase was fairly effective in separating the two phenomena. Figure 5.26 shows the two contributions to the shearing stress. Figure 5.27b is helpful in interpreting 5.26; here, integers are plotted which correspond to multiplying $\tilde{U}_1\tilde{U}_2/U_\infty^2$ by 100 and rounding. The solid lines outline positive areas and the broken lines bound negative areas with integers -1, 0, 1 excluded. Concentrating on areas below the wake centerline, the shearing stress associated with the large scale motions is seen to consist of large peaks located on the downstream portion of the vortices near the places where the entrainment of free stream fluid is occurring. These are followed by smaller peaks of opposite sign which tend to cancel some of the effect of the eddy on overall momentum transport toward the axis. $\tilde{U}_1\tilde{U}_2$ in Figure 5.27b exhibits consistent antisymmetry about the wake centerline; large regions of x-momentum flux toward the wake

centerline are followed by smaller regions of x-momentum flux away from the centerline. The turbulent part of the shearing stress at constant phase (Figure 5.26b) shows somewhat different behavior from any of the stresses discussed so far. Near the cylinder it shows the expected peaks of opposite sign, both representing transport of x-momentum toward the centerline. Beyond $X/D = 3$, the character of $\langle U_1' U_2' \rangle$ changes. The curves in Figure 5.26b in the range $2.8 < X/D < 4.3$ show very little variation for $Y/D < 0$ and then slowly begin to drop monotonically toward a negative value at the left end of the curve. Curves in the range $4.3 < X/D$ show the opposite behavior.

The discussion will now turn to the globally averaged components of the Reynolds stresses. Figure 5.22 shows the two components of $\overline{U_2''^2}$. Both have a maximum at $Y/D = 0$ with the curves of $\langle \overline{U_2'^2} \rangle$ being somewhat broader, with lower peaks and higher tails, than $\overline{\tilde{U}_2^2}$. Figure 5.21 shows the two components of $\overline{U_1''^2}$. Here the curves are substantially different, as was described earlier. Curves of $\langle \overline{U_1'^2} \rangle$ for frames near the cylinder have two peaks corresponding to the mean positions of the separation shear layers. Downstream the two peaks flatten out until $X/D \sim 3$, then a single peak begins to appear. Beyond $X/D \sim 3$, $\langle \overline{U_1'^2} \rangle$ resembles $\langle \overline{U_2'^2} \rangle$ except that $\langle \overline{U_2'^2} \rangle$ is of somewhat larger amplitude at points away from the wake centerline. The two contributions to the mean shearing stress are shown in Figure 5.23. Qualitative differences between $\overline{\tilde{U}_1 \tilde{U}_2}$ and $\langle \overline{U_1' U_2'} \rangle$ are difficult to detect in these plots, and a discussion of mean shear stress will concentrate on frame

56. Figure 5.28 shows the three globally averaged Reynolds stresses and their component parts at frame 56. In each case, the two components are of the same order with the large scale motions tending to dominate the shape of the overall profiles. More experiments need to be done to see what happens when the Reynolds number is varied. However, it is clear that the relative importance of one component to the other is spatially dependent. At the center of the wake, there is no contribution to $\overline{U''^2_1}$ from the large scale motions (neglecting dispersion) but there is a large contribution to $\overline{U''^2_2}$ from these motions. Near the outer edges of the wake the turbulent component tends to dominate, and in general, the turbulent profiles tend to be broader and flatter, dropping off less rapidly than the large scale profiles. Both components of the shearing stress show a characteristic bulge away from the wake centerline with the turbulent component reaching a maximum farther toward the outside of the wake.

Figures 5.29 through 5.31 show the stress distributions at frame 56 during eight phases of one cycle of the motion. The second half cycle can be constructed by simply exchanging phases and reversing the sign of the shearing stress. The center of a counterclockwise vortex is located below the wake centerline at frame 56 during phase (13, 5). The center of a clockwise vortex is located above the centerline at the same frame during phase (5, 13) (Figure 5.8a). Maxima in $\tilde{U}_1^2$ occur on either side of the vortex center, while maxima in $\langle U_1'^2 \rangle$ occur at the vortex center. $\tilde{U}_2^2$ goes through peaks between the vortices, while $\langle U_2'^2 \rangle$ peaks at the

vortex center. The cross wake distribution of $\tilde{U}_1\tilde{U}_2$ is such that positive x-momentum is strongly transported toward the center of the wake prior to and during the arrival of each vortex center and weakly transported away from the centerline as the vortex passes. The cross wake distribution of $\langle U_1' U_2' \rangle$ is such that throughout the passage of the counterclockwise vortex positive x-momentum is transported toward negative Y/D and during the passage of the clockwise vortex (see also Figure 5.8a) positive x-momentum is transported toward positive Y/D.

Figure 5.32 shows in more detail what happens at one point in the flow (X/D = 4.97, Y/D = -0.6). Phases 1, 2, and 3 where γ goes through a minimum correspond to the passage of fluid, which is usually laminar (neglecting the low level free stream turbulence), over the point in question. All three turbulent Reynolds stress components go through minima at phase 2 whereas the large scale Reynolds stresses do not. In Figure 5.32, $\tilde{U}_2^2$ reaches a maximum at phase 2 while $\tilde{U}_1\tilde{U}_2$ is close to a maximum at phase 3. If one includes phase 16 as a laminar phase, then $\tilde{U}_1\tilde{U}_2(16)$ would cancel $\tilde{U}_1\tilde{U}_2(2)$. However, the rather large value of $\langle U_1' U_2' \rangle$ at phase 16 precludes this, and it appears that there is a net contribution to the shearing stress from large scale motions associated with the entrainment of free stream fluid toward the wake axis. The vorticity behaves as expected except that the maximum and minimum are separated by nine phases instead of eight with the minimum lagging the clockwise vortex center by one phase.

In Figure 5.32, $\langle U_1'^2 \rangle$ and $\langle U_2'^2 \rangle$ show similar trajectories. The maximum in $\langle U_1'^2 \rangle$ is slightly less than twice that in $\langle U_1'^2 \rangle$ when the counterclockwise vortex passes. Notice that the peaks in $\langle U_2'^2 \rangle$ are slightly closer together than those in $\langle U_1'^2 \rangle$. This proximity may be an effect of dispersion, which would tend to shift the peaks in $\langle U_2'^2 \rangle$ toward the maximum gradient in $\tilde{U}_2^2$. In Figure 5.32, $\tilde{U}_1^2$ reaches a maximum upon the arrival of the vortex centers while $\tilde{U}_2^2$ achieves a maximum between the vortices.

It is interesting to note that while both components of the shearing stress result in a net positive contribution, the two oppose each other during the leading portion of the counterclockwise eddy and during the trailing portion of the clockwise eddy.

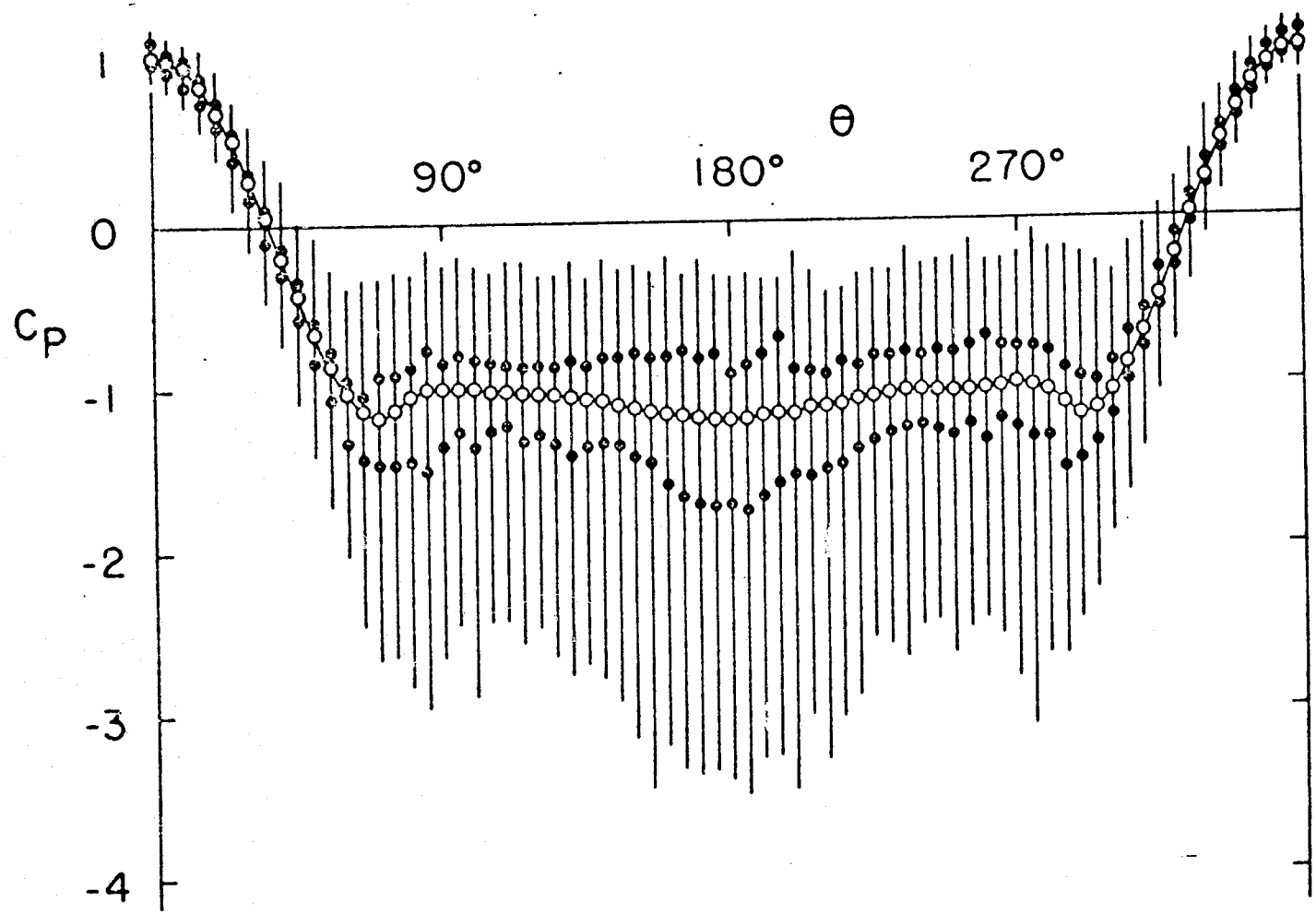

Figure 5.1 A plot of mean and fluctuating surface pressure at a Reynolds number of 140, 000

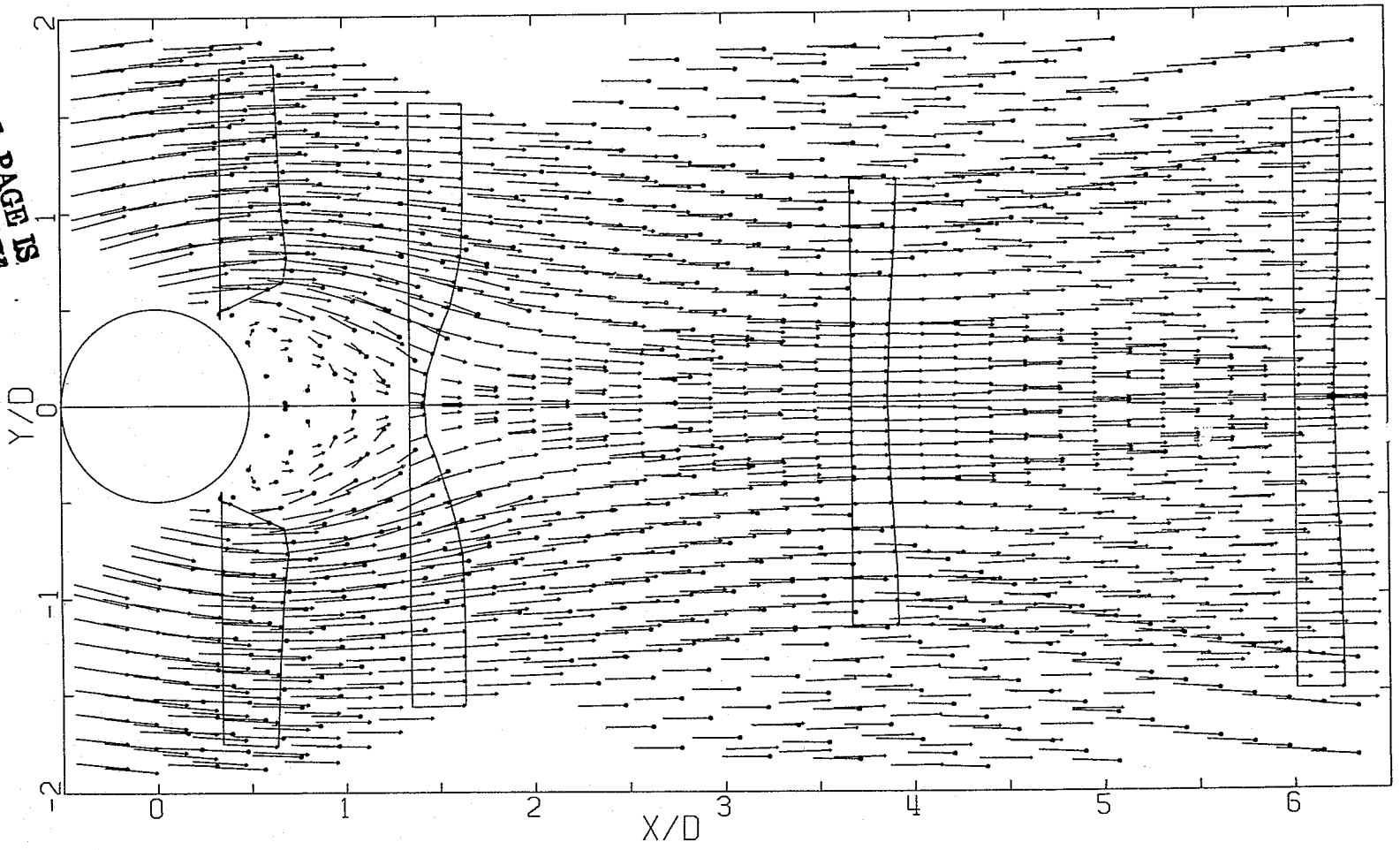

Figure 5.2 Mean flow vectors measured along three sets of data arcs corresponding to tapes 31-35, 36-43, 44-57.

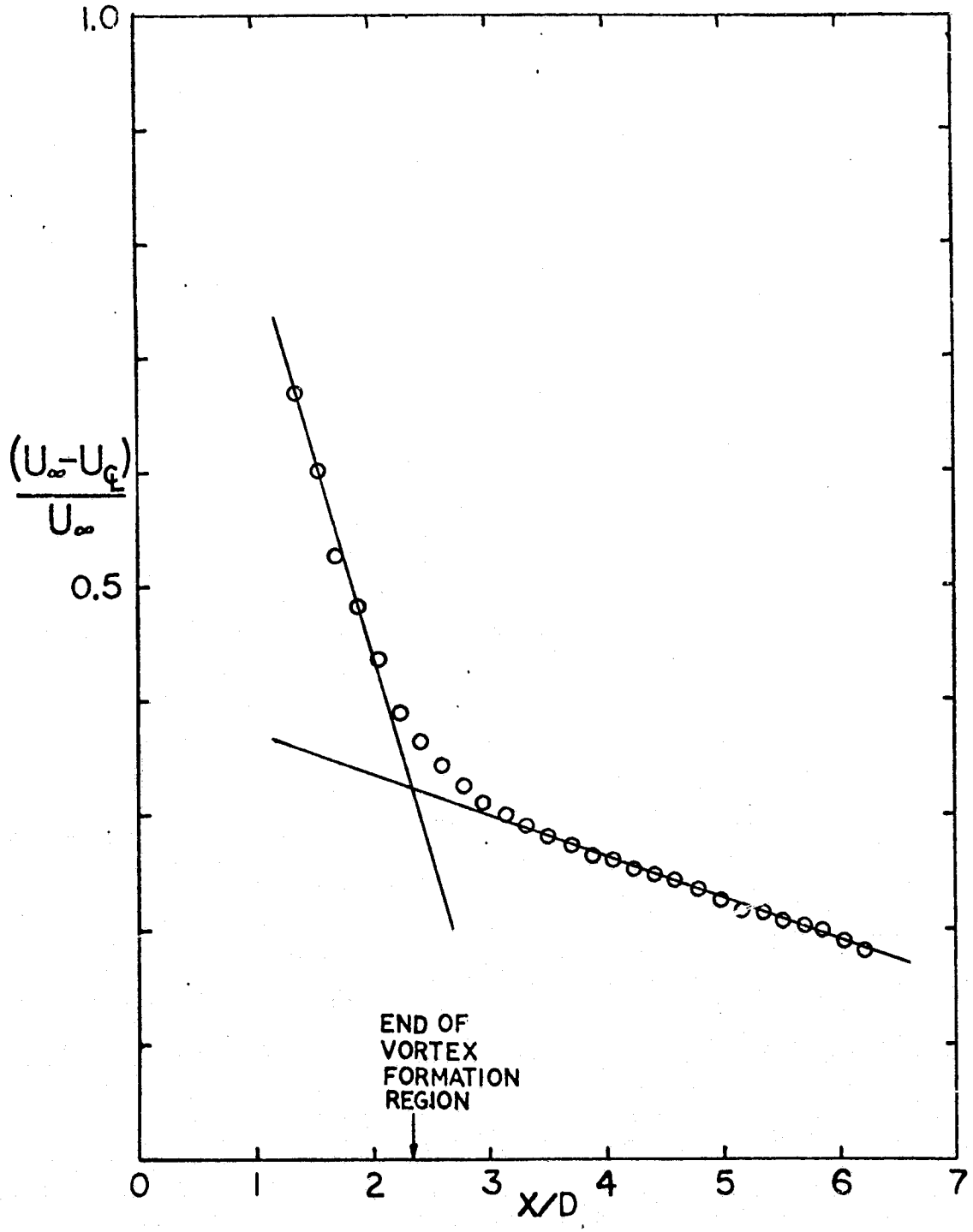

Figure 5.3 A plot of the variation in wake defect velocity, $\Delta U_\mathcal{C}/U_\infty$ with X/D.

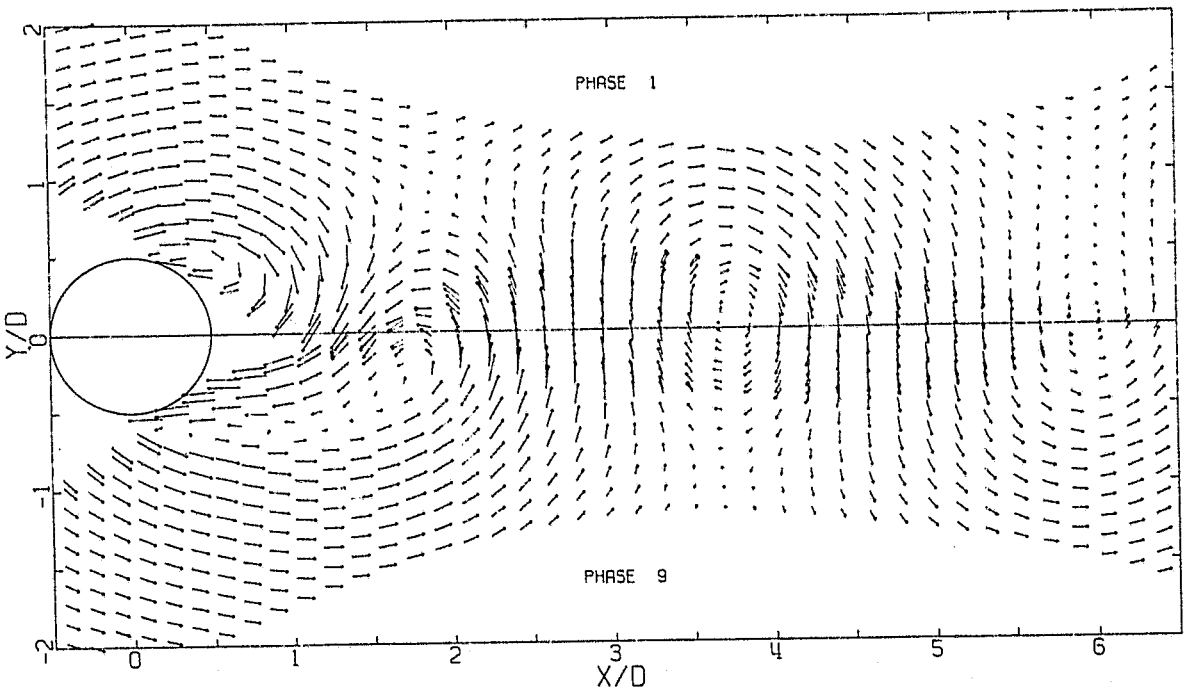

(a)

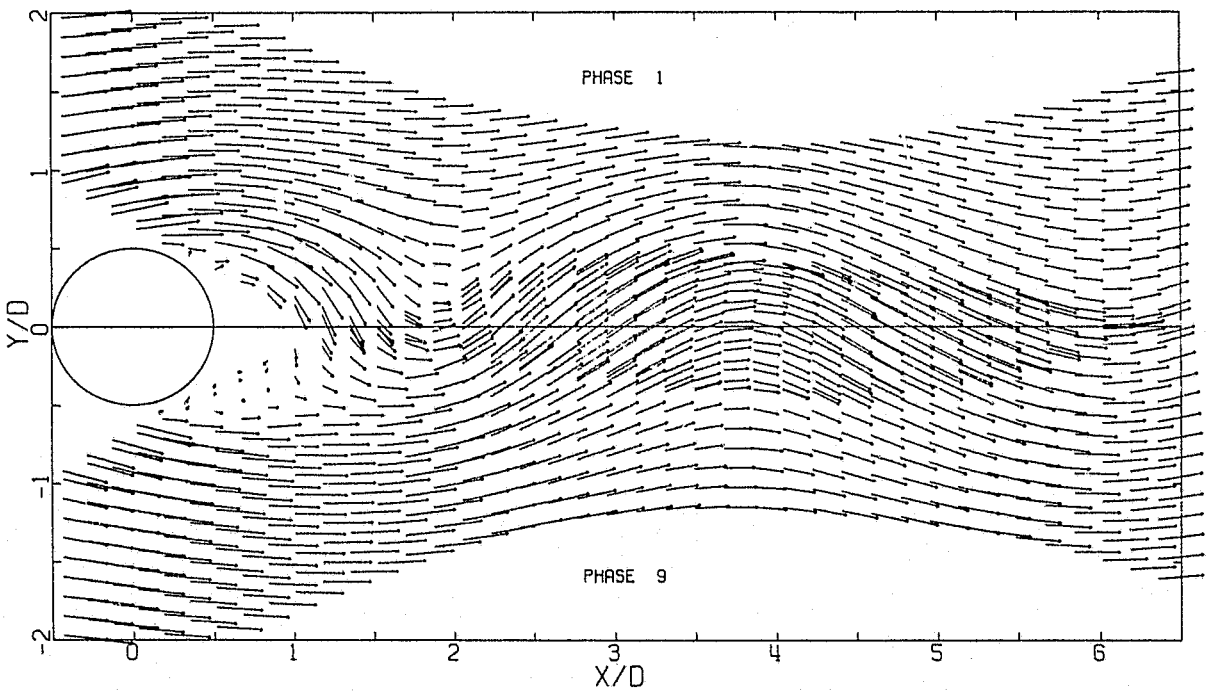

(b)

Figure 5.4 The velocity field at constant phase (1, 9) as viewed from a frame of reference: a) moving with the vortices, b) moving with the cylinder.

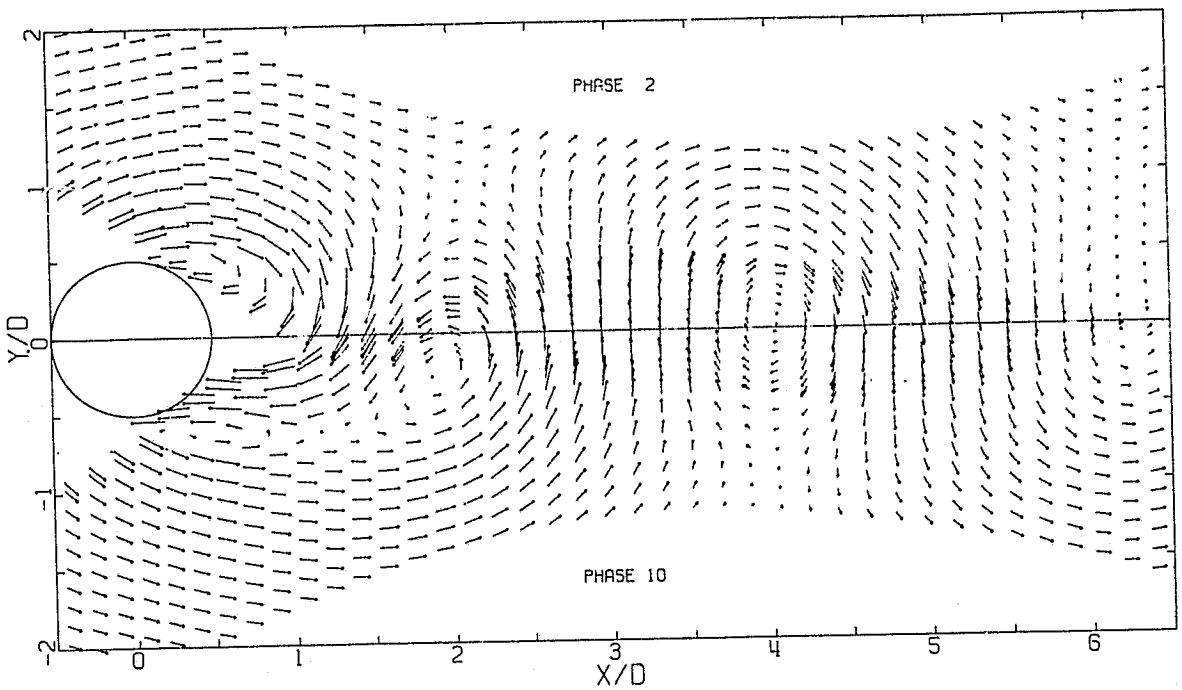

(a)

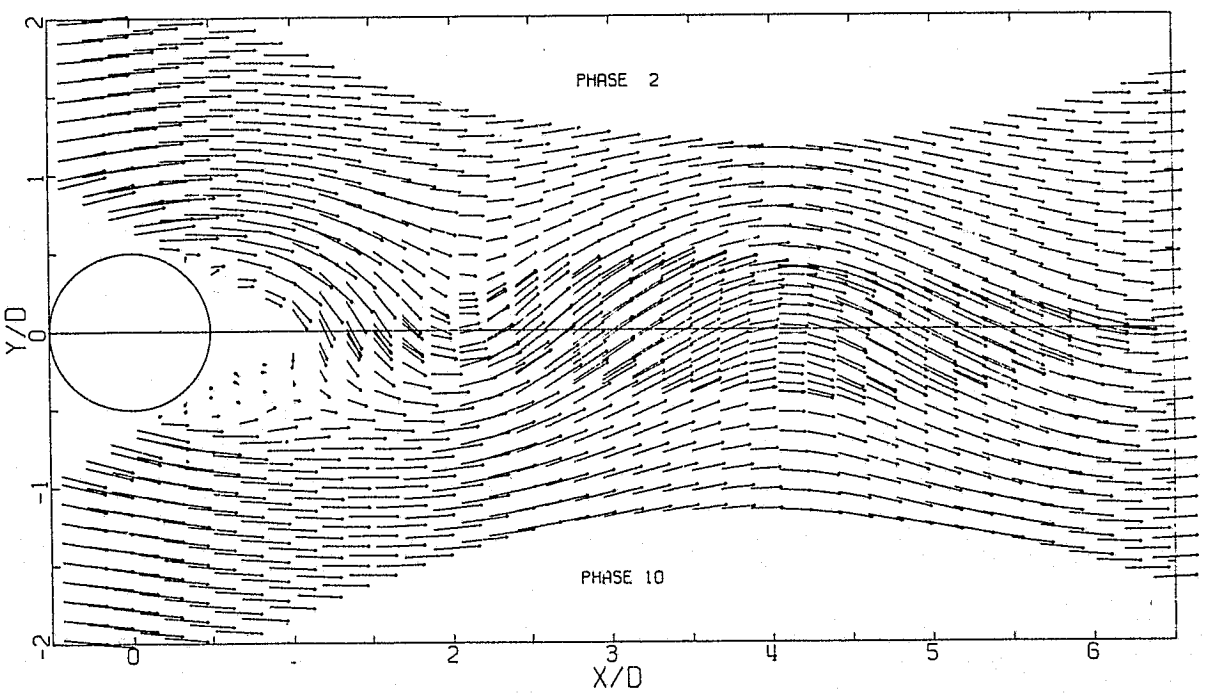

(b)

Figure 5.5 The velocity field at constant phase (2, 10) as viewed from a frame of reference: a) moving with the vortices, b) moving with the cylinder.

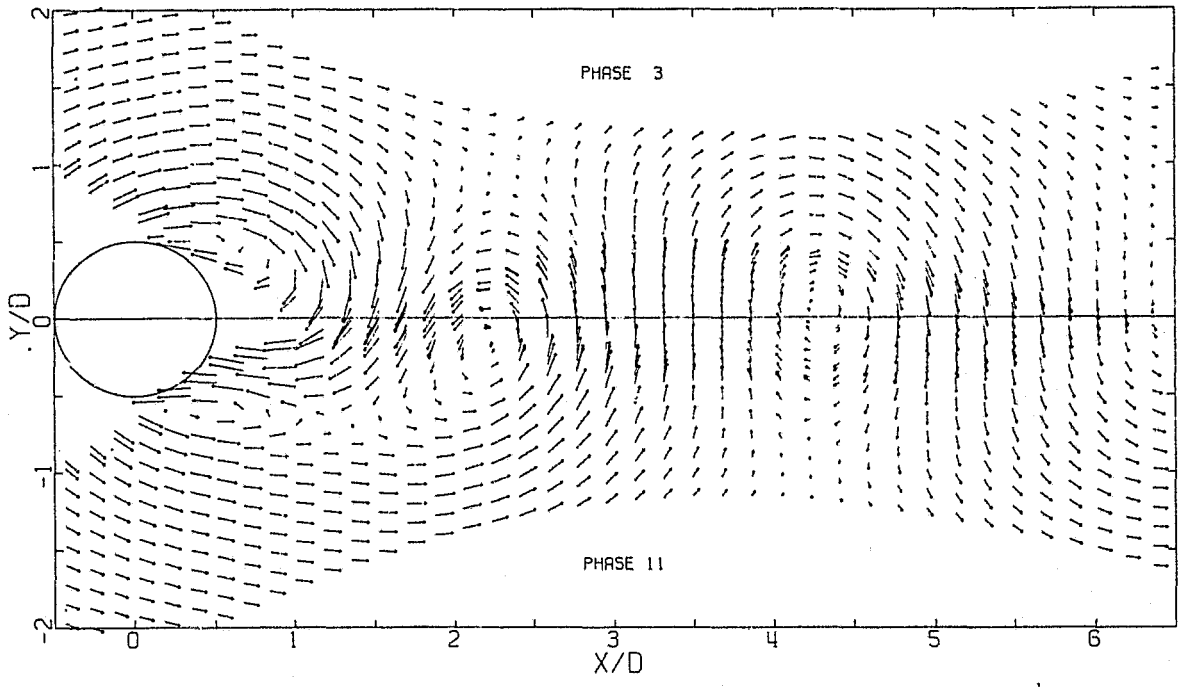

(a)

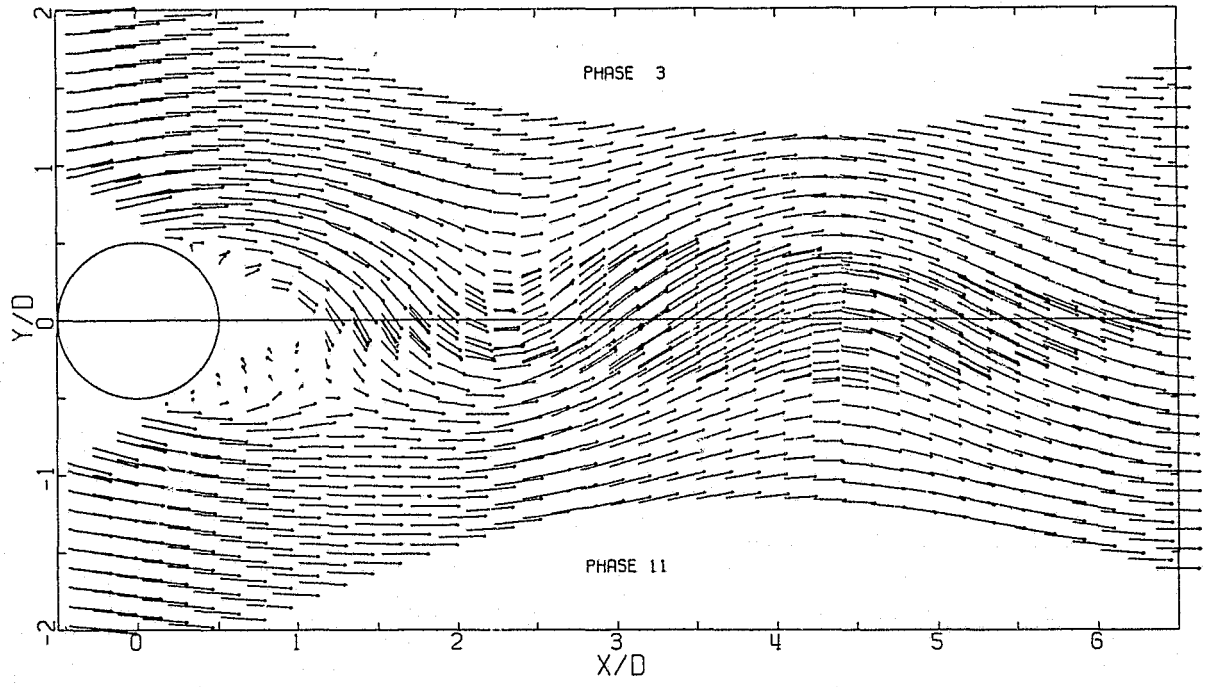

(b)

Figure 5.6 The velocity field at constant phase (3, 11) as viewed from a frame of reference: a) moving with the vortices, b) moving with the cylinder.

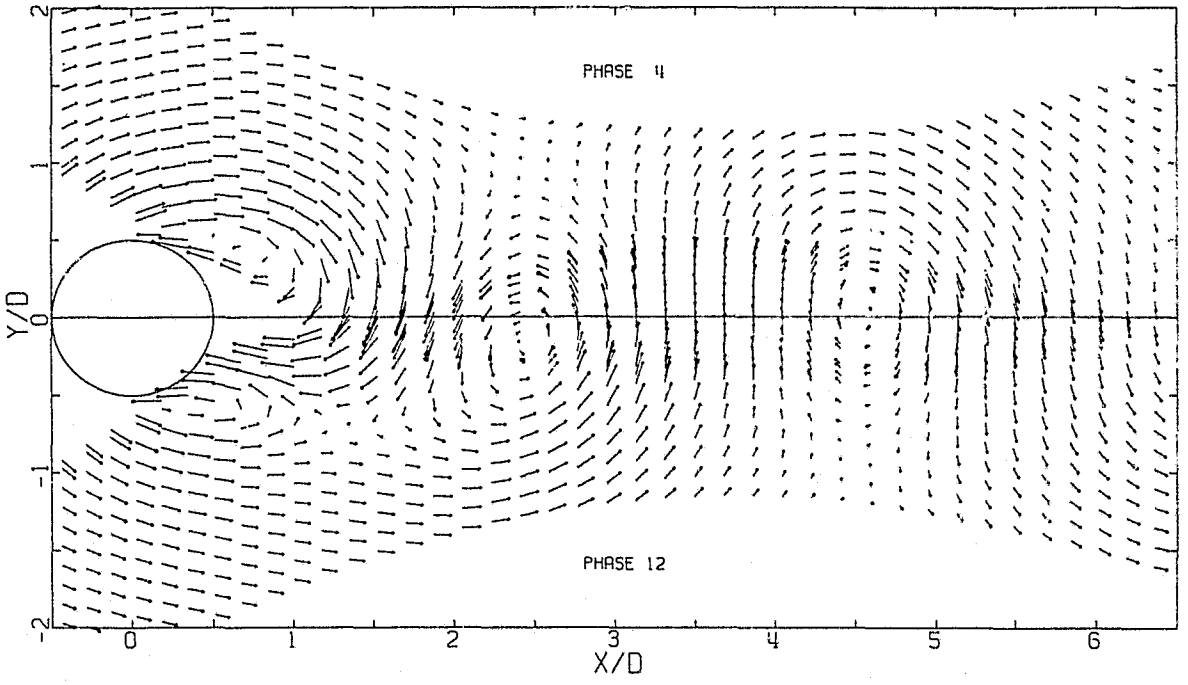

(a)

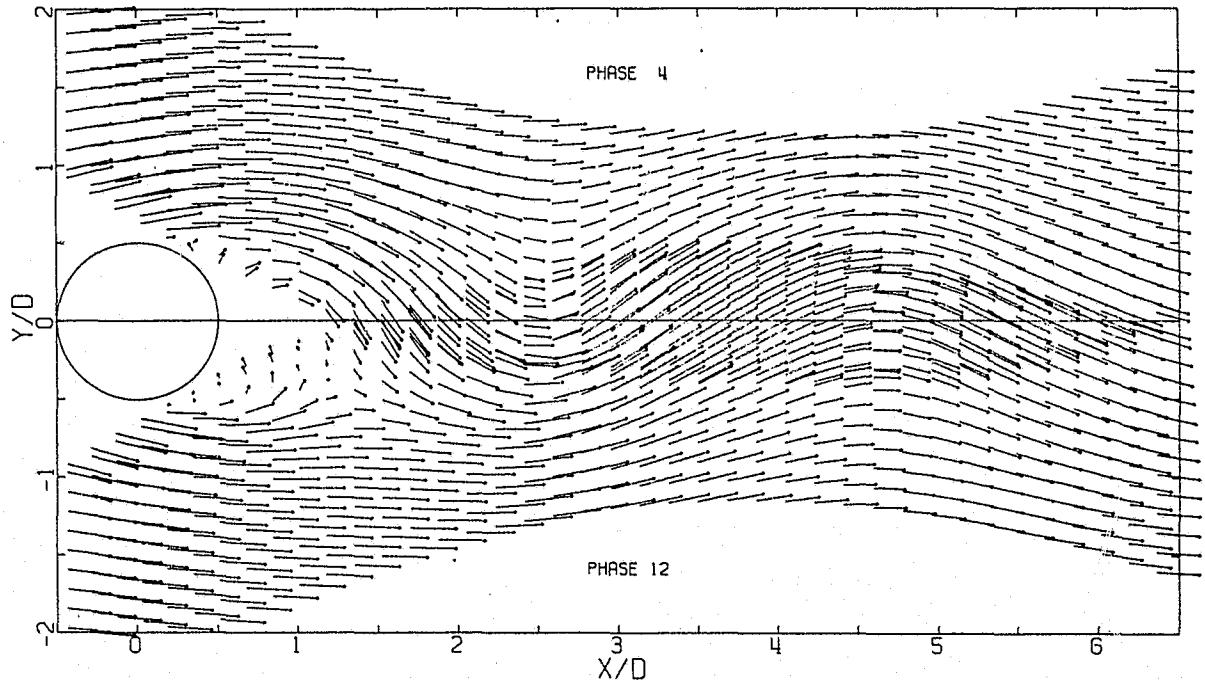

(b)

Figure 5.7 The velocity field at constant phase (4, 12) as viewed from a frame of reference: a) moving with the vortices, b) moving with the cylinder.

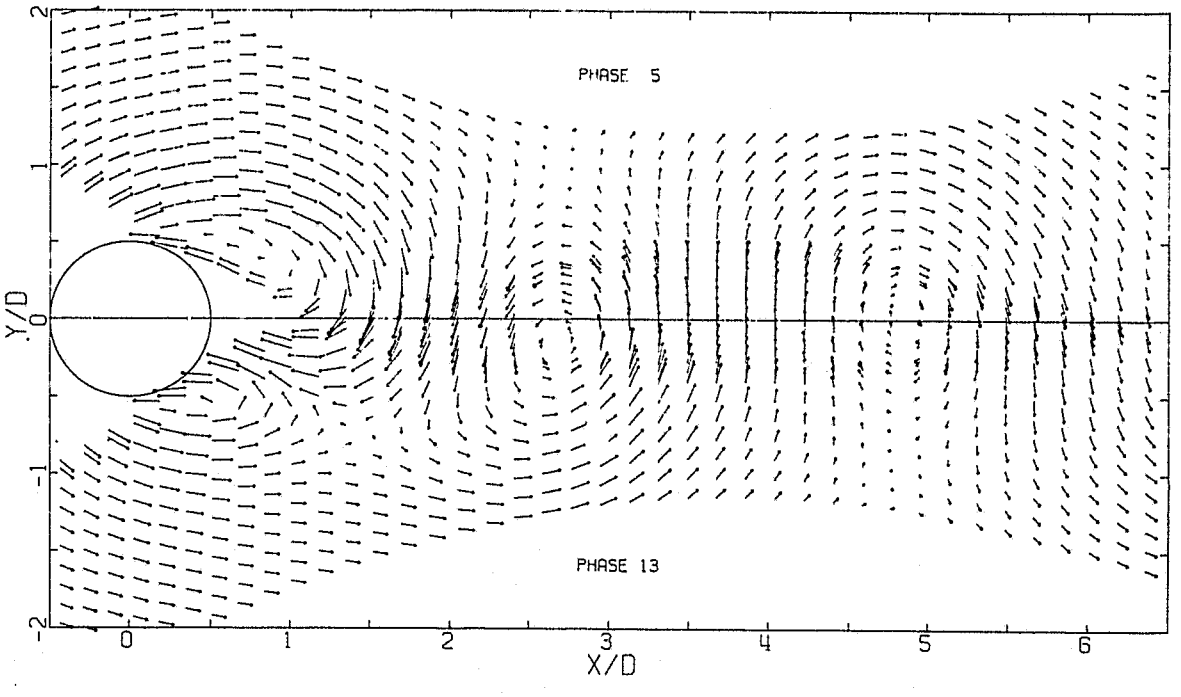

(a)

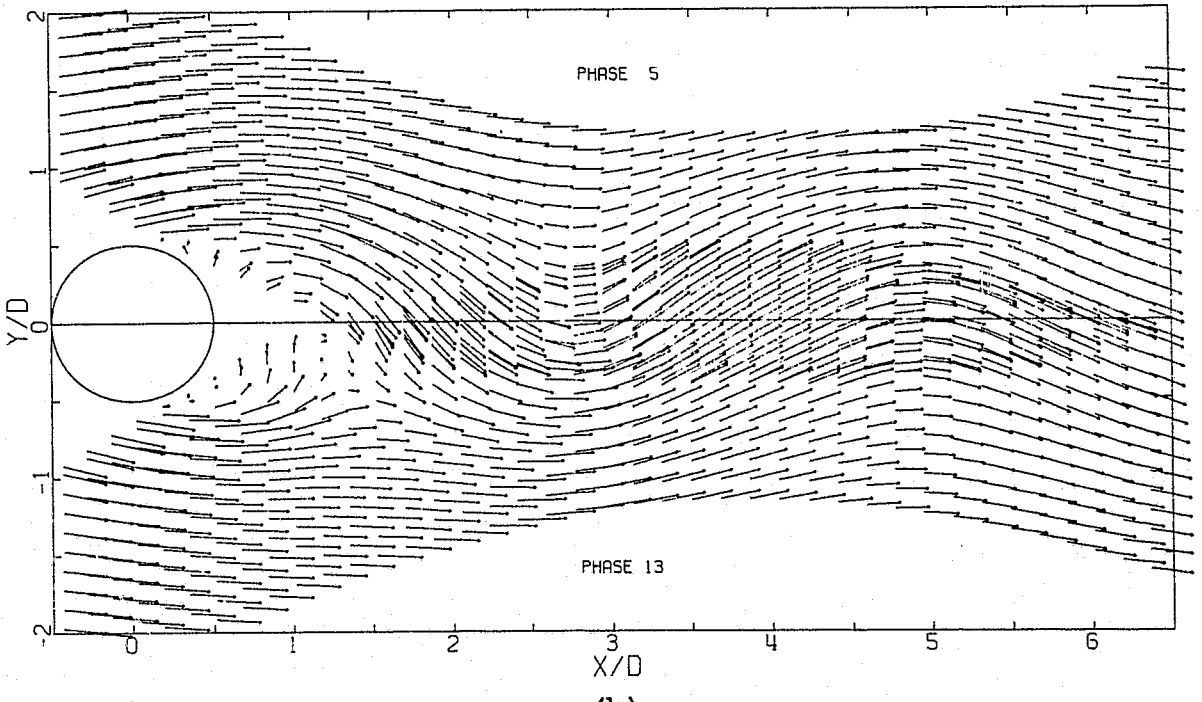

(b)

Figure 5.8 The velocity field at constant phase (5, 13) as viewed from a frame of reference: a) moving with the vortices, b) moving with the cylinder.

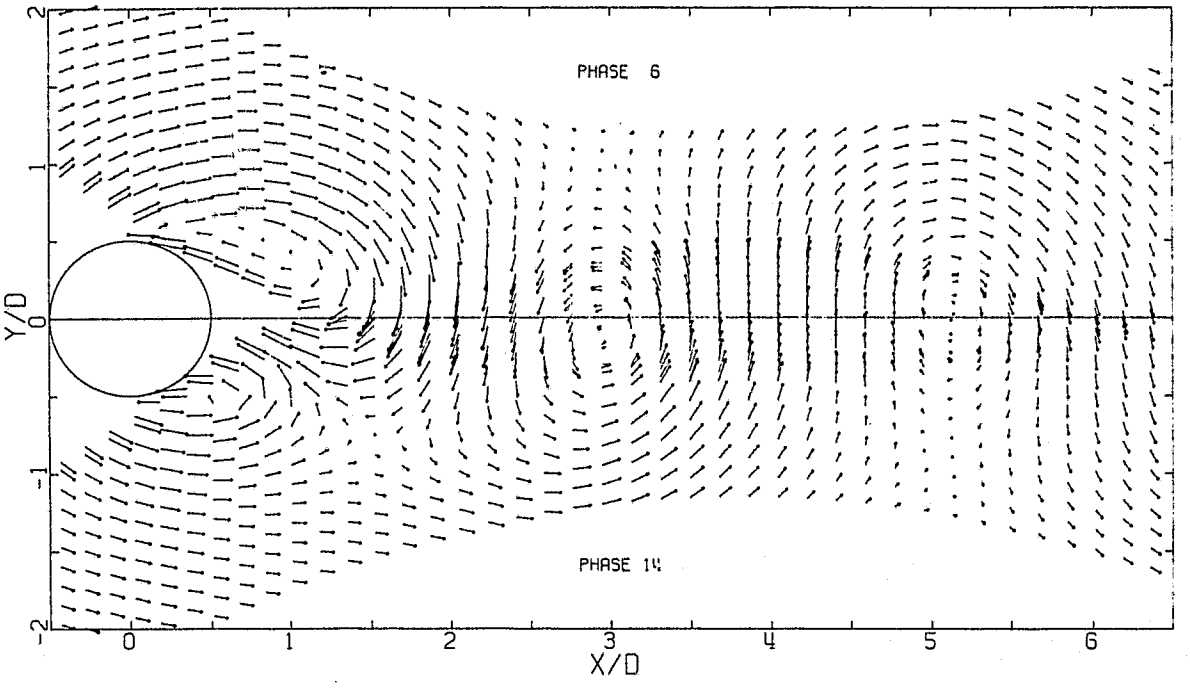

(a)

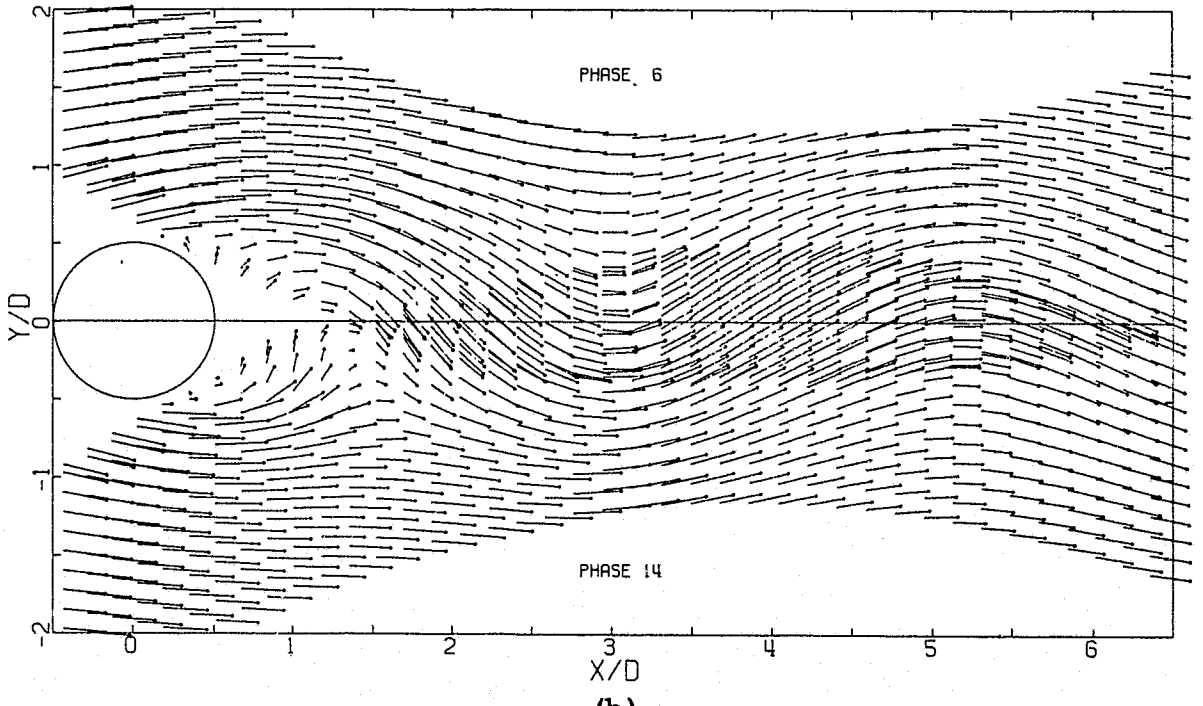

(b)

Figure 5.9 The velocity field at constant phase (6, 14) as viewed from a frame of reference: a) moving with the vortices, b) moving with the cylinder.

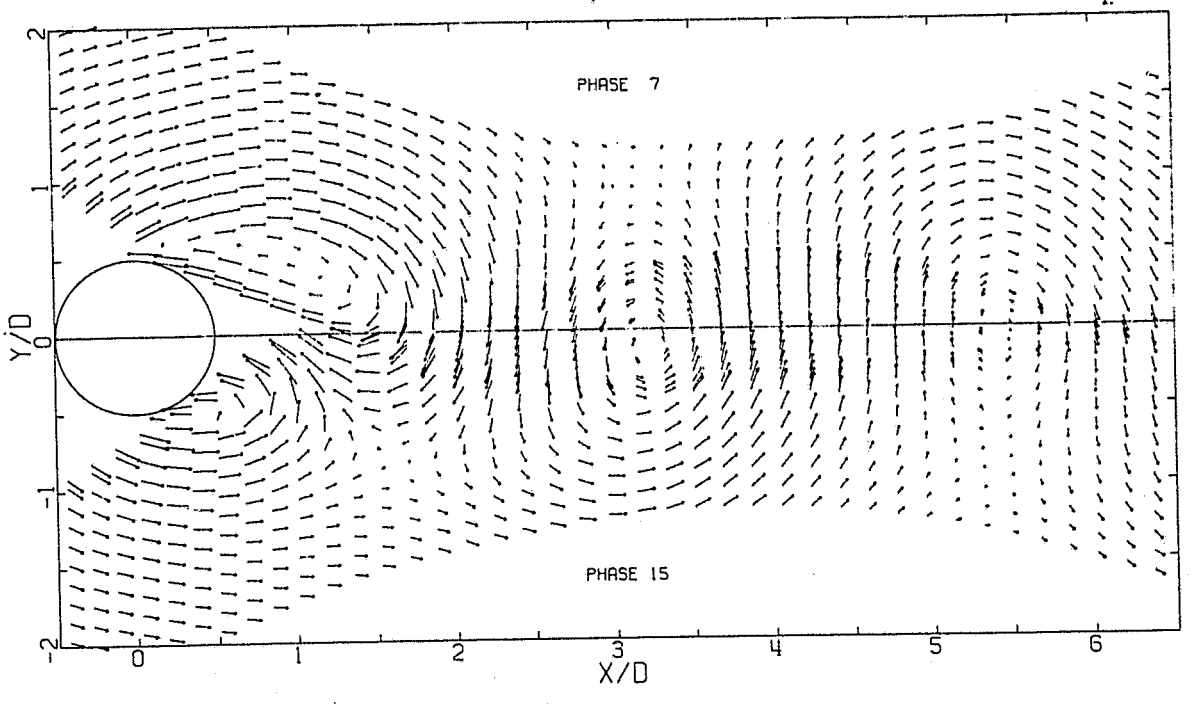

(a)

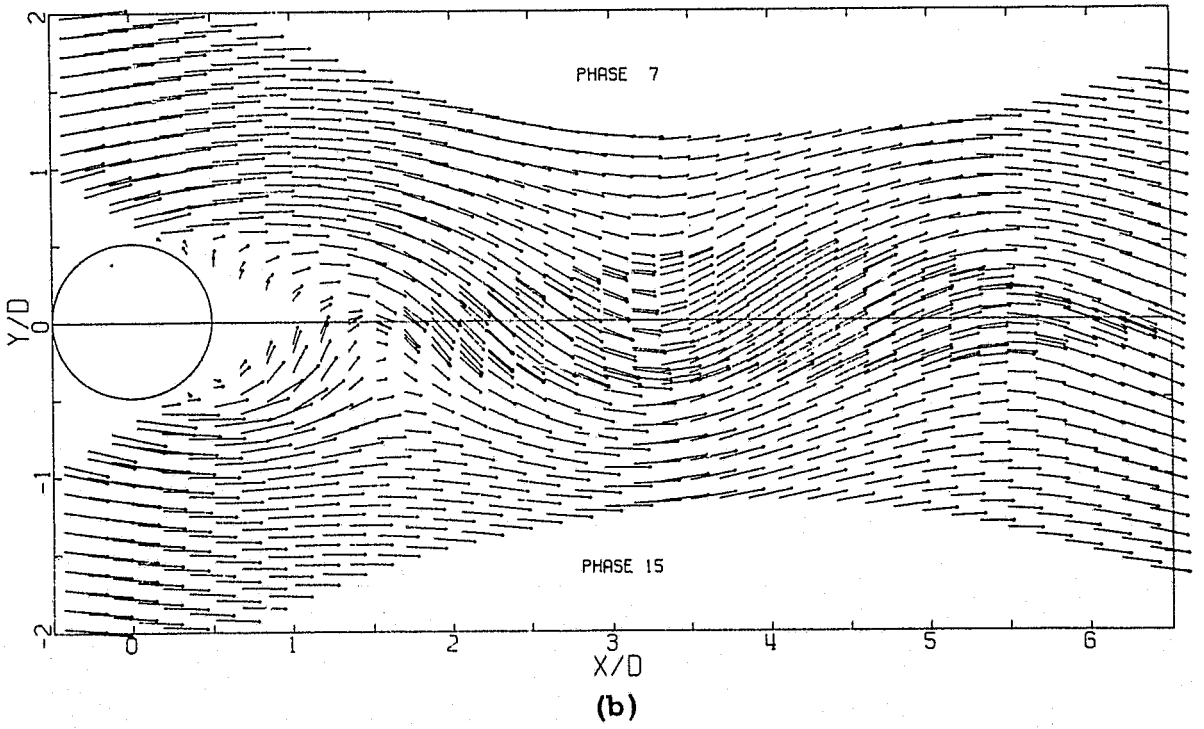

(b)

Figure 5.10 The velocity field at constant phase (7, 15) as viewed from a frame of reference: a) moving with the vortices, b) moving with the cylinder.

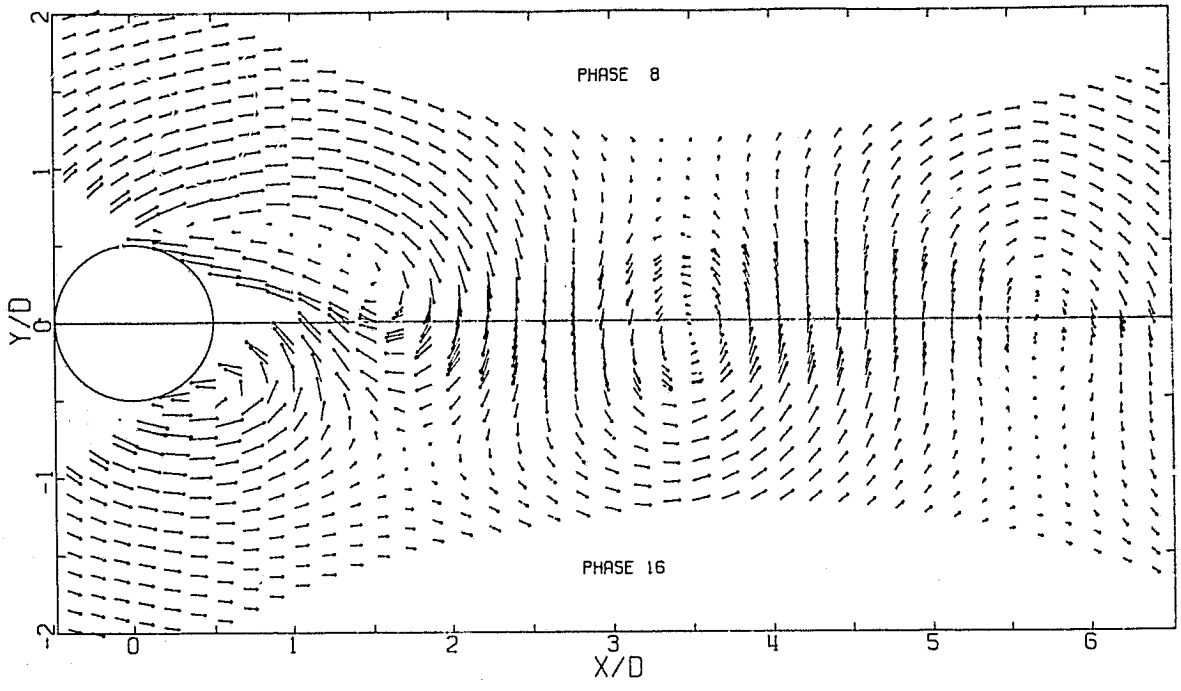

(a)

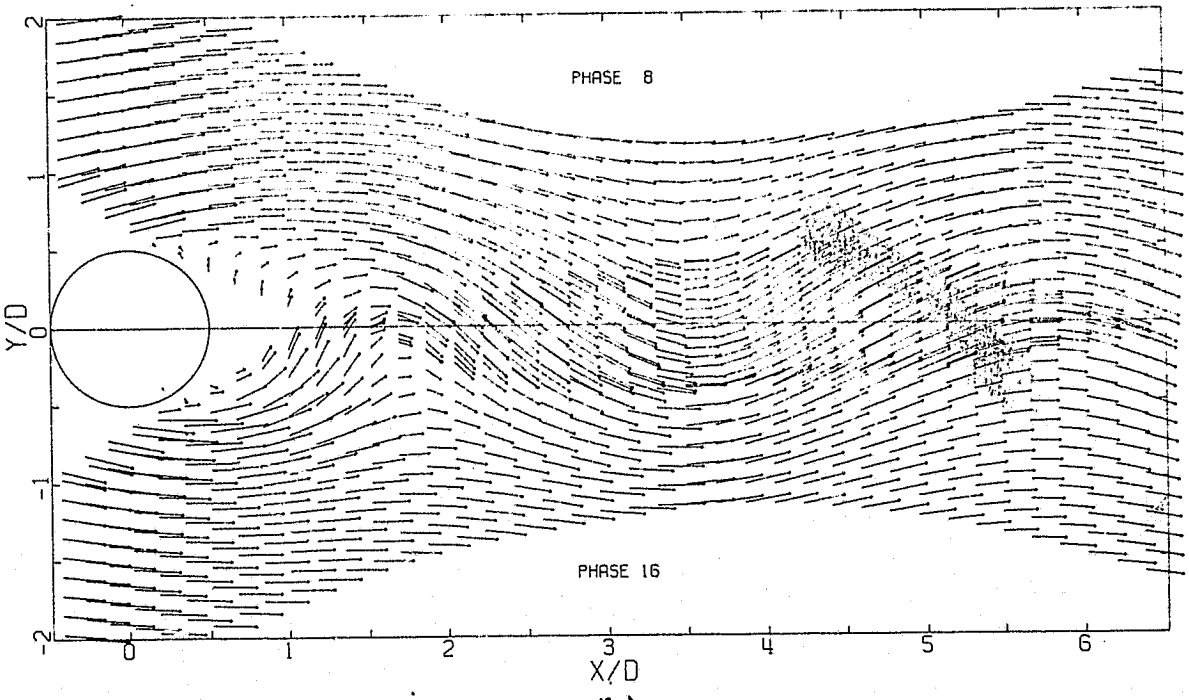

(b)

Figure 5.11 The velocity field at constant phase (8, 16) as viewed from a frame of reference: a) moving with the vortices, b) moving with the cylinder.

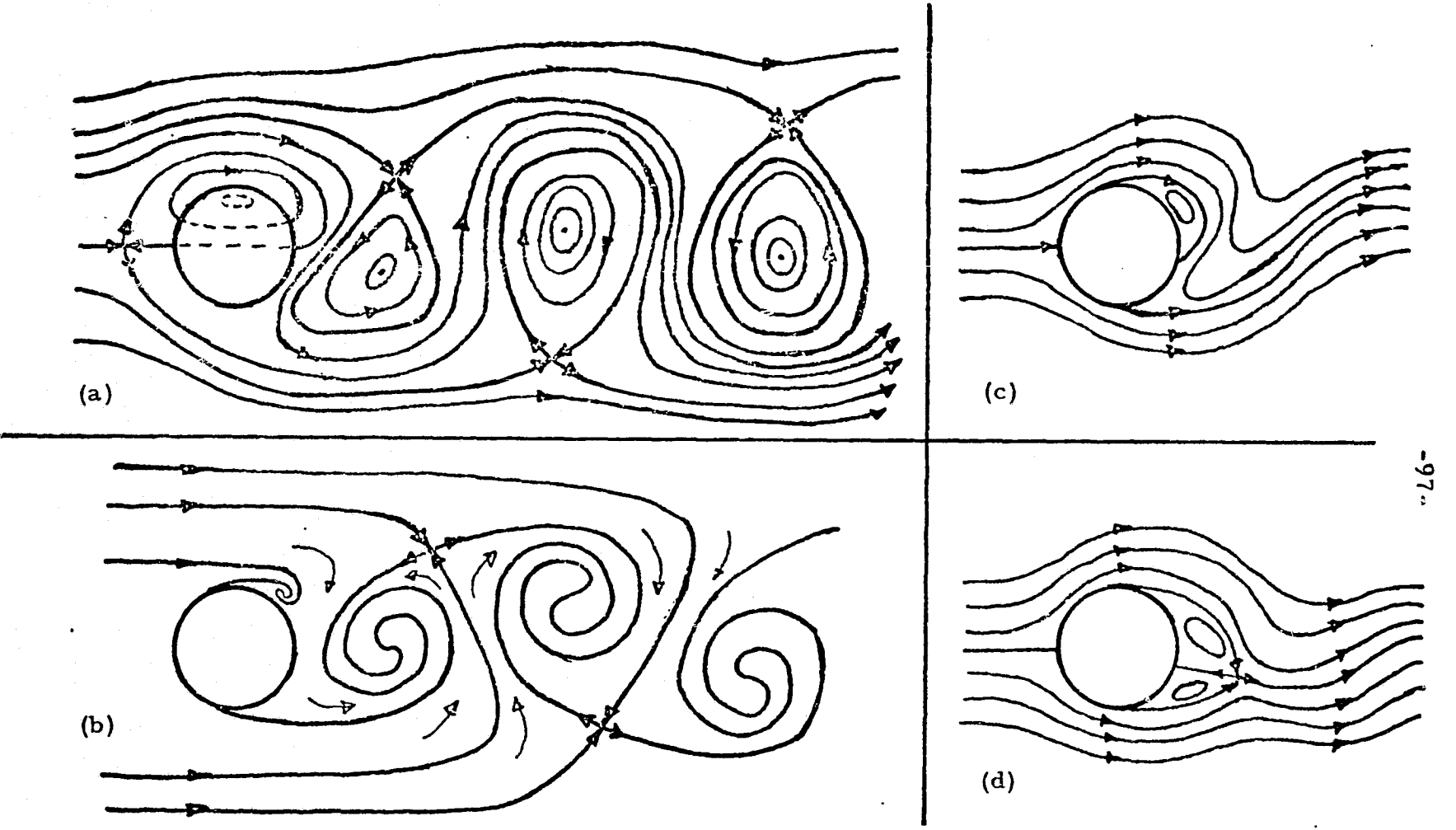

Figure 5.12 Sketches of a) streamlines in a frame of reference moving with the vortices; b) the roll up of material lines in the near wake; c) and d) two possible streamline patterns in the rest frame of the cylinder.

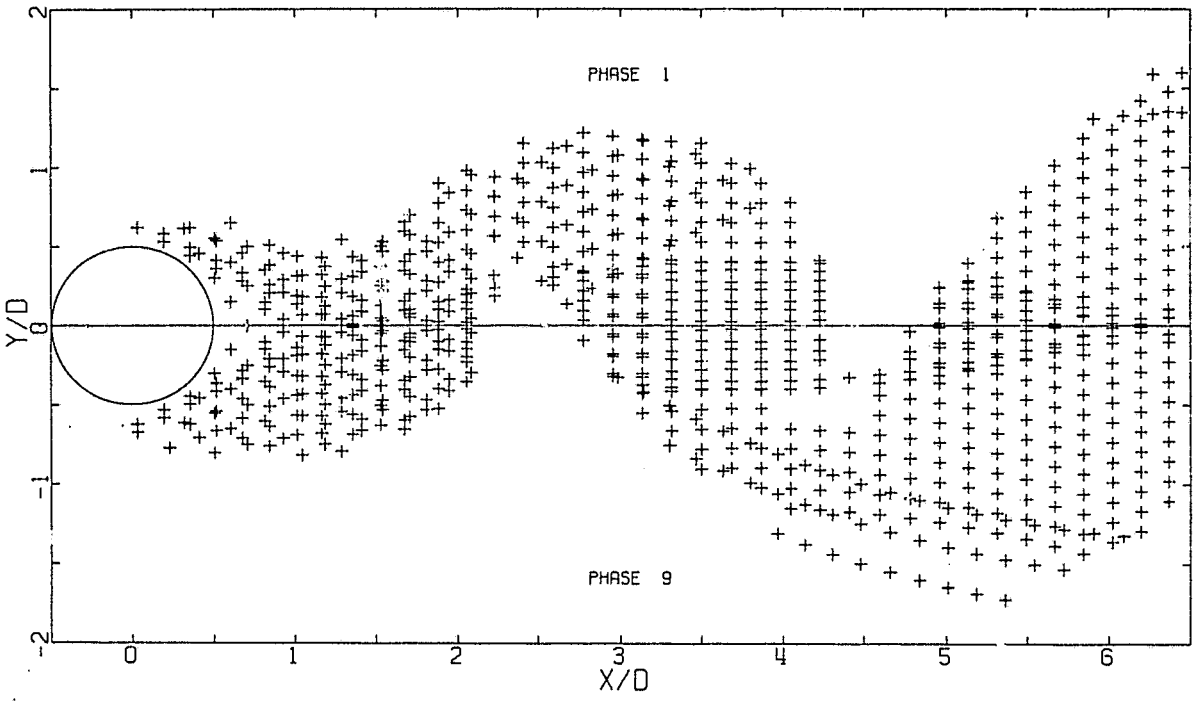

(a)

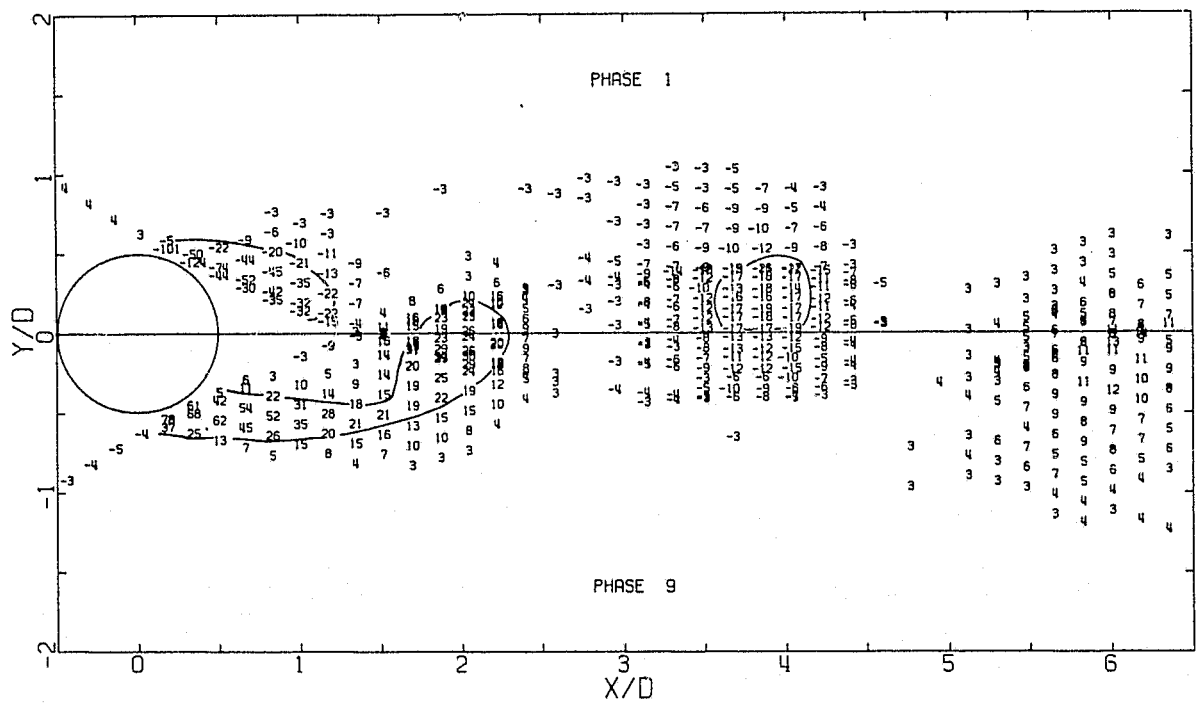

(b)

Figure 5.13 A view of the flow at constant phase (1, 9) in terms of a) regions where the intermittency factor was greater than 0.5 and b) the vorticity field, $(\omega D/U_\infty)*10$.

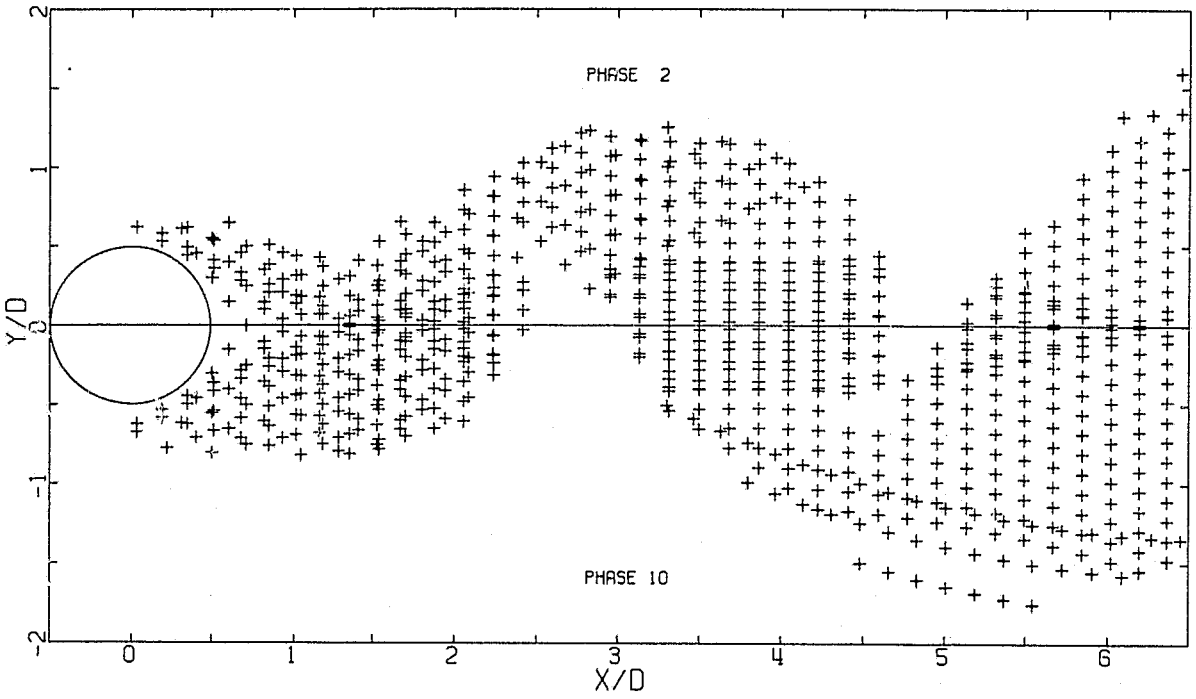

(a)

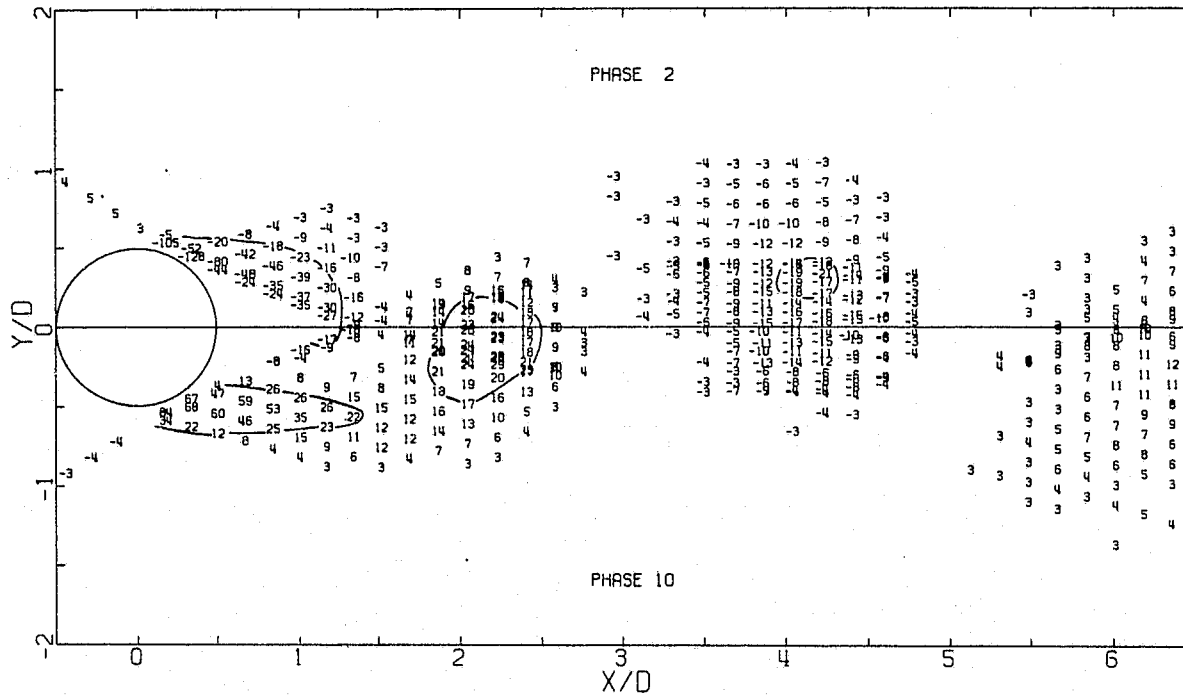

(b)

Figure 5.14 A view of the flow at constant phase (2 10) in terms of a) regions where the intermittency factor was greater than 0.5 and b) the vorticity field, $(\omega D/U_\infty)*10$

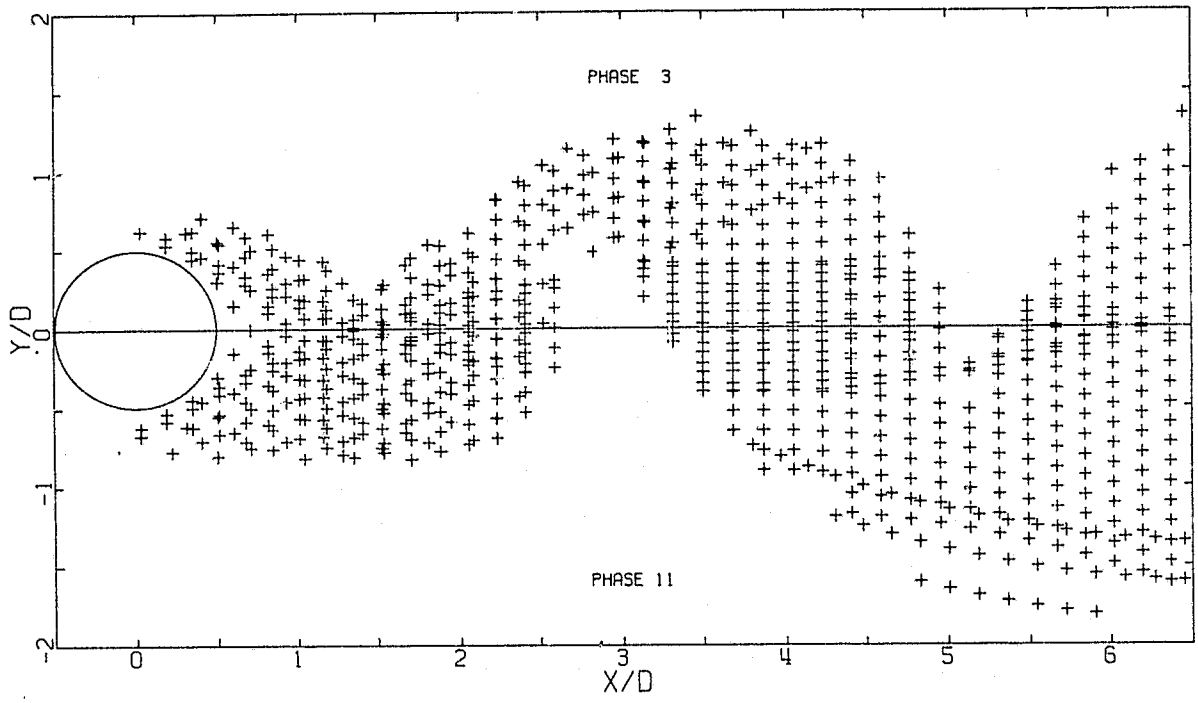

(a)

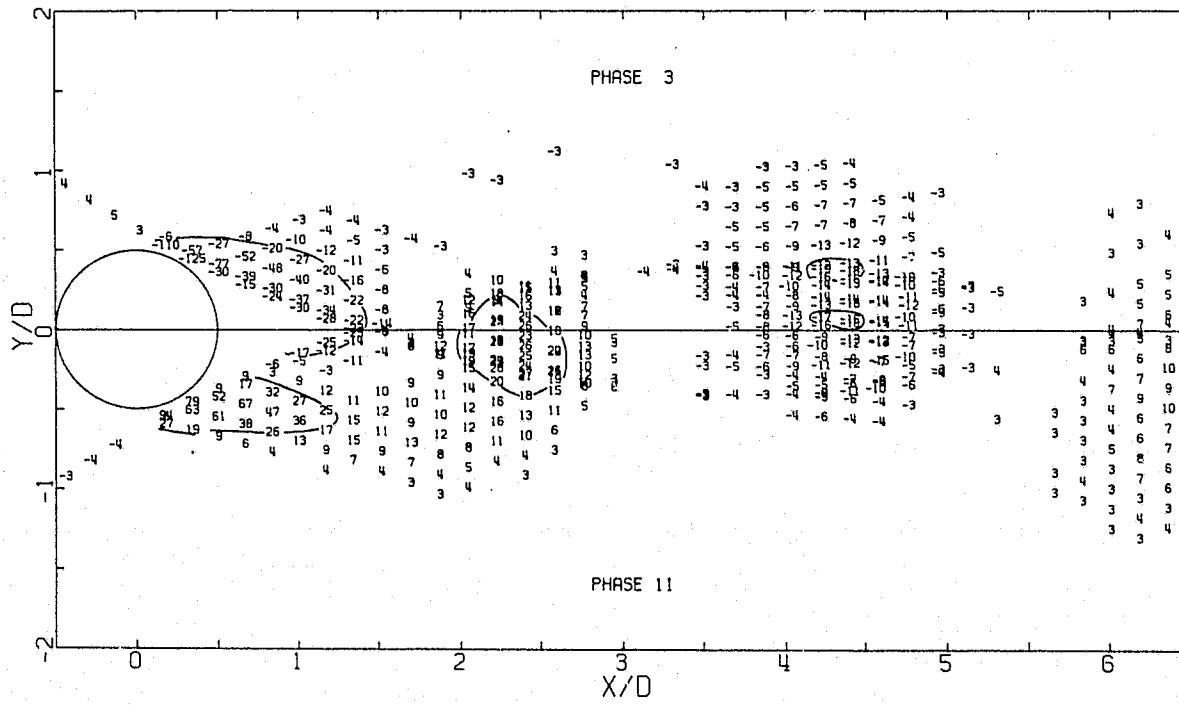

(b)

Figure 5.15 A view of the flow at constant phase (3, 11) in terms of a) regions where the intermittency factor was greater than 0.5 and b) the vorticity field, $(\omega D/U_\infty)*10$.

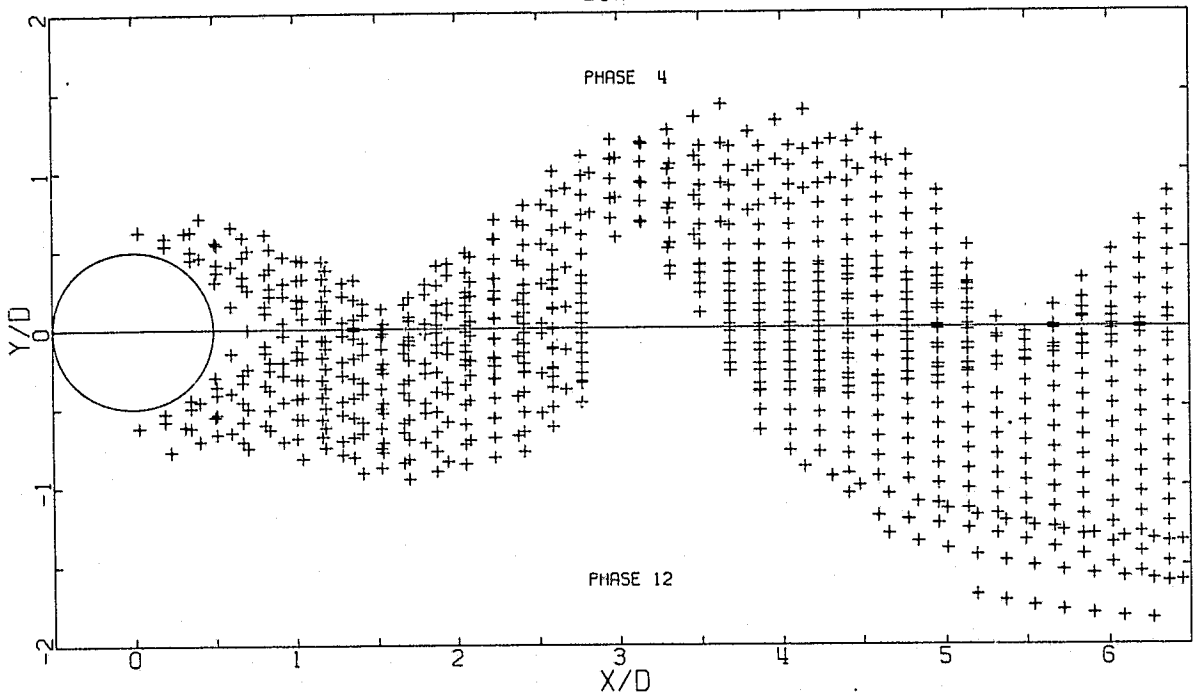

(a)

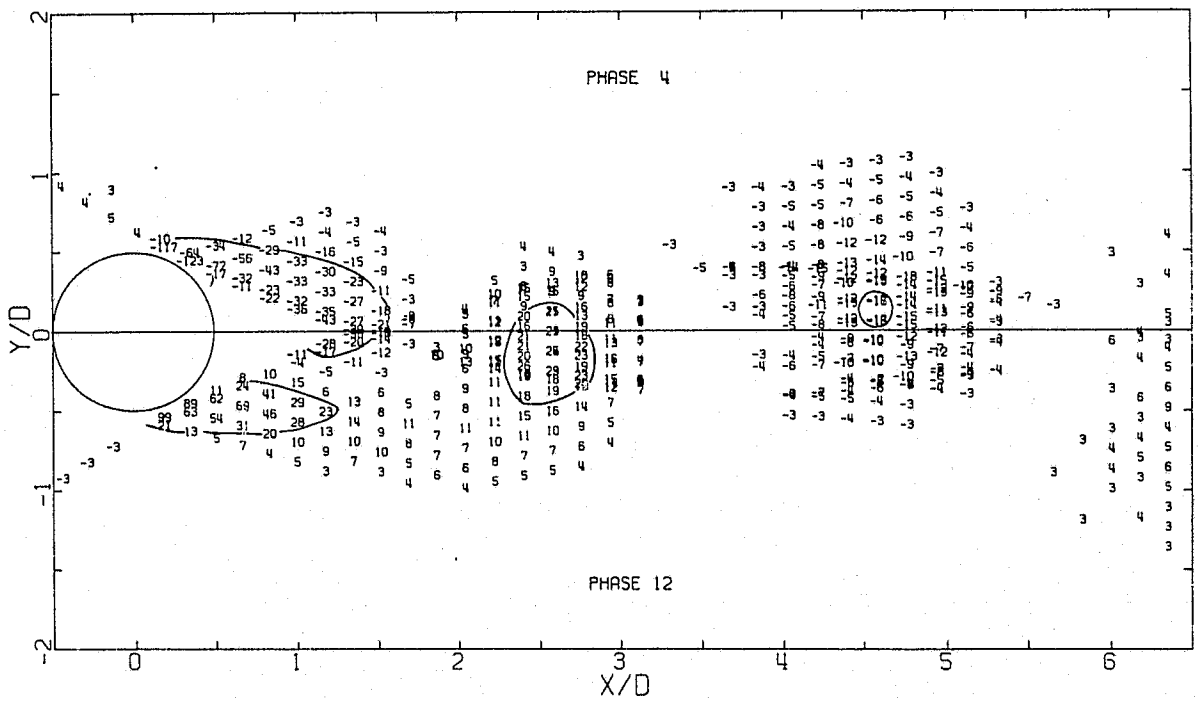

(b)

Figure 5.16 A view of the flow at constant phase (4, 12) in terms of a) regions where the intermittency factor was greater than 0.5 and b) the vorticity field, $(\omega D/U_\infty)*10$.

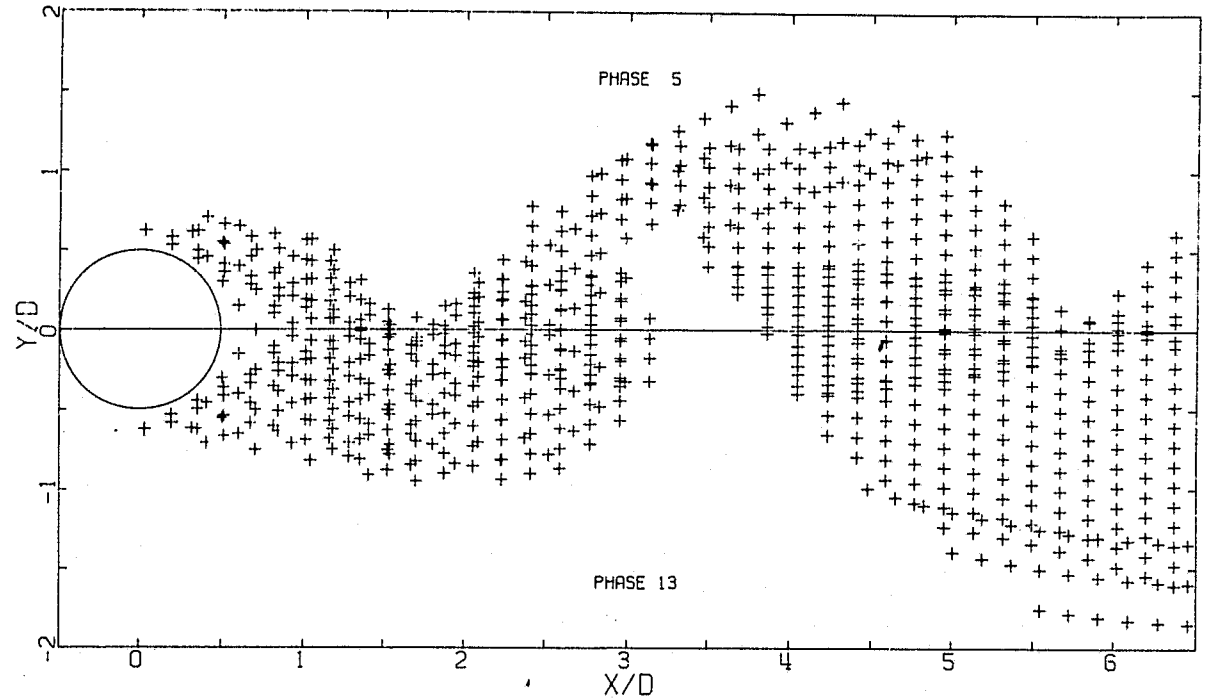

(a)

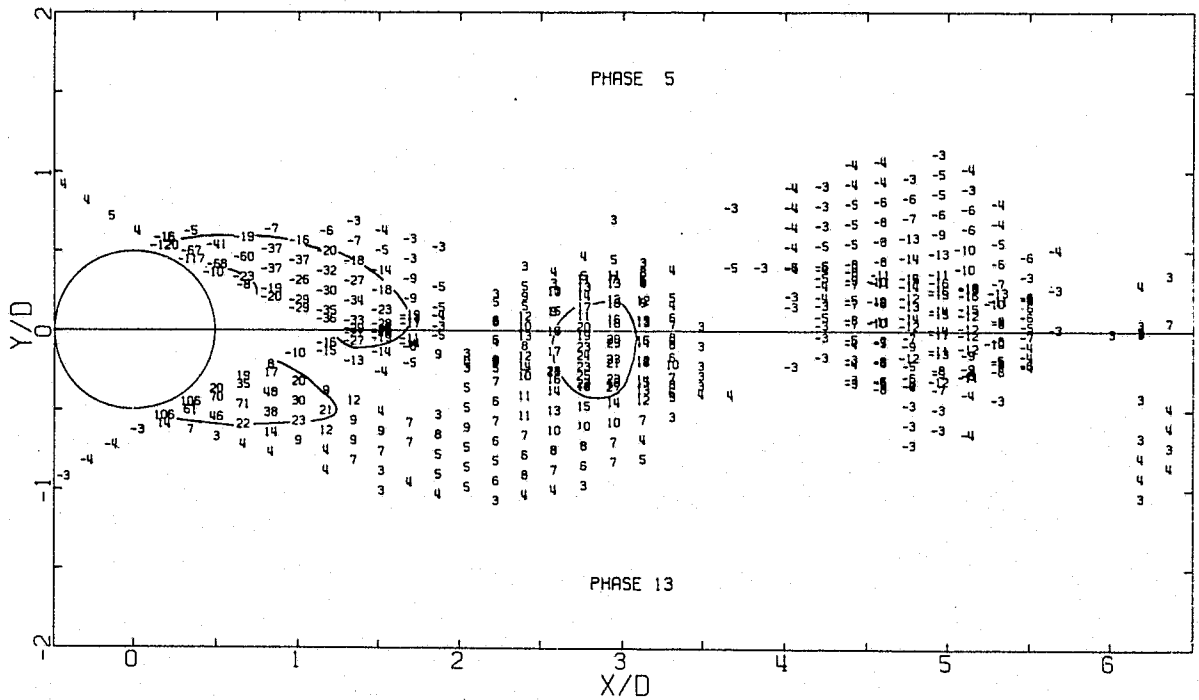

(b)

Figure 5.17 A view of the flow at constant phase (5, 13) in terms of a) regions where the intermittency factor was greater than 0.5 and b) the vorticity field, $(\omega D/U_\infty)*10$.

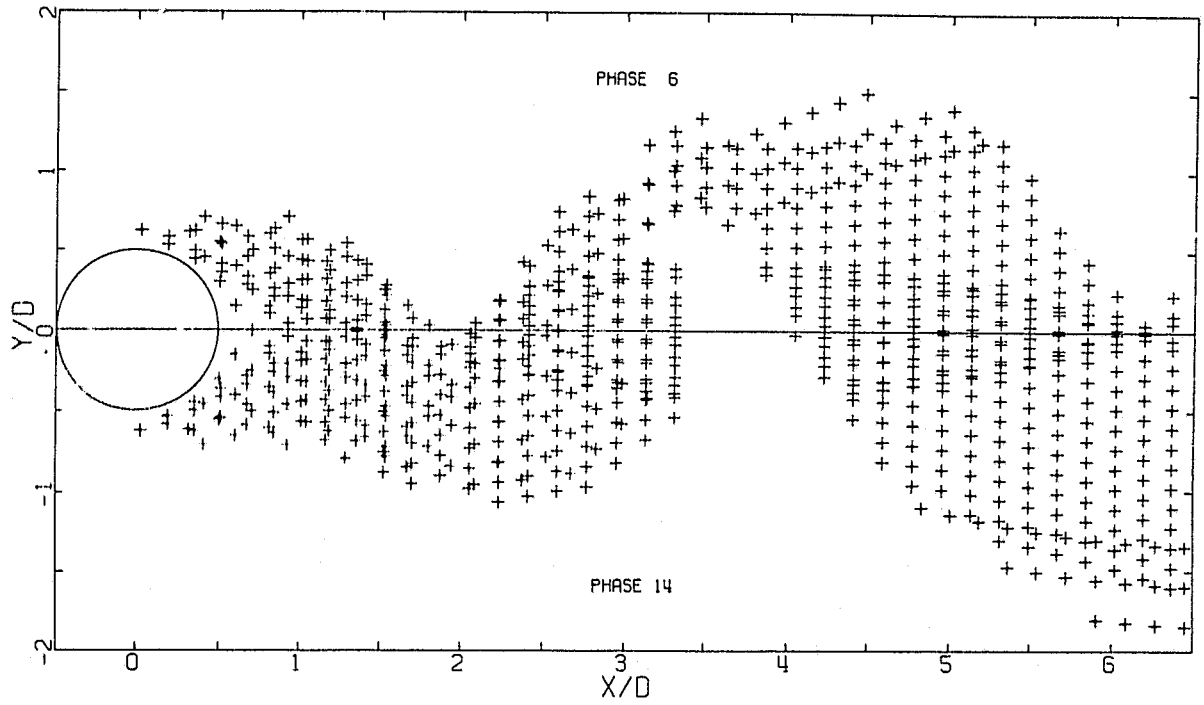

(a)

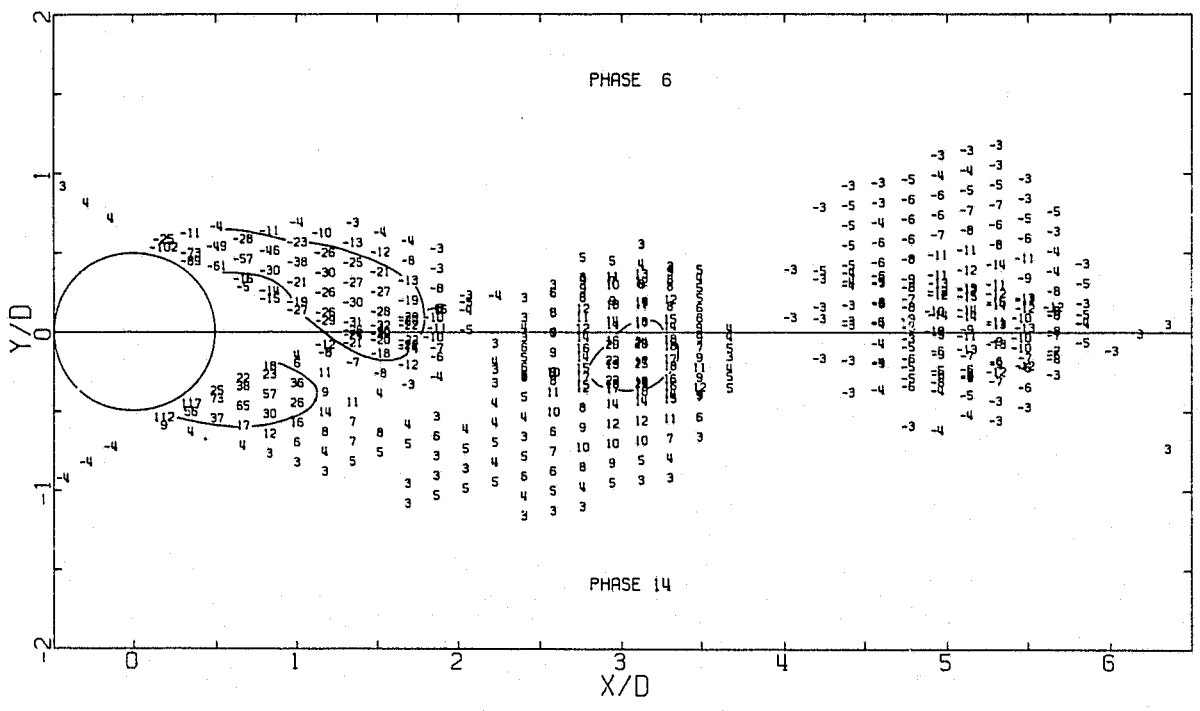

(b)

Figure 5.18 A view of the flow at constant phase (6, 14) in terms of a) regions where the intermittency factor was greater than 0.5 and b) the vorticity field, $(\omega D/U_\infty)*10$.

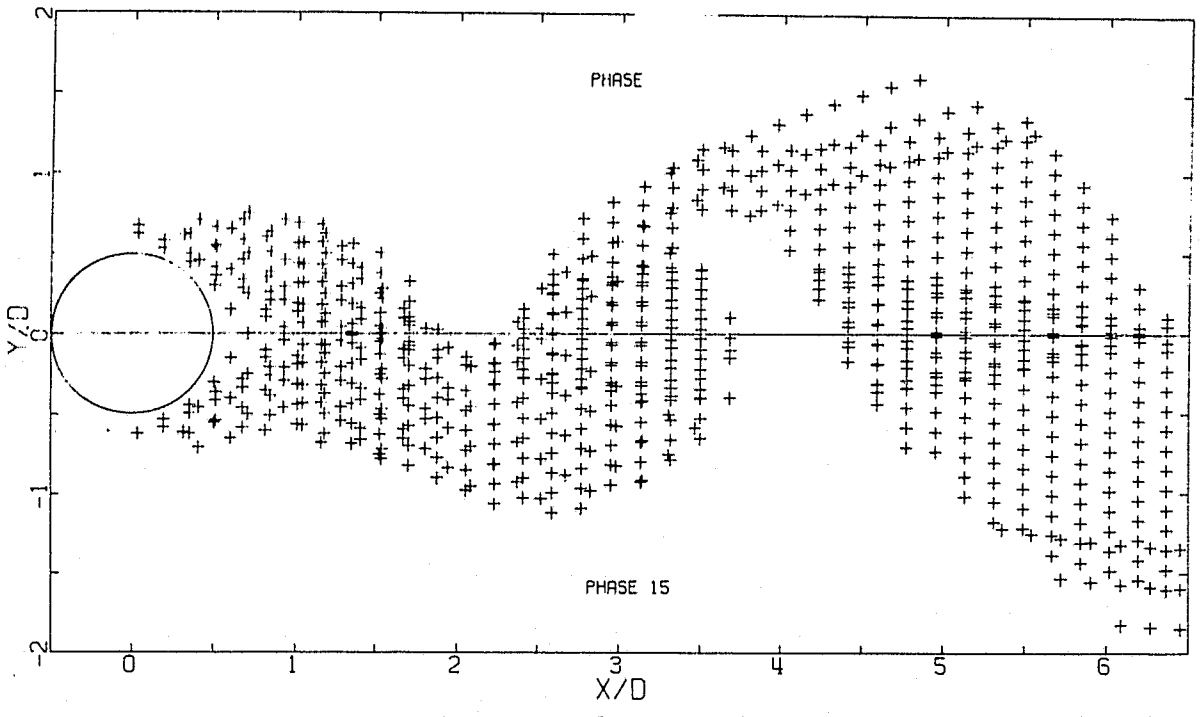

(a)

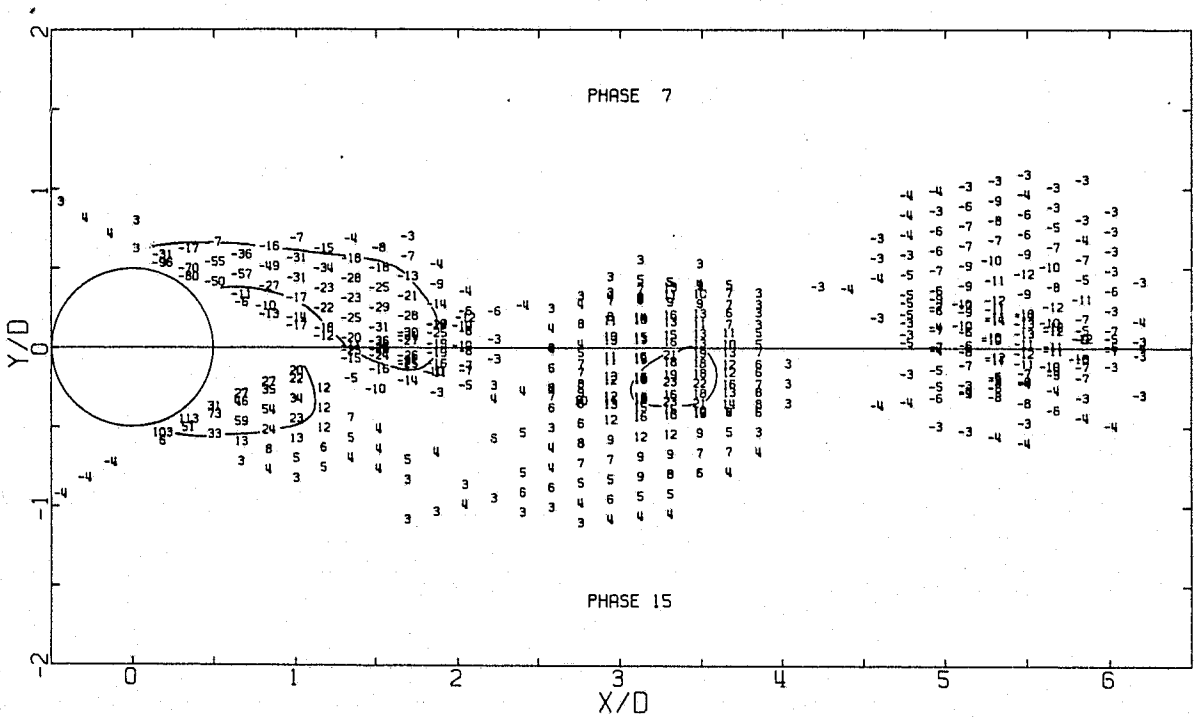

(b)

Figure 5.19 A view of the flow at constant phase (7, 15) in terms of a) regions where the intermittency factor was greater than 0.5 and b) the vorticity field, $(\omega D/U_\infty)*10$.

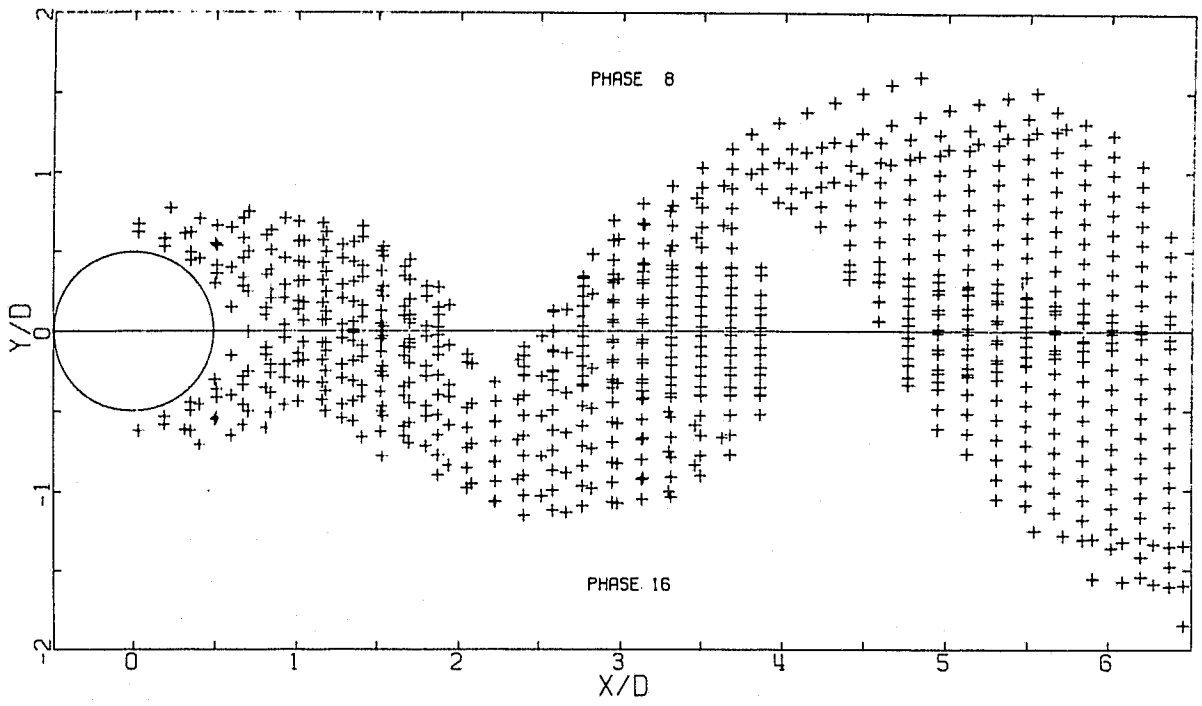

(a)

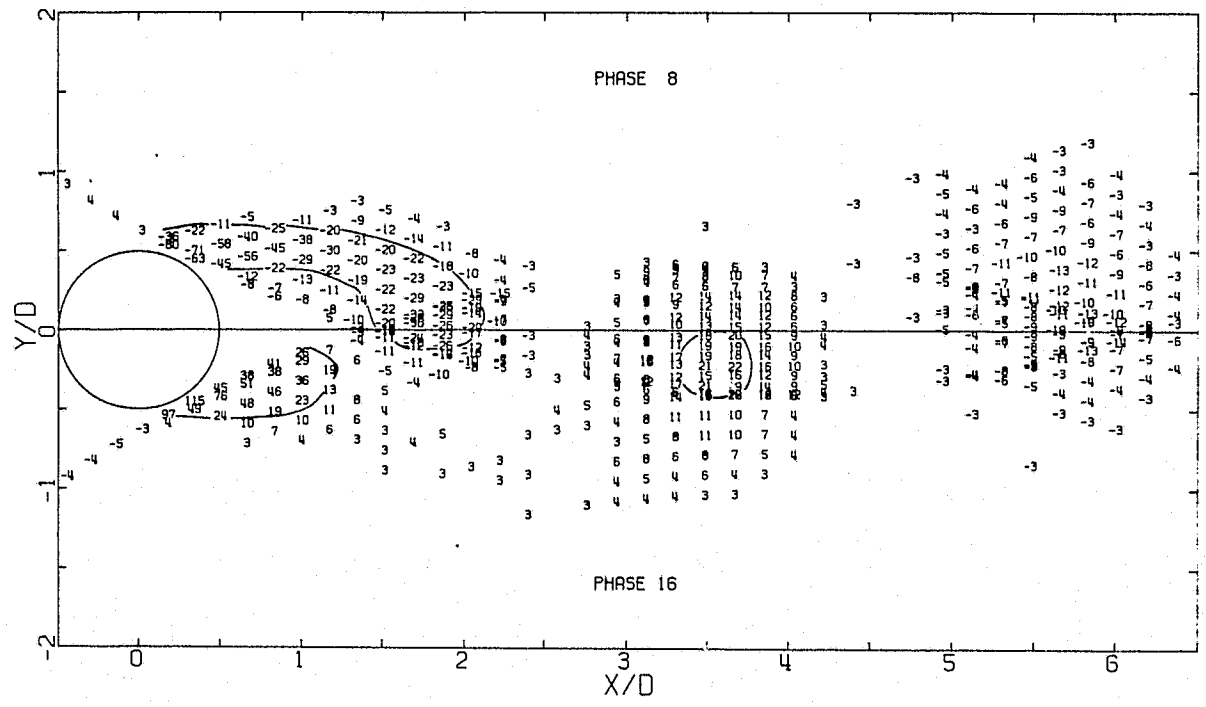

(b)

Figure 5.20 A view of the flow at constant phase (8, 16) in terms of a) regions where the intermittency factor was greater than 0.5 and b) the vorticity field, $(\omega D/U_\infty)*10$.

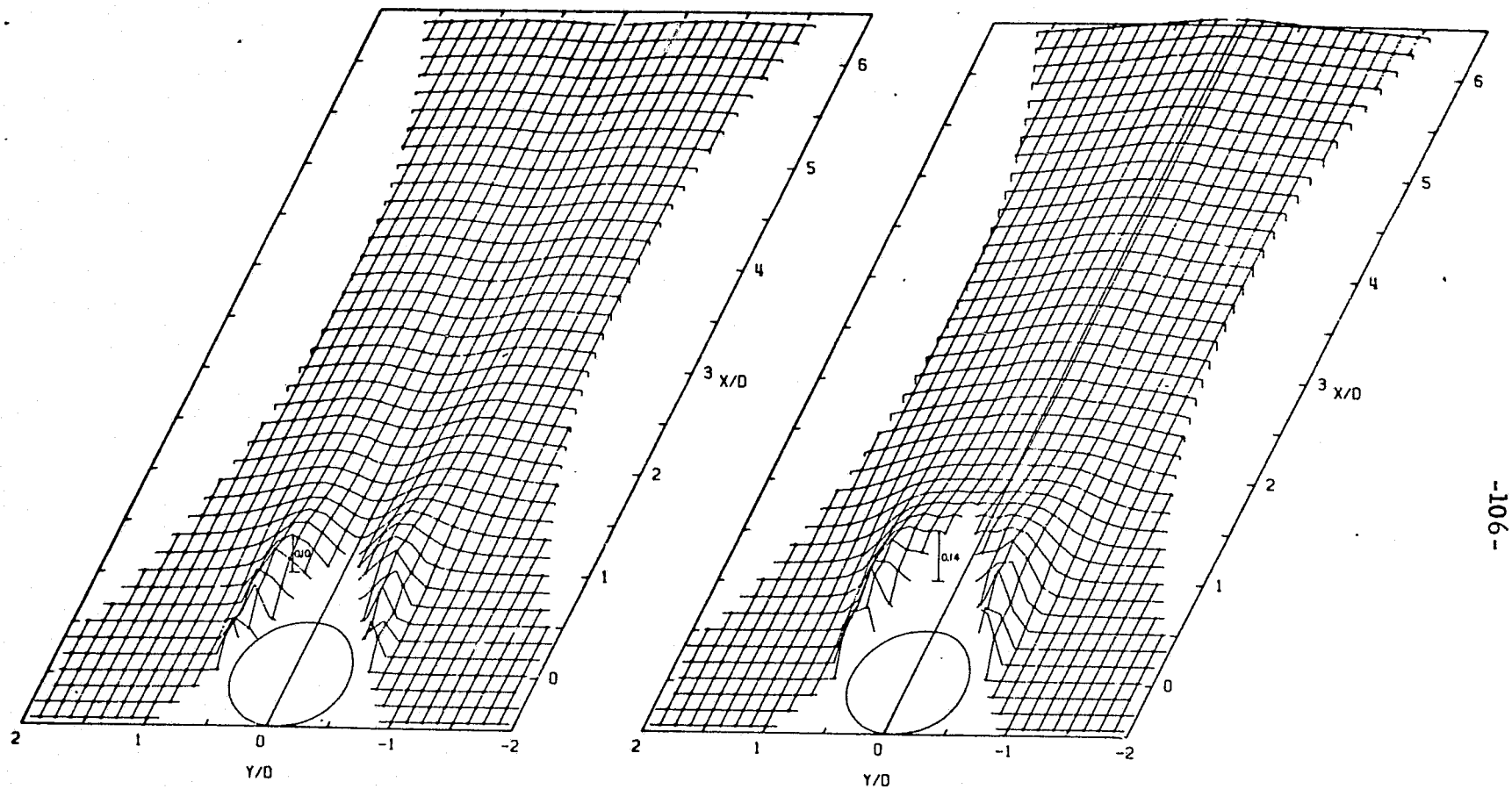

Figure 5.21 A three dimensional view of a) $\overline{\tilde{U}_1^2}/U_\infty^2$; b) $\langle\overline{U_1^2}\rangle/U_\infty^2$.

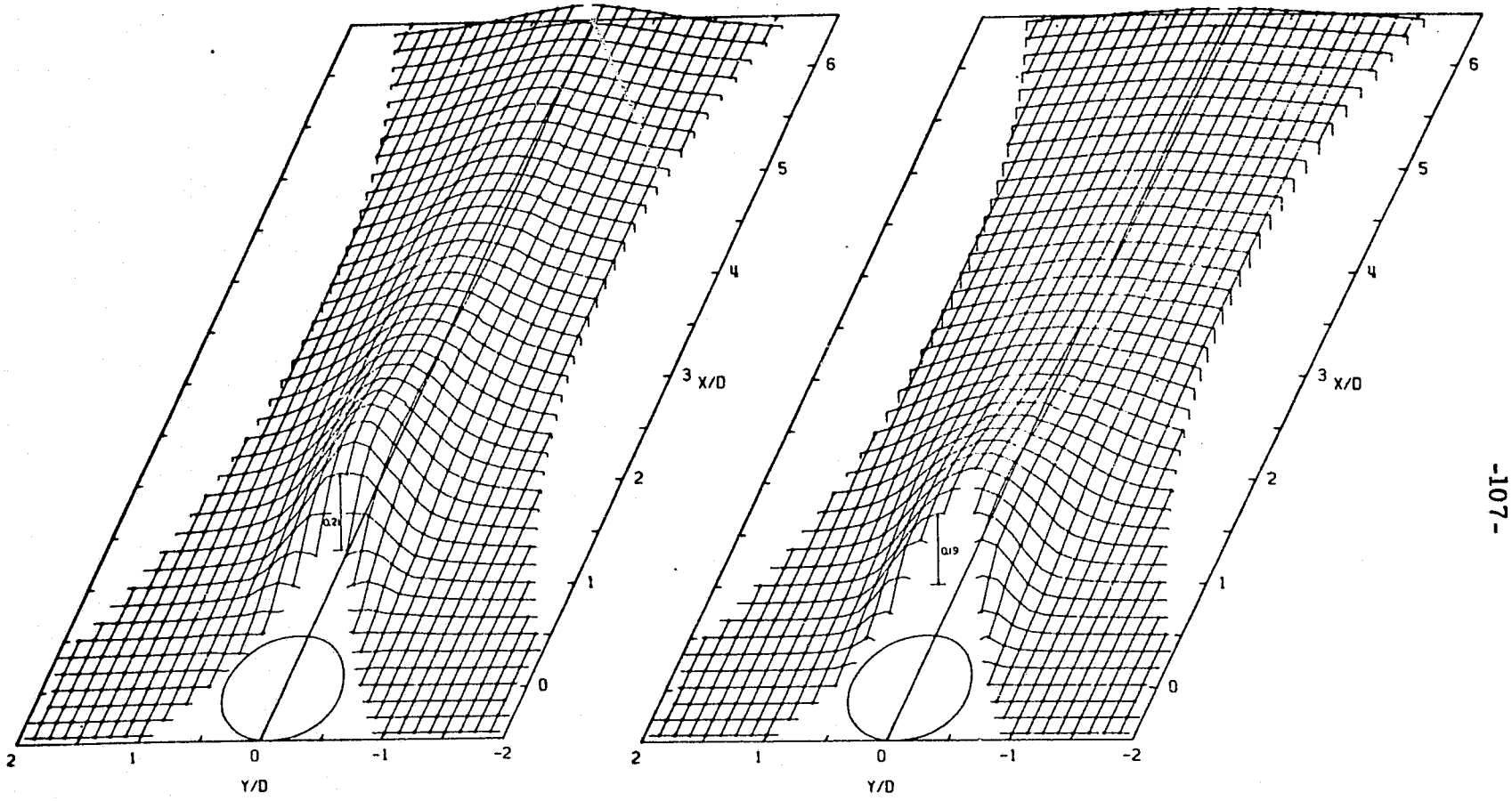

(a) (b)

Figure 5.22 A three dimensional view of a) $\overline{\tilde{U}_2^2}/U_\infty^2$; b) $\langle\overline{U_2'^2}\rangle/U_\infty^2$.

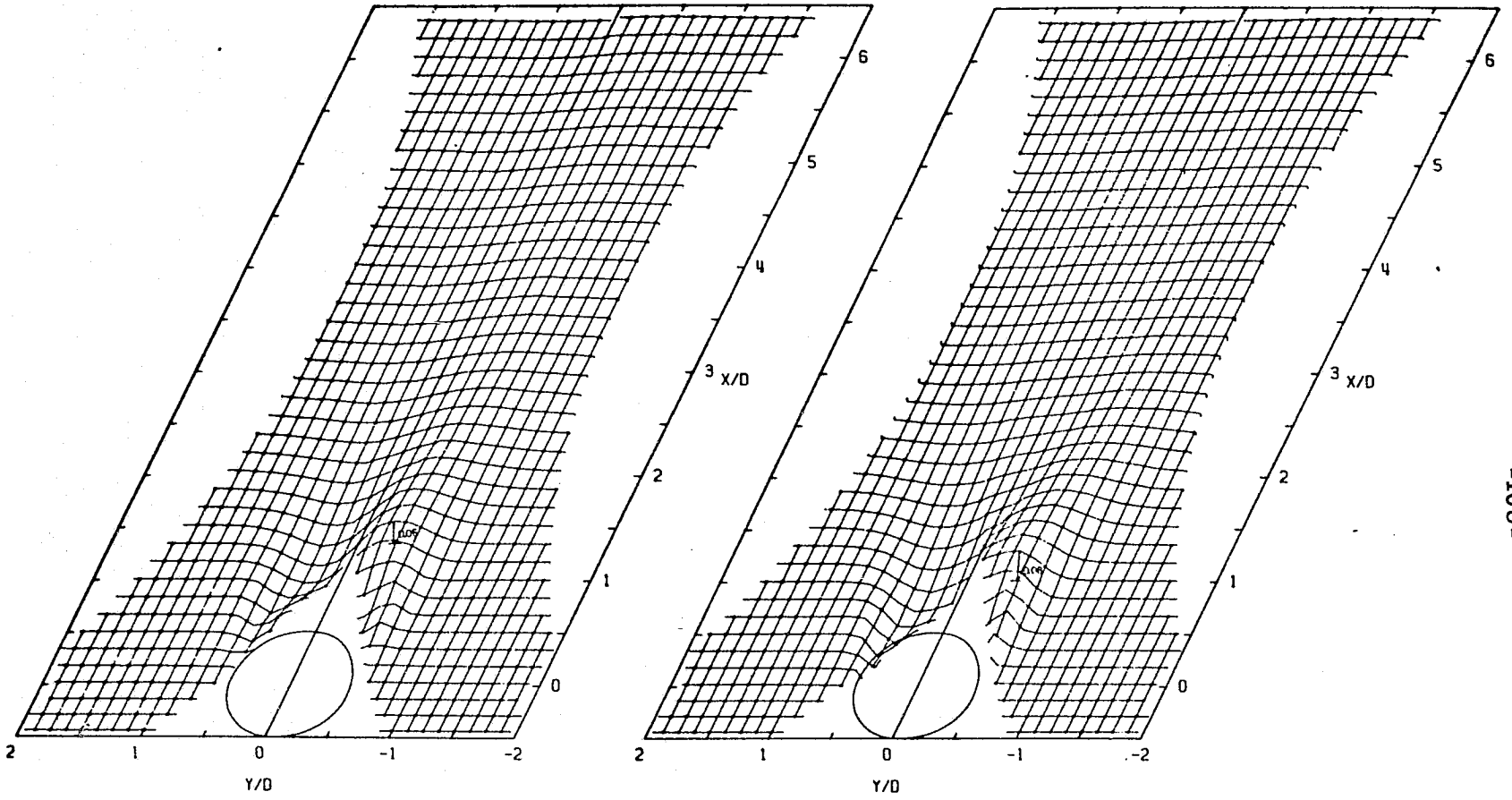

Figure 5.23 A three dimensional view of a) $\overline{\tilde{U}_1 \tilde{U}_2}/U_\infty^2$; b) $\overline{U'_1 U'_2}/U_\infty^2$.

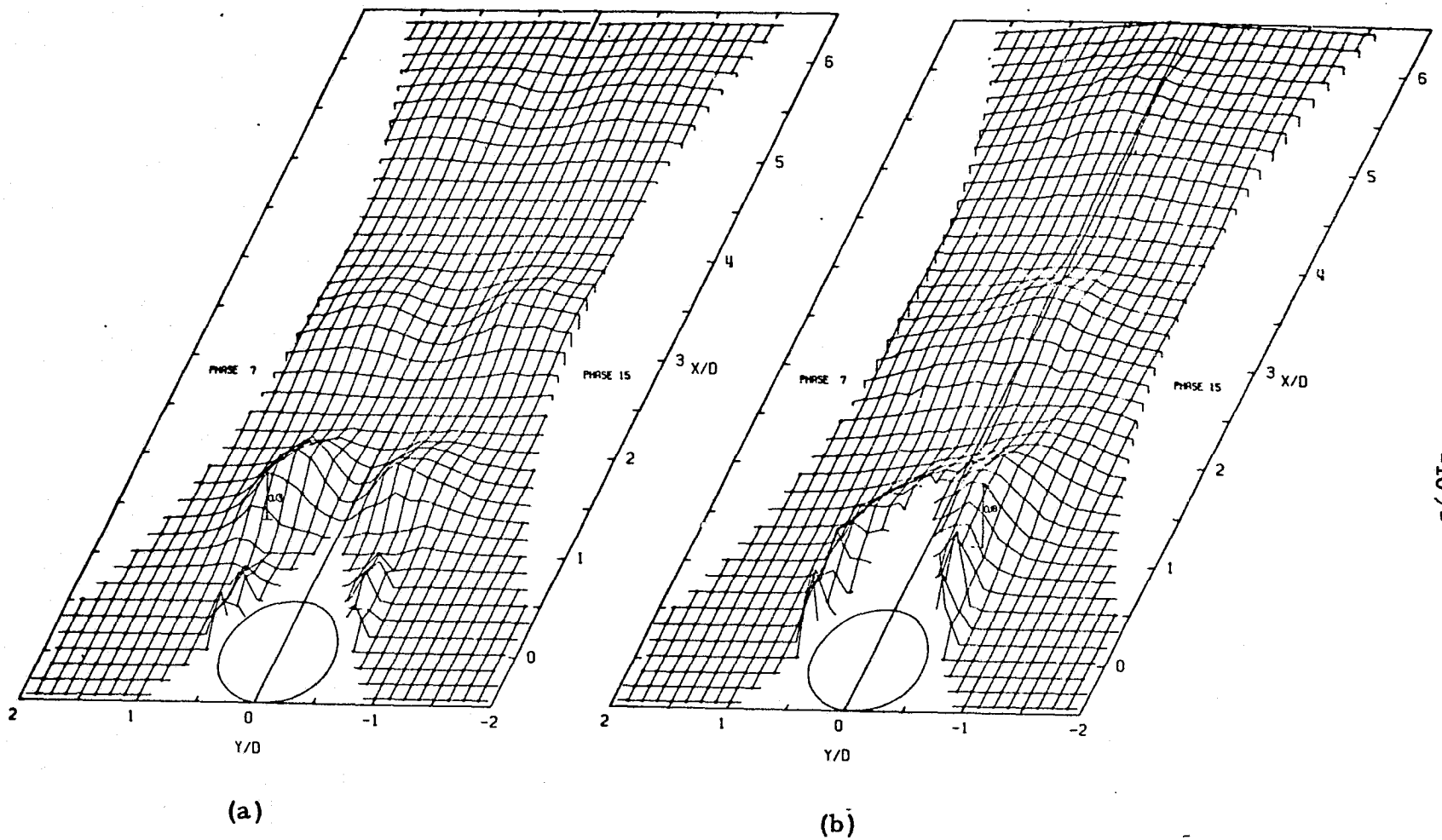

Figure 5.24 A three dimensional view of a) $\tilde{U}_1^2/U_\infty^2$; b) $\langle U_1'^2 \rangle/U_\infty^2$ at phase (7, 15).

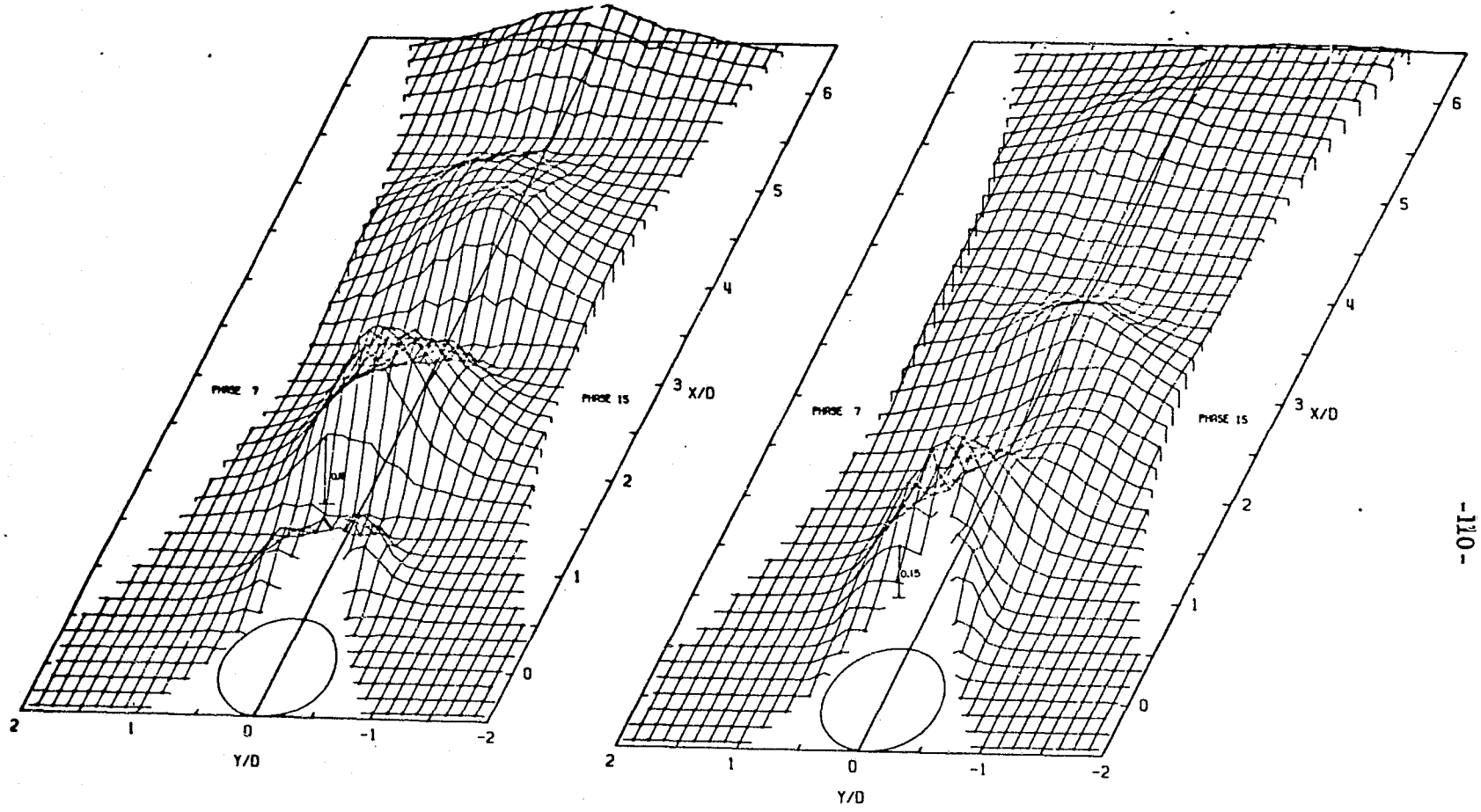

Figure 5.25 A three dimensional view of a) $\tilde{U}_2^2/U_\infty^2$; b) $\langle U'^2_2\rangle/U_\infty^2$ at phase (7, 15).

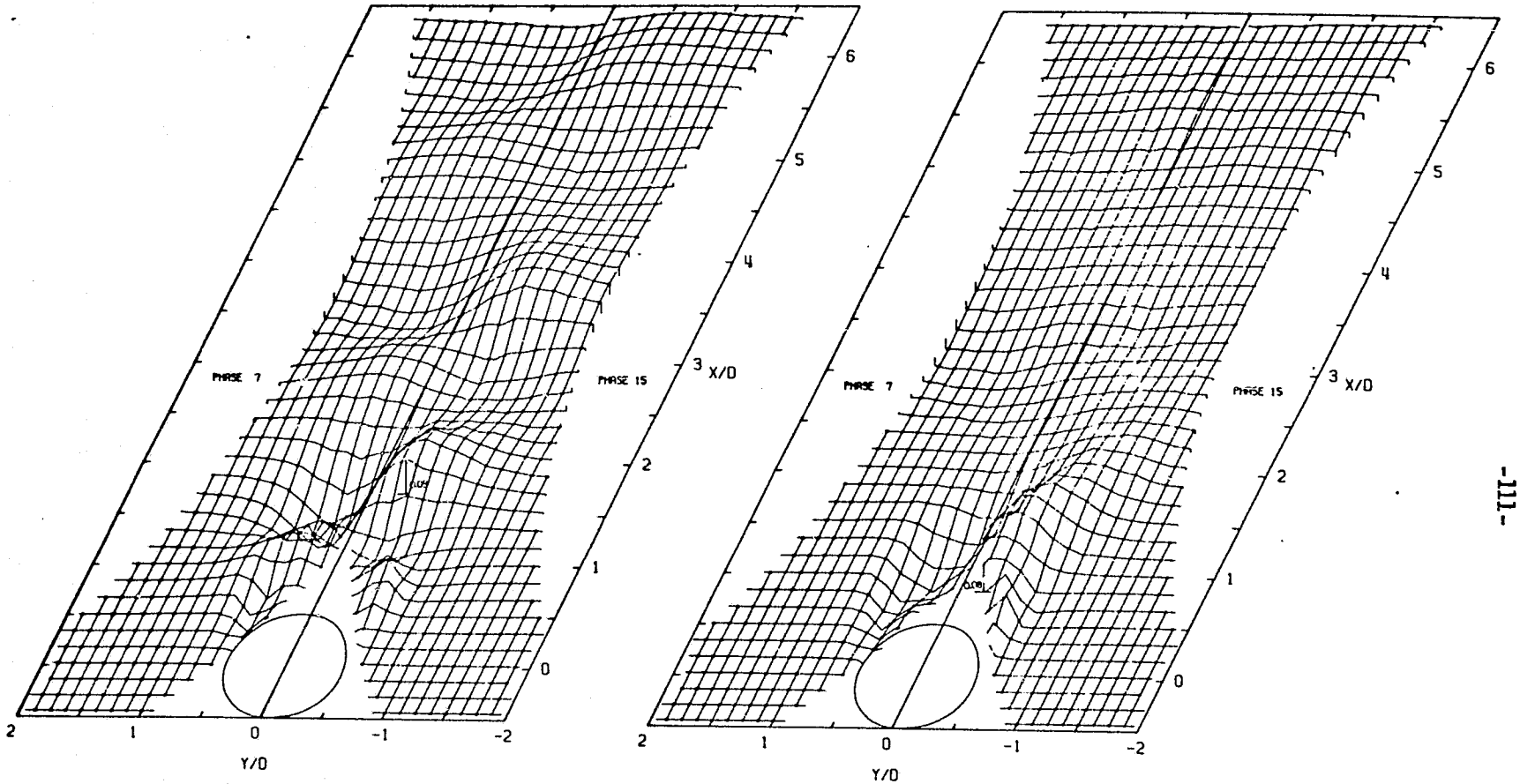

(a) (b)

Figure 5.26 A three dimensional view of a) $\tilde{U}_1\tilde{U}_2/U_\infty^2$; b) $\langle U'_1 U'_2\rangle/U_\infty^2$ at phase (7, 15).

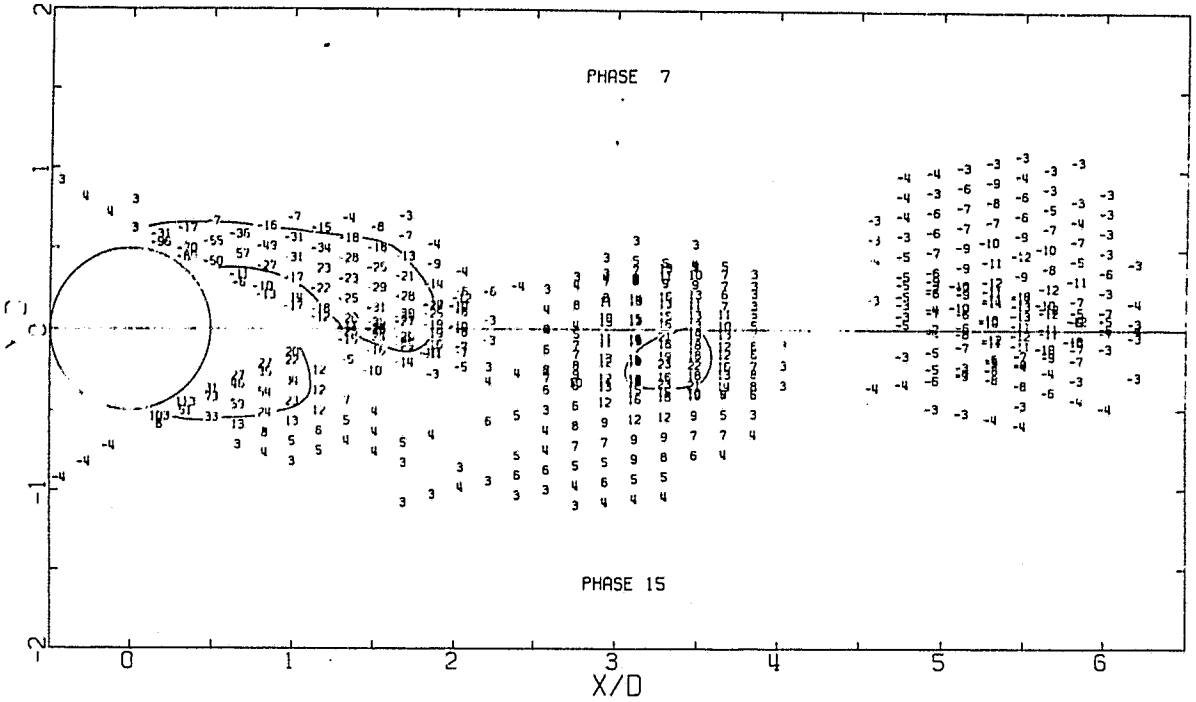

(a)

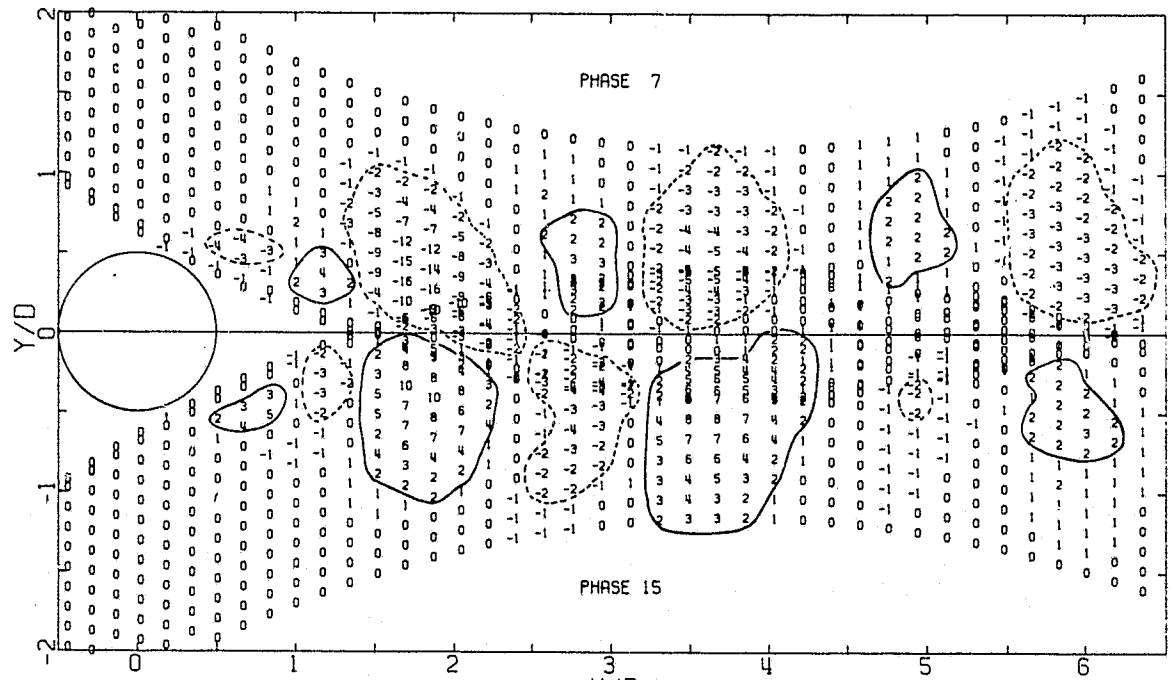

(b)

Figure 5.27 A plot of a) the vorticity field, $(\omega D/U_\infty)*10$ b) the large scale shear stress, $(\tilde{U}_1 \tilde{U}_2/U_\infty^2)*100$ at phase (7, 15). Dashed lines surround numbers less than -1. Solid lines surround numbers larger than 1.

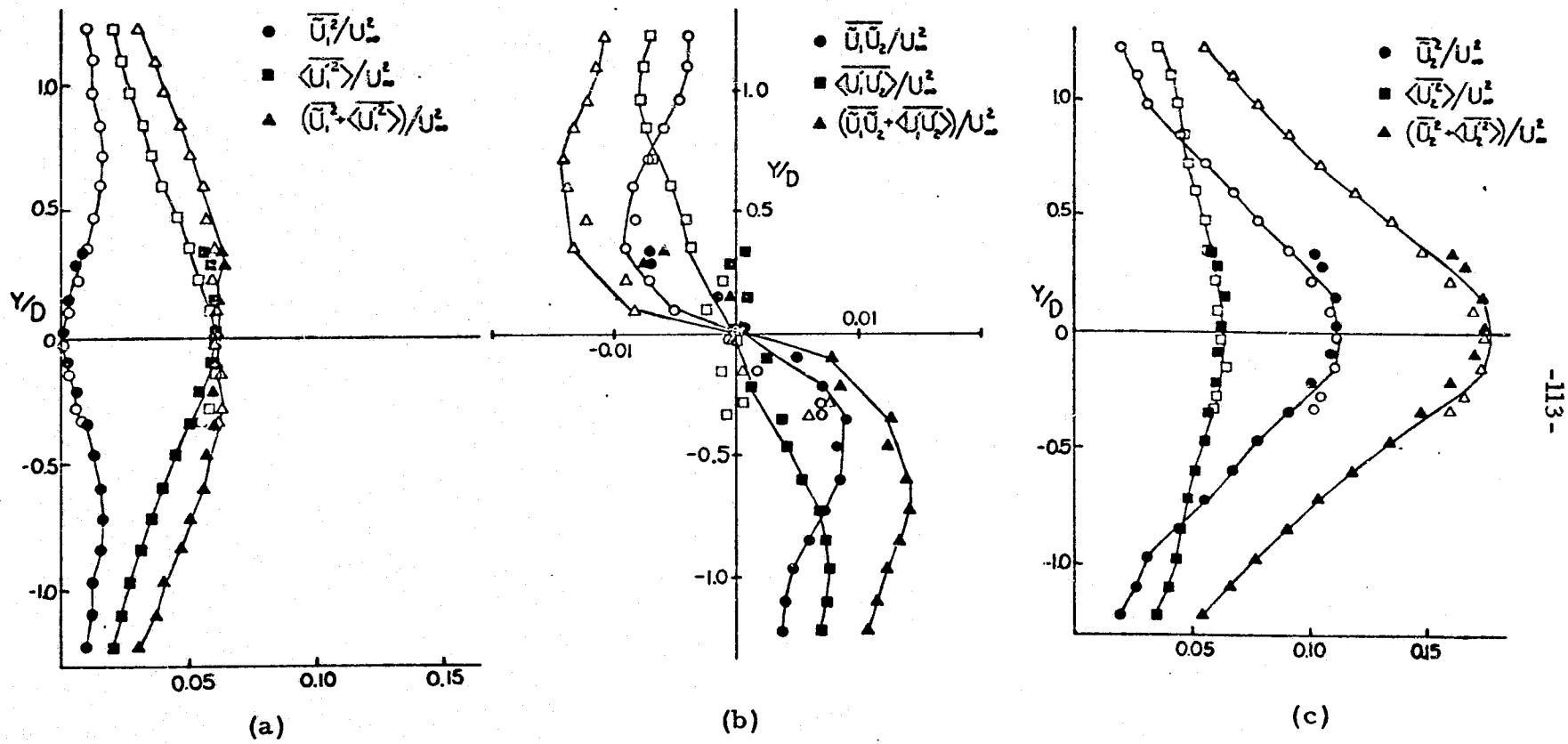

Figure 5.28 Three plots of the globally averaged Reynolds stresses versus Y/D at Frame 56 (X/D = 4.97)

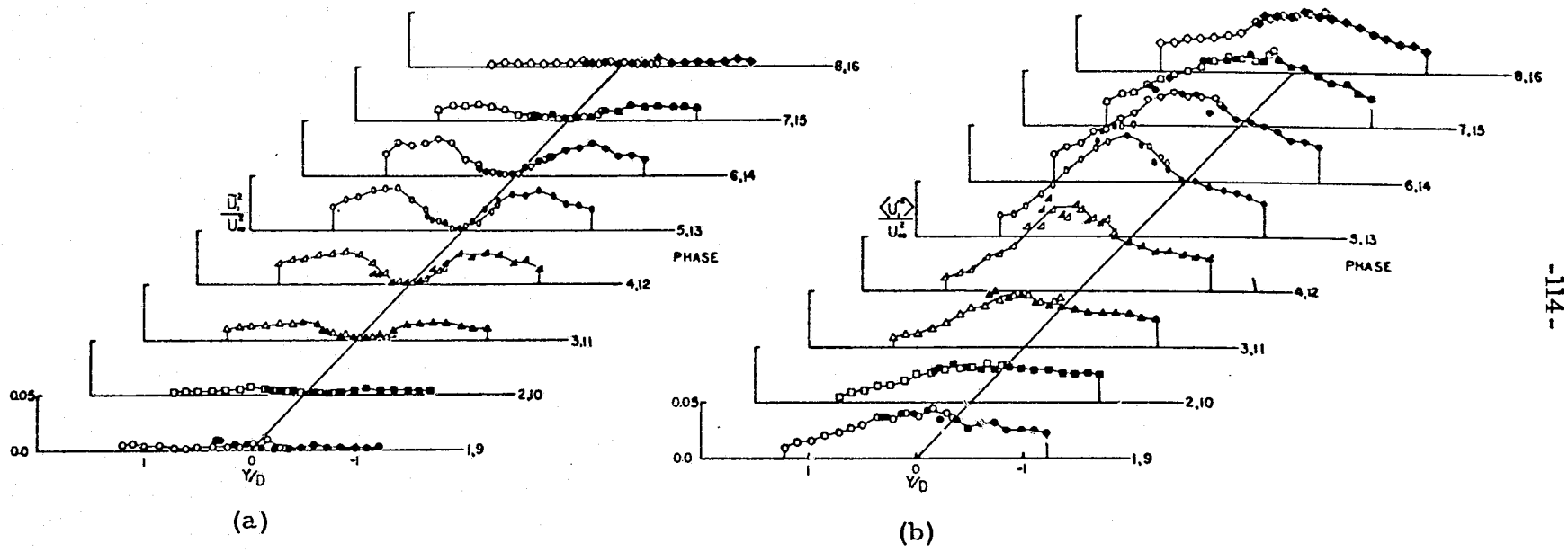

Figure 5.29 A plot of a) $\tilde{U}_1^2/U_\infty^2$; b) $\langle U_1'^2\rangle/U_\infty^2$ versus Y/D at frame 56 (X/D = 4.97), phases (1, 9)-(8, 16). Solid points represent values of Y/D where data were actually taken; open points represent the reflection of data points about the wake centerline.

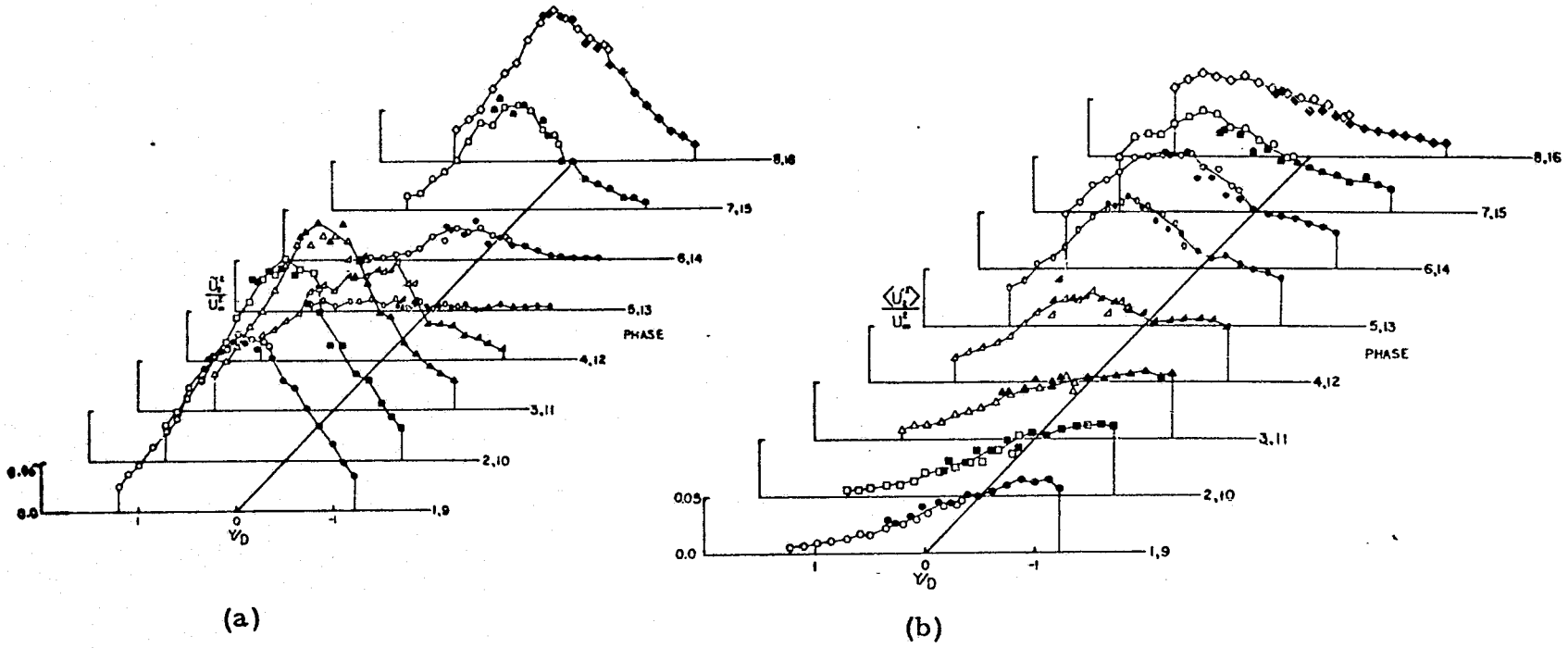

Figure 5.30 A plot of a) $\tilde{U}_2^2/U_\infty^2$; b) $\langle U'^2_2\rangle/U_\infty^2$ versus Y/D at frame 56 (X/D = 4.97), phases (1, 9)-(8, 16). Solid points represent values of Y/D where data were actually taken; open points represent the reflection of data points about the wake centerline.

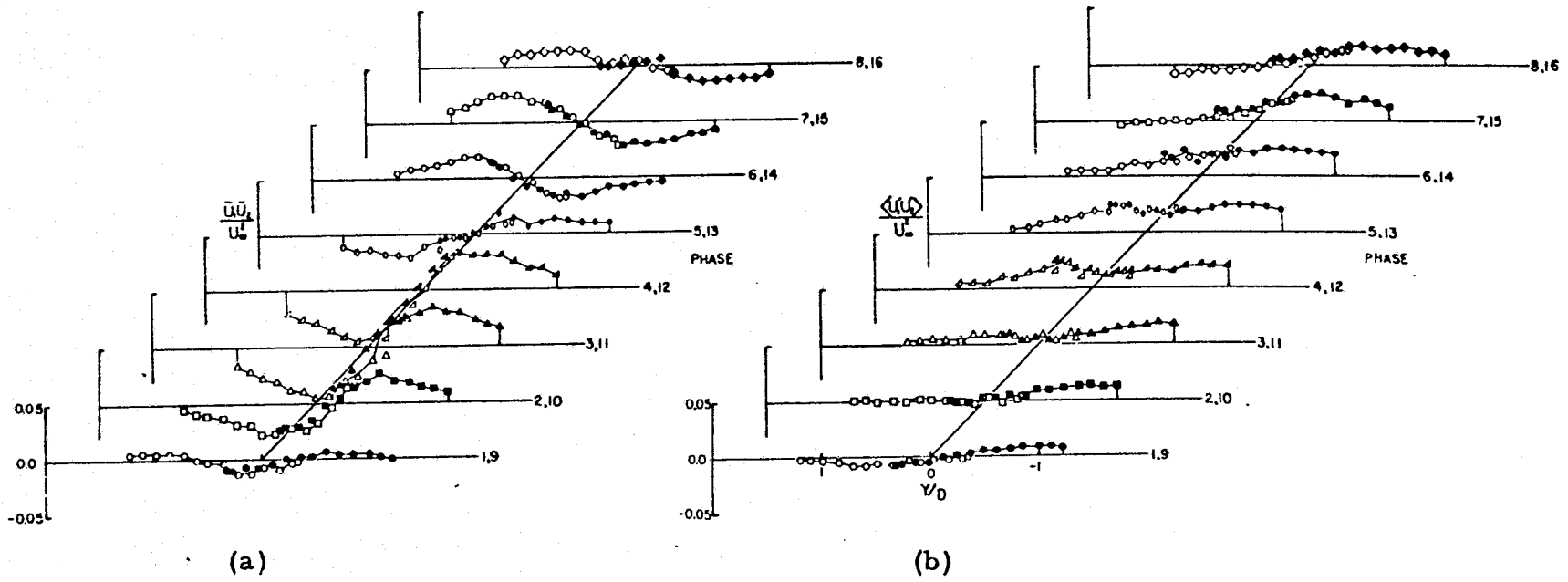

Figure 5.31 A plot of a) $\tilde{U}_1\tilde{U}_2/U_\infty^2$; b) $\langle U'_1U'_2\rangle/U_\infty^2$ versus Y/D at frame 56 (X/D = 4.97), phases (1, 9)-(8, 16). Solid points represent values of Y/D where data were taken; open points represent the reflection of data points about the wake centerline.

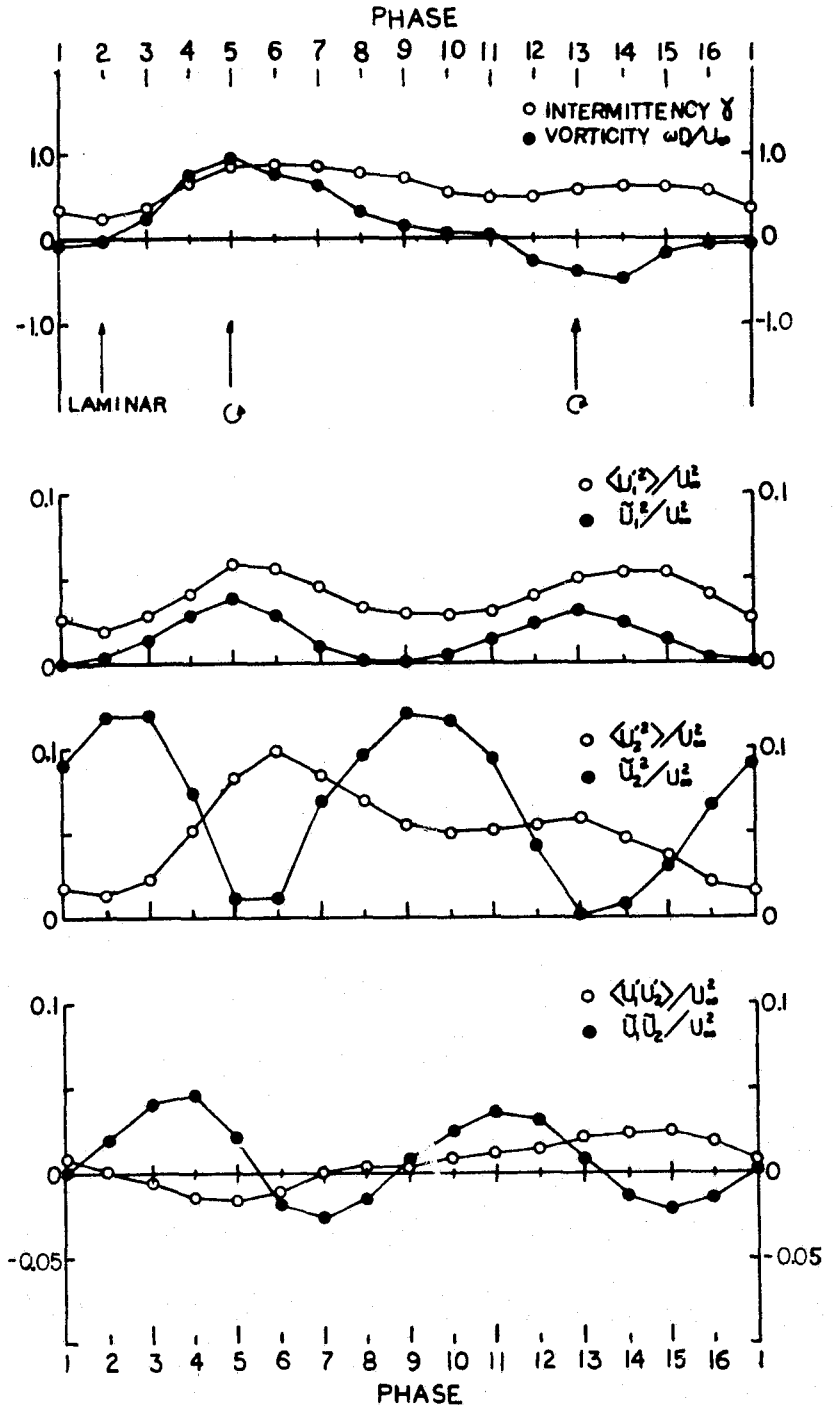

Figure 5.32 The history of stress, vorticity and intermittency at one off-axis point at frame 56 (X/D= 4.97, Y/D= -0.72).

VI. CONCLUSIONS

The conclusions of the flying hot wire study of the cylinder near wake at a Reynolds number of 140,000 are described in the following numbered paragraphs.

1. The main conclusion with regard to the flying hot wire technique is that, while it is a somewhat complicated and unwieldy apparatus to use, it can be effective in making measurements in highly turbulent flows involving large excursions in flow direction. The issue concerning the disturbance of the flow field by the rotating arms remains largely unresolved. The same apparatus was used to measure the separated flow around a stalled airfoil and some early results from this experiment suggest a displacement of the flow when the probe moves through the separated region at large angles of attack. No such effect is observed in the results of the cylinder experiment. However, in this case, most of the measurements were made along arcs which were at a fairly gentle angle to the mean flow. Some of the discrepancies between velocity vectors measured along different arcs in Figure 5.2 could be explainable on the basis of a disturbance to the flow caused by the probe moving on an arc which is at a large angle of attack to the mean flow direction.

2. The main difficulty with the apparatus came from drift in the hot wire calibrations. The self-calibrating feature of the flying hot wire was useful in compensating for drift, but the problem, nonetheless, dictated the use of a fairly unsophisticated mathematical form for the inversion of voltage pairs to velocity pairs, one which

could be altered from tape to tape using the rather limited amount of information found on each arc outside the disturbance region of the wake. The source of the drift remains unknown. However, the most likely source appears to be the platinum plated tungsten wire material. It is well known that plain tungsten wires drift badly due to oxidation, and the purpose of the platinum plating is to prevent this. However, flaws in the plating, caused during manufacture or during the installation of the wire on the probe, could expose areas of tungsten where oxidation might take place. Another source of drift may come from the presence of fibers of synthetic material which may catch on the wire and melt, thereby changing the heat transfer characteristics of the wire.

3. Perhaps the most important conclusion with regard to the apparatus is that this sort of experiment would have been completely out of reach without the aid of fast, direct A to D data conversion together with on-line access to a computer. The unique timing and data handling requirements of the flying hot wire technique render it almost useless without such data acquisition capabilities. One of the problems with computerized data acquisition during an ongoing experiment is that it is not possible to take advantage of the highly redundant, self-checking and self-correcting features of the system. You have to take what you get and live with it. If the capstan slips while writing data on a magnetic tape there is no opportunity to go back and rewrite the record correctly. In an experiment like the one described in this thesis, where vast quantities of data are required, such accidents happen and allowance must

be made for them. Handles for finding bad or improperly formatted data should be built into the apparatus and the software before the experiment is undertaken and not ad-libbed later. The recording of a voltage standard, in addition to the experimental data, is a most effective and painless way of detecting data errors. Keeping track of the maximum and minimum voltages measured on a particular channel is also helpful in isolating errors. The experience of the cylinder experiment is that anomalies in the data can be expected to occur at a rate of about one every 15-20 million words (not bad, but more than the one part in 10^8 quoted by the manufacturer). Although most of these occur in the form of tape parity errors, several improperly formatted records were discovered which were not associated with parity errors. In addition, there are four or five inexplicable cases of a single isolated word of data having been written down as all zeros.

4. The technique of ensemble averaging at a constant phase, used to discriminate between the large scale vortices and background turbulence, appears to be an effective means for studying periodic turbulent flows. The evidence of the turbulent and large scale Reynolds stresses described in the previous chapter is a fairly good indication that separation of the two phenomena has been achieved. However, there is a conflict on this point which has to do with the fact that the intermittency factor averaged at constant phase does not go to one at the centers of each of the vortices. In fact, $\gamma = 1$ only in a small region very close to the base of the cylinder. This is difficult, if not impossible, to explain without

allowing for some dispersion in the vortices, and indeed the aperiodicity in the vortex shedding surface pressure signal would indicate that there must be dispersion. The source of the dispersion has not been identified. The sheet of vortical fluid which separates from the cylinder surface is probably far from two dimensional. Early transition at random points along the separating surface boundary layer or axial instabilities in the sheet itself may result in deep gouges normal to the axis of the shedding vortex. If these gouges occur where the probe slices through the wake, they may put laminar fluid in its path at a point which corresponds to the average position of a vortex center.

5. The most important conclusion for the mean flow is Figure 5.2. The mean bubble at a Reynolds number of 140,000 is much smaller and more confined than was expected, with mean closure occurring about 1.1 diameters downstream of the cylinder center. The wake defect velocity decays very rapidly and drops below 20 percent of U_∞ at X/D = 6. Both of these properties of the mean flow allude to the dynamical nature of the near wake where the unsteady vortex shedding motions give rise to very large convective stresses.

6. The vortex formation region is seen to extend downstream of the mean separation bubble. Downstream of the formation region, entrainment consists of deep intrusions of laminar (neglecting free stream turbulence) fluid, which may cross the wake axis with a lateral velocity as large as half the free stream speed. In a frame of reference moving with the vortices, there is a

confluence between fluid moving across the wake axis and fluid coming from the other side of the wake in a region of turbulent but essentially non-vortical fluid--the so-called "connective tissue". The confluence region continually feeds entrained fluid into the two adjacent vortices where it participates in the rollup and growth of each vortex. Within the formation region, entrainment occurs as just described except that here the fluid entrained by the forming vortex includes turbulent fluid of opposite vorticity coming from the opposite shear layer. The processes of entrainment and rapid diffusion produce the saddles of "connective tissue" (confluence regions) as each vortex is shed.

7. Perhaps the single most important result regarding momentum transport is that the background turbulence cannot be neglected. Throughout the near wake the mean contributions of large scale motion and background turbulence (including dispersion) are of the same order (Figures 5.21 to 5.23). At X/D = 1.0, the maximum in $\overline{U_1''^2}/U_\infty^2$ (turbulent plus large scale stress) = 0.25; at X/D of 1.5 the maximum in $\overline{U_2''^2}/U_\infty^2 = 0.41$. At X/D of 1.1, $\overline{U_1''U_2''}/U_\infty^2$ has a maximum of 0.14, nearly one order of magnitude larger than the maximum shearing stress in a mixing layer (normalized by the difference velocity between the two streams). All of these quantities drop off rapidly with X/D as may be seen from Figures 5.21 through 5.23.

8. The large scale Reynolds stress, $\tilde{U}_1^2/U_\infty^2$, makes no impression on fluid near the wake centerline; off the centerline, $\tilde{U}_1^2/U_\infty^2$ peaks during the passage of vortex centers and then falls nearly to zero between vortices. The normal stresses (turbulent energy) due to

background turbulence, $\langle U_1'^2 \rangle / U_\infty^2$ and $\langle U_2'^2 \rangle / U_\infty^2$, reach maxima at vortex centers and minima between vortices where each has the character of a slowly changing function which increases across the wake in the direction of the "connective tissue". The most dramatic variation is shown by $\tilde{U}_2^2 / U_\infty^2$, with large maxima between vortices, where large upwash and downwash motions occur, and small minima at vortex centers.

9. The shearing stress at constant phase caused by the large scale motion consists of a set of causally related peaks and valleys. From the point of view of an observer located below the wake centerline, the arrival of a counterclockwise (near) eddy is preceded by a maximum in the large scale shear stress representing a flux of positive x momentum toward the wake centerline. This is followed by a minimum representing a flux of positive x momentum away from the centerline. As the second (far) eddy passes through, smaller amplitude motions again cause a flux of positive x momentum first, toward the centerline, then away. One interesting property of $\tilde{U}_1 \tilde{U}_2 / U_\infty^2$ is that motions of free stream fluid contribute to the shear. The shearing stress at constant phase due to turbulence, $\langle U_1' U_2' \rangle / U_\infty^2$, has the form of an approximately monotonically varying function across the wake, with its high end toward positive Y/D during passage of a counterclockwise eddy and toward negative Y/D during passage of a clockwise eddy.

10. Before any real understanding of the turbulence problem can be reached, further experiments will be necessary which clarify the large eddy structure in a variety of flows. The advent of computer assisted techniques brings with it hope for increased

understanding. Figure 5.29 is a case in point. Any theoretical model of this flow which might try to explain the shape and properties of $\overline{U_1''^2}/U_\infty^2$, but which did not somehow contain within its framework the fact that $\overline{U_1''^2}/U_\infty^2$ is really the net effect of two quite different phenomena, would surely fail when applied to a different flow (or a variation on the wake flow). The cylinder experiment relied heavily on the periodic character of the flow to separate the large eddy from the background turbulence. Unfortunately, few turbulent flows are periodic, and if the large structures inherent to these flows are to be studied in detail, means should be sought to control their appearance.

APPENDIX A

DATA ACQUISITION AND CONTROL

Throughout the cylinder experiment, data management was under automatic control of a computer data acquisition system (Solo System). Data are digitized by a 16 channel Preston A/D converter (ADC) with a resolution of 14 bits plus sign, capable of conversion rates as high as 500,000 words/sec on one channel. The computer is an HP 2100 minicomputer with a disc operating system and 32K of core memory. The basic computer word is 16 bits. Data from the ADC are left-justified in memory, leaving the last bit available as a comment bit. Data are written on magnetic tape in phase encoded format with a density of 1600 bits per inch.

One of the important features of the ADC is that an external clock can be used to cause conversions to take place almost simultaneously on two hot wires. For the cylinder experiment, the source of the external clock signal was a 200 KHZ pulse train coming from a preset counter built into the Solo System. An input to the ADC called BETA can be used to prevent conversions. If BETA is held false, no conversions will occur no matter what is on the clock line. The clock signal is the prime mover in the whole process. When a clock pulse occurs, the multiplexer switches to the next data channel and a 1.5 μsec delay begins which allows for settling of the analog input amplifier and the sample-and-hold amplifier. After 1.5 μsec, an internal pulse (TADC = trigger ADC) puts the sample-

and-hold circuit into "hold". Conversion begins. After a further 1.2 μsec delay, a gate pulse causes digital output to begin. Old data become invalid, and the sample-and-hold circuit returns to "sample". About 0.5 μsec after gate, or 1.7 μsec after TADC, an output pulse called EOC (end of conversion) is provided by the ADC to show that digital data are ready. Each conversion cycle requires 3.2 μsec. The period (5 μsec) of the clock signal determines the time between conversions.

Data acquisition was slaved to the position of the flying arm by using the 256-tooth encoder on the hub of the flying arm together with an external logic circuit (labelled clock controller in Figure A.1) to control the arrival of bursts of clock pulses at the ADC. Refer to Figure A.2. Initially, the $\overline{\text{HOLDOFF}}$ toggle switch is false; the ADC is quiescent; the computer is poised, waiting for the first word of data. The arm is rotating, putting out 256 encoder pulses per revolution. Each time arm I passes through $\phi = -87.65^{\circ}$, a zero pulse occurs. When $\overline{\text{HOLD-OFF}}$ is switched true, the clock controller is armed, and when the next zero pulse arrives, there is a 427 μsec delay after which γ is latched true and BETA becomes true. The next positive edge of the encoder signal occurs when $\phi = -86.31^{\circ}$. Prior to this, α has been fired to load the countdown counter with the binary coded decimal number which has been specified by the toggle switches on the front panel of the controller. This number corresponds to the number of data channels. The positive edge of the encoder causes δ to go up, and 200 kHz pulses generated by the preset counter,

which have first been gated by the encoder signal, begin to come through as the clock pulses. Each time the sample-and-hold circuit goes into "hold", a pulse occurs on the TADC line. These TADC pulses are inverted and fed into the countdown line of the counter. When all outputs of the counter are low, a number of clock pulses equal to the number of data channels have been gated through, and δ falls. Twelve conversions of data, one for each ADC channel beginning with first channel (0), have now occurred. Nothing more happens until the negative-going edge of the encoder signal arrives, at which point the counter is reloaded and the cycle is ready to begin again. As long as BETA is true, bursts of 12 conversions, one per data channel, will continue to occur each time a positive-going edge of the encoder signal is encountered.

Data from the ADC was processed in the computer by one of three available programs. One program was designed to be used with the arm not rotating; one was for calibration and benchmark runs; and the third program was used for making phase related wake measurements. Each of the data acquisition programs was a self-contained, stand-alone program which did not require the system for its operation, and hence could utilize the full core in order to efficiently meet the rather severe data handling requirements of the flying hot wire. The programs were not equipped to perform the two's complement arithmetic necessary to process negative numbers and therefore only functioned properly with positive input voltages to the ADC. Each program used two data buffers of 3K words apiece, two tape buffers with 2304 or 2048

words, and one accumulation buffer, 2176 words long.

It was decided early on that data from the lower half revolution where the arm passes the streamlined strut would be of no use; therefore, all recorded hot wire data are restricted to frame numbers 1-128. Phase related data are restricted still further to a set of frames in the upper half revolution specified by two program parameters, NSAVE and NSKIP.

The programs utilize the asynchronous no-wait feature of DMA transfers in a ping-pong sequence of editing data in one buffer while filling another. The sequence of events comprising a typical run is as follows:

1. Initially the $\overline{\text{HOLDOFF}}$ switch is false, therefore BETA is false and the ADC is disabled. The number of data channels is specified by setting the toggle switches on the clock controller. The front panel switches on the ADC are set to the first (CHAN 0) and last (CHAN 11) channels to be used.

2. A program is loaded into core and the number of revolutions (NREV), number of records (NREC), number of channels (NCHAN), and, in the case of wake data, the number of skipped frames (NSKIP) and the number of saved frames (NSAVE) are entered into their appropriate memory locations using the display register buttons of the computer (NSAVE was always set equal to 78). For proper operation, the controller toggle setting, ADC toggle settings, and NCHAN must agree in the number of data channels.

3. The run button on the computer is pushed, and the initialization stage of the previously loaded program begins. The interrupt system is disabled, and the various buffers and accumulators are cleared. The program makes several diagnostics to check system readiness. The magnetic tape unit writes a gap; the multiplexer on the ADC is initialized to the last channel; and the computer sets up the first DMA transfer. At this point the whole system is in a state of suspended animation, waiting for data to become available from the ADC (see Table 1 for ADC channel assignments).

4. When $\overline{\text{HOLDOFF}}$ is switched to true, the controller is armed and when the next zero pulse arrives, BETA goes true and bursts of clock pulses begin to arrive at the ADC. The first revolution, beginning with frame 1, fills the first data buffer (12 channels x 256 frames/rev = 3K words).

5. The second revolution, beginning with frame 1, begins filling the second data buffer, and while this is filling, the data in the first are edited. The editing routine performs several functions on data contained in the filled data buffer. Hot-wire data from the lower half revolution are discarded. Channels 0-7 are accumulated over each revolution. For wake data, the 256 frames of data on channels 0 and 1 are combined into single words with the first eight bits of each word being the eight most significant bits of channel 0 (Pitran ramp) and the second eight bits being the eight most significant bits of channel 1 (hot wire ramp). The editing routine uses the 2K word accumulator to keep track

of V, V^2, V_{max}, and V_{min} on channels 8, 9, 10, and 11 (hot wire channels) for all 128 frames of the upper half revolution. Input switches to the new data buffer at the beginning of each revolution. Each time input is switched to the new data buffer, the program checks to see if the index pulse has already occurred. If it has, the revolution is considered to be out of synchronization, and the data are discarded. The program also checks to see that the ADC has ended up on the last channel. If it has not, a format error has occurred, and the data are discarded. In either case, the revolution is considered a bad revolution (BADRV), and its serial number (complemented for synchronization errors) is retained. If 124 such bad revolutions occur, the program aborts.

6. As the hot wire data are edited, they are inserted into the current, unfilled tape buffer. In the cylinder experiment, NREV/NREC (number of revolutions per tape record) was always equal to four so that each tape buffer was composed of four revolutions of edited data. For wake measurements, each revolution of data is constructed as follows: the first 78 x 4 words of the revolution are hot wire data; the next 256 words are ramp data; the last eight words are the averages over the revolution of channels 0-7 ((78 x 4 + 256 + 8) x 4 = 2304 words per record). For calibration and benchmark measurements and measurements with the arms not rotating, each revolution of data is composed of 8 words consisting of the averages over the revolution of channels 0-7, followed by 4 x 126 words of hot wire data beginning

with frame 3 ((8 + 4 x 126) x 4 = 2048 words/record). At the end of the edit routine for each revolution, the program checks to see if the current data buffer is full. If the buffer is full, editing has taken too long, and the program aborts. The time needed for editing places an upper limit (~ 5 revolutions/sec) on the speed at which the flying hot wire may run.

7. After four revolutions, the edited data begin filling the second tape buffer, and while this second buffer is filling, the data in the filled buffer are written onto magnetic tape via a second DMA channel.

8. At the end of a run, after NREC such data records have been written, the mean, RMS, and maximum and minimum hot wire voltages stored in the accumulator are written as the last record in the file.

The intermittency signal is hooked into the GAMMA line of the ADC (Figure A. 1) where it is inverted and used by the computer to modify the last bit in each data word. Data which are even imply turbulence. Odd data imply no turbulence.

For the program designed to take data with the flying hot wire arms fixed, the encoder signal was simulated by a function generator, and the synchronization diagnostic routine was omitted.

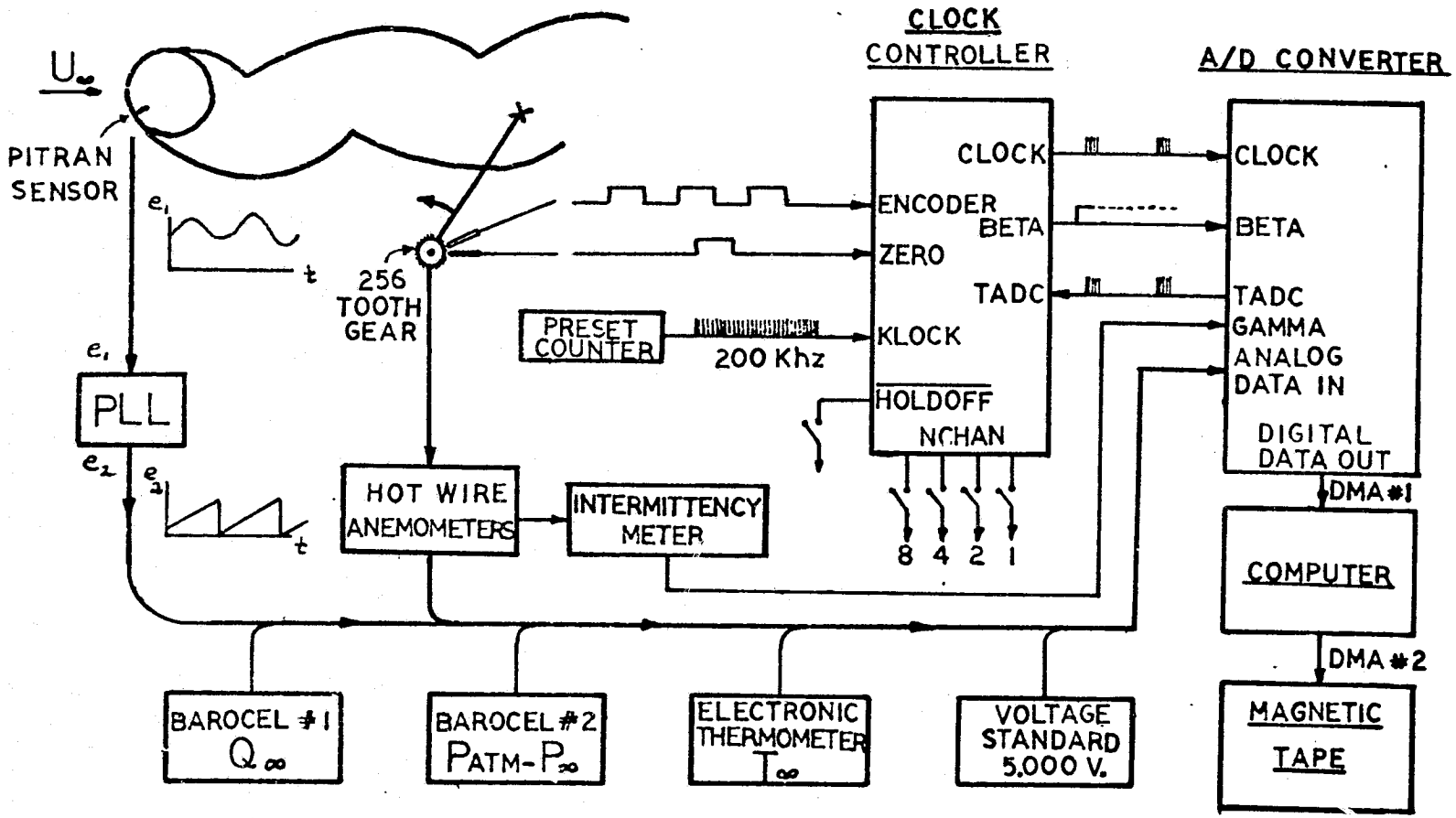

Figure A.1 A sketch showing the causal relationship between various instrumentation and data acquisition modules.

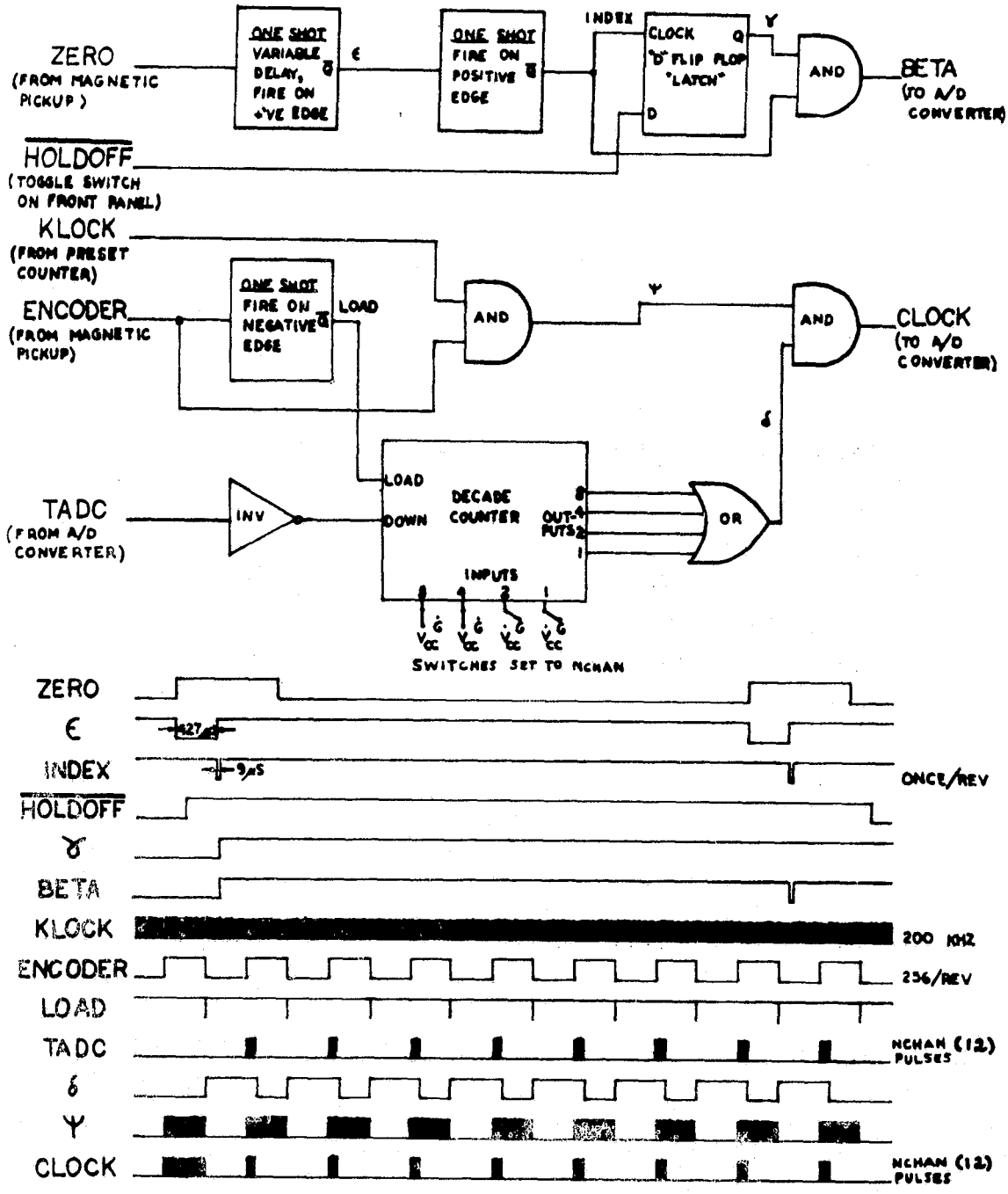

Figure A.2 A logic and timing diagram of the clock controller.

APPENDIX B

THE MEASUREMENT OF FLOW PROPERTIES

Tunnel dynamic pressure (Q_∞) was nominally set by an operator reading a micromanometer which was connected to a pair of pressure rings located in the contraction section of the tunnel. The micromanometer was calibrated to produce the desired value of Q_∞ at the position of the cylinder center with the test section empty. A Pitot-static tube attached to the ceiling of the test section measured tunnel static and dynamic pressures. An electronic thermometer measured tunnel temperature.

Pressures were measured in the cylinder experiment using two Barocel electronic manometers. Model 511 sensors with a range of 0-100 mm Hg were used. The manometers have a full-scale output of 10 volts and are linear to better than 0.5 percent over a wide dynamic range.

Tunnel dynamic pressure was measured using a Pitot-static tube fixed midway along the ceiling of the test section and protruding about twelve inches into the airstream. While this gave accurate reference values for Q_∞ at that particular point in the test section, the dynamic pressure did vary slightly along the arc used for calibrating hot wires. To see this variation, a Pitot-static tube was mounted on one arm and positioned at several points along the calibration arc. Tunnel Q_∞ was then varied by the operator through all the nominal values used during calibrations, and the values of $Q_{\infty\,\mathrm{arm}}$ and $Q_{\infty\,\mathrm{fixed}}$ were compared. Figure B.1 shows how $Q_{\infty\,\mathrm{arm}}/Q_{\infty\,\mathrm{fixed}}$ varied with position (mm) and $Q_{\infty\,\mathrm{nominal}}$

(in psf). A good approximation to the variation of $Q_{\infty arm}/Q_{\infty fixed}$ is given by equation (B.1),

$$\frac{Q_{\infty arm}}{Q_{\infty fixed}} = (-1.54 \cdot 10^{-8})x^2 + (3.179 \cdot 10^{-5})x + 0.986 \qquad (B.1)$$
$$-0.01\, Q_{\infty nom} - (1.43 \cdot 10^{-2})(Q_{\infty nom}^{-1} - 0.05)^{\frac{1}{2}}$$

All calibration and benchmark runs were carried out with the y-traverse set at 36 inches and the x-traverse at 522 mm. Dynamic pressure, Q_∞, at the position of the x-array sensor on the tip of the arm is obtained by multiplying $Q_{\infty fixed}$ (which was recorded with the data) by (B.1) with x taken relative to the traverse origin;

$$x = 522 - R\sin\phi \qquad (B.2)$$

The spatial coordinate, x, is used instead of the arm angle, ϕ, because most of the variation in Q_∞ with arm angle (at fixed $Q_{\infty nominal}$) is due to variations along the axis of the test section. Hence (B.1) will more accurately represent the behavior of Q_∞ at points outside the range of measurement, where ϕ ranges from ±40 degrees to ±90 degrees, but where x varies only slightly.

The measurements in Figure B.1 were made with the tunnel empty. However, for benchmark runs which were done with the cylinder installed, Q_∞ was assumed to behave in the same way. For calibrations obtained from wake data runs, the small correction to $Q_{\infty fixed}$ described by equation (B.1) was not applied. Q_∞, and hence U_∞, was obtained directly from the fixed pitot-static tube. This may introduce an error in U_∞ on the order of 0.5 percent or less.

Throughout the experiment, the atmospheric pressure, P_{atm}, and wet and dry bulb temperatures were recorded at least once a day. Wet and dry bulb temperatures are used to find the vapor pressure of moisture in the air, H, which tended to remain fairly close to 10 mm Hg.

The recorded atmospheric pressure varied much more than expected. This variance was probably the result of faulty barometer readings by an inexperienced technician. These data were discarded, and the atmospheric pressure recorded by the tower at Los Angeles International Airport was used after corrections were made for the altitude difference between LAX and the 10-foot tunnel, assuming an adiabatic atmosphere.

Tunnel static pressure, P_∞, was taken from the static port on the pitot-static tube used to measure Q_∞. P_∞ was always slightly below atmospheric pressure and had to be applied to the low side of a Barocel which was referenced on the high side to P_{atm}. This arrangement was necessary to make the output voltage positive as required by the data acquisition programs.

Tunnel temperature, T_∞, was measured using an electronic thermometer (National model LX5606) mounted on the wall of the test section, close to the centerline, approximately 14 inches forward of the downstream edge. To check the accuracy of the electronic thermometer, and for the sake of redundancy, the temperature was manually recorded from two other thermometers: a permanent vapor pressure thermometer attached to the wall of the test section, and a temporary mercury thermometer inserted into

the air exchange slot at the rear of the test section. The electronic thermometer followed changes in the vapor pressure thermometer very well, but tended to read about one degree too low. A correction was added to the voltage recorded from the electronic thermometer when it was used in the computation of tunnel velocity. However, no correction was applied when the electronic thermometer was used to compute $T_w - T_\infty$ (wire temperature minus air temperature) in the Nusselt number in King's Law, since only changes in this quantity are important.

During wake data runs when Q_∞ was held at 5 psf, T_∞ tended to vary less than one degree. The largest temperature changes, on the order of several degrees centigrade, occurred during calibrations. These variations were caused by the power input to the flow by the fan at increased values of Q_∞. The worst case temperature variations were about 5^oC and represent changes in viscosity of about 1.3 percent and changes in Reynolds number on the order of 3 percent. The circuit of the electronic sensor was designed so that the temperature in ^oC was equal to 10 times the output voltage.

Tunnel speed is computed from the measured flow properties. Using the atmospheric pressure known for each date along with the voltage (averaged over a revolution) recorded on channel 6, the tunnel static pressure is computed from

$$P_\infty = P_{atm} - E_6 \quad \text{(mm Hg)} \qquad \text{(B.3)}$$

Using the temperature correction known for each day along with the voltage from channel 5, the tunnel temperature is computed from

$$T_\infty = T_c + 10 E_5 \qquad (^oC) \tag{B.4}$$

The density is computed from equation (B.5) using P_∞, T_∞ and the vapor pressure (H) of moisture in the air known for each day.

$$\rho_\infty = \frac{(P_\infty - 0.3783 H)}{2153.06(T_\infty + 273.15)} \qquad (gm/cm^3) \tag{B.5}$$

The tunnel dynamic pressure is computed using the voltage recorded from channel 7 (fixed Pitot-static tube) multiplied by 1332.895 to convert from mm Hg to dynes/cm^2. Tunnel velocity is computed from

$$U_\infty = (2 Q_{\infty\,fixed}/\rho_\infty)^{\frac{1}{2}} \qquad (cm/sec). \tag{B.6}$$

To correct $U_{\infty\,fixed}$ for variations in Q_∞ along the calibration arc, U_∞ is multiplied by the square root of equation (B.1).

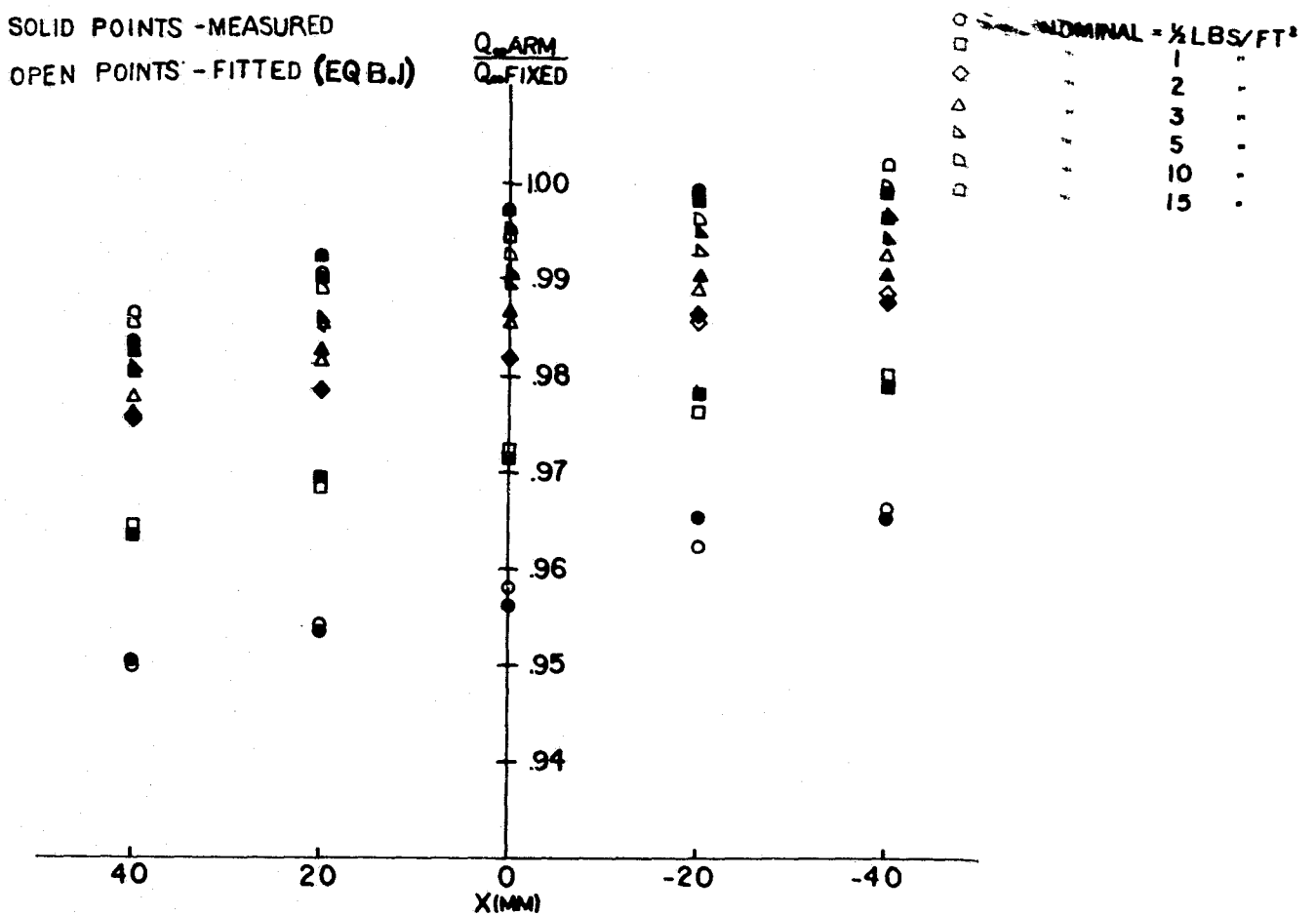

Figure B.1 The variation with x and $Q_{\infty nominal}$ of the ratio of tunnel Q_∞ as measured along the calibration arc to tunnel Q_∞ as measured by the fixed pitot static tube.

APPENDIX C

HOT WIRE CALIBRATION ANALYSIS

Hot wires were assumed to follow King's law in the form of equation (C.1)

$$Nu = A' + B'(Re_{\perp})^{\eta} \tag{C.1}$$

where Nu is the Nusselt number and $Re_{\perp}$ is the Reynolds number based on the component of velocity normal to the wire.

If fluid properties (ρ, μ, k) are based on the wire temperature T_w and a linear dependence on $T_w - T_\infty$ is assumed, equation (C.2) results

$$\frac{E^2}{T_w - T_\infty} = A + B(U_{\perp})^{\eta} \tag{C.2}$$

where E is the anemometer output in volts, T_∞ is the gas temperature in ^{o}C, and $U_{\perp}$ is the velocity component normal to the wire in cm/sec. Since the fluid properties are not part of the picture, the dimensioned quantity $E^2/\Delta T$ will still be termed "Nusselt number" for lack of a better phrase.

Referring to Figure C.1 consider $U_{\perp}$ for two inclined wires.

$$U_{\perp o} = Ux_r \sin\beta_o - Uy_r \cos\beta_o = Ux_r \sin\beta_o (1 - \cot\beta_o \tan\alpha) \tag{C.3}$$

$$U_{\perp 1} = Ux_r \sin\beta_1 + Uy_r \cos\beta_1 = Ux_r \sin\beta_1 (1 + \cot\beta_1 \tan\alpha) \tag{C.4}$$

Substituting equations (C.3) and (C.4) into equation (C.2) and absorbing $(\sin\beta)^{\eta}$ into B one obtains the following:

$$N_o \equiv \frac{E_o^2}{T_{wo} - T_\infty} = A_o + B_o(Ux_r(1 + C_o \tan\alpha))^{\eta_o} \tag{C.5}$$

$$N_1 \equiv \frac{E_1^2}{T_{w1}-T_\infty} = A_1 + B_1(Ux_r(1+C_1\tan\alpha))^{\eta_1} \quad . \qquad (C.6)$$

A, B, η and C are constants around 0.2, 0.01, 0.5 and 1.0, respectively, which are independent of Ux_r and α. Rearrange equations (C.5) and (C.6) to form

$$G_o \equiv \left(\frac{N_o-A_o}{B_o}\right)^{1/\eta_o} = Ux_r(1 + C_o\tan\alpha) \qquad (C.7)$$

and

$$G_1 \equiv \left(\frac{N_1-A_1}{B_1}\right)^{1/\eta_1} = Ux_r(1 + C_1\tan\alpha) \quad . \qquad (C.8)$$

Dimensional Nusselt numbers ($E^2/\Delta T$) corresponding to a set of suitably chosen calibration α's are found using the voltages and T_∞ measured along each calibration arc, equation (2.4), and the known value of K for each calibration setting. A quadratic is used to interpolate N between frames which fall on either side of a chosen value of α.

Equations (B.1), (B.2), (B.3), (B.4), (B.5) and (B.6) are used to compute U_∞ at each ϕ corresponding to the chosen α's. Fluctuations in $Q_{\infty\,\text{fixed}}$, P_∞ and T_∞ over a typical calibration setting ($Q_{\infty\text{nominal}}$, ωR) are small enough so that simple averages of these quantities are used. The flow is assumed to be horizontal and equation (2.5) is used to compute U_r and hence Ux_r at each ϕ (or α). The final result is a set of pairs (N(I, J), Ux_r(I, J)) for each wire corresponding to the Ith calibration setting and Jth calibration angle.

Several approaches to the average of $E^2/(T_w-T_\infty)$ were tried and each result was compared to the exact value found by averaging

$E^2/(T_w-T_\infty)$ over every revolution of a calibration run. The average using $\overline{E}$ and $\overline{E'^2}$ taken from the last record and multiplied by the average of $1/(T_w-T_\infty)$ approximates the exact value up to several parts in the fifth significant figure. The average using $1/(T_w-\overline{T}_\infty)$ gave rise to an error, in N, of about 0.5 percent or smaller, depending on how much T_∞ varied during the run. The exact average was used in calibrations derived from calibration and benchmark runs. Calibrations derived later from wake data runs used the approximate average: $\overline{N} = (\overline{E}^2 + \overline{E'^2})(\overline{1/(T_w-T_\infty)})$.

The first consideration in deciding on a range of α's to use for calibration purposes is to notice that the cross of the x-array is rotated 5.64° in its own plane (Figure 2.4). Twenty-three α's in the three degree increments between -30° and $+36^\circ$ were chosen first, and later this range was reduced to $-24^\circ < \alpha < 36^\circ$ due to the increased error outside of a 60° range of sensitivity of the x-array.

The first step in approximating the calibration data was to pick off points corresponding to $\alpha = 0^\circ$. There is one such point at top dead center of the arc for each calibration setting. Using this data, A, B and η are found for each wire. A least squares method is used to fit the function $N(Ux_r) = A + B(Ux_r)^\eta$ to the $\alpha = 0$ data. Equation (C.9) is minimized where $Ux_r(I, J_o)$ and $N(I, J_o)$ are the relative horizontal velocity component and the dimensional Nusselt number at $\alpha = 0$, $(J = J_o)$, measured during the Ith calibration setting.

$$L = \sum_{I=1}^{NSET} \left(N(Ux_r(I, J_o)) - N(I, J_o) \right)^2 = \sum_{I=1}^{NSET} \left(A + BUx_r(I, J_o)^{\eta} - N(I, J_o) \right)^2 \qquad (C.9)$$

Differentiating (C.9) with respect to A, B and η and setting these derivatives equal to zero (for a minimum in L) yields three independent equations in A, B and η. The first two are used to eliminate A and B in the third thereby yielding a single nonlinear equation in the unknown η which is then solved using Newton's method. L is rather insensitive to η and changes very little for errors in the optimum η on the order of 0.01, as long as A and B are optimal. This held true no matter what calibration technique was tried. However, this method yields very strange values for the exponent, some of which were too small with the corresponding B too large. This strange result for η is due to the fact that at $\alpha = 0$, the minimum Ux_r which could be applied to the wires was about 1000 cm/sec, and as a result all the calibration data lay on the flat upper part of the King's Law curve where very small perturbations in the data can cause wide variations in the optimum η.

Data at $\alpha \neq 0$ (i.e., away from top dead center) are used to find C in equations (C.7) and (C.8) using the known values of A, B, and η. First, fix α_j and least squares fit $G(I, J) = P(J)\, Ux_r(I, J)$ by minimizing equation (C.10).

$$L(J) = \sum_{I=1}^{NSET} \left(P(J)\, Ux_r(I, J) - G(I, J) \right)^2 \qquad (C.10)$$

Differentiate equation (C.10) with respect to P(J) and set this equal to zero. Solve for P(J).

$$P(J) = \sum_{I=1}^{NSET} G(I, J)\, Ux_r(I, J) \Big/ \sum_{I=1}^{NSET} \left(Ux_r(I, J)\right)^2 \qquad (C.11)$$

Proceeding this way for each α_j at three degree increments for $-24^o \leq \alpha_j \leq 36^o$, one obtains a set of P(J); j = 1, 2...NANG (the number of angles, NANG = 23). The P(J) are now used to least squares fit $P(\alpha) = 1 + C\tan\alpha$ in order to determine C.

$$L = \sum_{J=1}^{NANG} \left(P\left(\alpha(J)\right) - P(J)\right)^2 = \sum_{J=1}^{NANG} \left(1 + C\tan\alpha(J) - P(J)\right)^2 \qquad (C.12)$$

Differentiating equation (C.12) and solving for C, one obtains

$$C = \frac{\sum_{J=1}^{NANG} P(J)\tan\left(\alpha(J)\right) - \sum_{J=1}^{NANG} \tan\left(\alpha(J)\right)}{\sum_{J=1}^{NANG} \left(\tan\left(\alpha(J)\right)\right)^2} \,. \qquad (C.13)$$

Once C is known for a given wire the data at $\alpha = 0$ can be extended to lower and higher Ux_r's by choosing several calibration settings in the high and low velocity ranges. Within each setting several supplementary points are chosen which correspond to $\alpha \neq 0$. The question is now asked, "What equivalent value of U_r at $\alpha = 0$, denoted Ux_{req}, would give the same velocity component normal to the wire as that due to the actual U_r at $\alpha \neq 0$?" The trigonometric constuction in Figure C.1 may help clarify this idea.

$$Ux_{req} = Ux_r(1 + \cot\beta\tan\alpha) = Ux_r(1 + C\tan\alpha) \qquad (C.14)$$

Equation (C.14) relates Ux_r at the supplementary $\alpha \neq 0$ points to the equivalent (i.e., same velocity component normal to the wire) Ux_r at $\alpha = 0$. A, B and η can be recalculated using the supplementary points treated as $\alpha = 0$ data to give a much broader range of Ux_r's.

Actually the least squares fit using equation (C.9) was dicarded in favor of a method which minimizes the error, not in N but in $(Ux_r)^{\eta}$. To further increase the accuracy at low velocities, the new method minimized the fractional error in $(Ux_r)^{\eta}$, rather than the absolute error.

Rearrange the summand in equation (C.9) such that

$$U_{\eta}(N(I, J_o)) \equiv (Ux_r(N(I, J_o)))^{\eta} = (N(I, J_o)-A)/B \ . \qquad (C.15)$$

Minimize (C.16) where NTOT = NSET (the number of calibration settings) plus NSUP (the number of supplementary $\alpha \neq 0$ points).

$$L = \sum_{I=1}^{NTOT} \left(\frac{U_{\eta}(N(I, J_o)) - U_{\eta}(I, J_o)}{U_{\eta}(I, J_o)} \right)^2 = \sum_{I=1}^{NTOT} \left(\frac{N(I, J_o)-A}{BU_{\eta}(I, J_o)} - 1 \right)^2 \qquad (C.16)$$

Differentiate (C.16) with respect to A and B.

$$\frac{\partial L}{\partial A} = \sum_{I=1}^{NTOT} 2 \left(\frac{N(I, J_o) - A}{BU_{\eta}(I, J_o)} - 1 \right) \left(\frac{-1}{BU_{\eta}(I, J_o)} \right) = 0 \qquad (C.17)$$

$$\frac{\partial L}{\partial B} = -\sum_{I=1}^{NTOT} 2\left(\frac{N(I, J_o)-A}{BU_\eta(I, J_o)} - 1\right)\left(\frac{N(I, J_o)-A}{B^2U_\eta(I, J_o)}\right) = 0 \qquad (C.18)$$

Pull A and B out of the summations in equations (C.17) and (C.18).

$$B\sum_{I=1}^{NTOT} \frac{1}{U_\eta(I, J_o)} + A\sum_{I=1}^{NTOT} \frac{1}{U_\eta(I, J_o)^2} - \sum_{I=1}^{NTOT} \frac{N(I, J_o)}{U_\eta(I, J_o)^2} = 0 \quad (C.19)$$

$$B\sum_{I=1}^{NTOT} \frac{N(I, J_o)}{U_\eta(I, J_o)} + A\sum_{I=1}^{NTOT} \frac{N(I, J_o)}{U_\eta(I, J_o)^2} - \sum_{I=1}^{NTOT} \frac{N(I, J_o)^2}{U_\eta(I, J_o)^2} = 0 \quad (C.20)$$

The exponent, η, is decreased from a starting value of 0.7 by increments of .01, and A, B and L are calculated using equations (C.16), (C.19) and (C.20) at each step until a minimum in equation C.16 is achieved. The final values of A, B, and η are used to recompute the G(I,J) which are used in equations (C.11) and (C.13) to compute a new value of C. This C is then used to recalculate the supplementary $\alpha = 0$ data, using equation (C.14), which is used in turn to recompute A, B. and η. After four or five iterations C no longer changes, and the process is terminated.

The method just described was used to process the data on tape 30 to find A, B, η and C for wire set 4(L-0, L-1). A and B

were determined for benchmark runs on tapes 12, 14, 16, 18, 20 and 22 using equations (C.19) and (C.20) along with the tape 30 values of η and C. None of tapes 12-22 included enough benchmark runs to calculate new values of η and C. The method was also used to process calibration tapes 31 and 58 as well as the extensive benchmark data on tapes 35 and 57 (see Table 4).

King's law in the form of equations (C.5) and (C.6) approximates the calibration data quite well, with errors in Ux_r on the order of 50 cm/sec and errors in the angle on the order of 1 1/2 degrees. Errors at large angles of attack tend to exceed the error at $\alpha = 0$. However, in many cases large angles of attack show errors which are commensurate with those at $\alpha = 0$.

The functional form of $P(\alpha) = 1 + C\tan\alpha$ agrees well with the measured data. Fitting a higher order function to $P(\alpha)$ such as a cubic in $\tan\alpha$ would improve the agreement and therefore lessen the error at large angles of attack, but would leave the error at $\alpha = 0$ unchanged.

A different approach for improving the accuracy of the calibration which has the advantage that it decreases the error at all angles of attack is used. The set of measured dimensional Nusselt numbers $N_o(Ux_{r_i}, \alpha_j)$ and $N_1(Ux_{r_i}, \alpha_j)$ are used, along with the previously arrived at calibration constants for each wire pair, to calculate velocities, $Ux_{r\,calc}(I, J)$ and $Uy_{r\,calc}(I, J)$. These calculated velocities are subtracted from the measured velocities, $Ux_r(I, J)$ and $Uy_r(I, J)$, to give the error in the King's Law fit at point (I, J). A polynomial

is used to approximate the error and becomes part of a two-step procedure for inverting (N_o, N_1) pairs to obtain velocities.

Solve for $Ux_{r\,calc}$ and $Uy_{r\,calc}$ using equations (C.7) and (C.8) and the relation $\tan\alpha = Uy_r/Ux_r$ to form equations (C.21) and C.22).

$$Ux_{r\,calc}(I, J) = \frac{C_1 G_o(I, J) - C_o G_1(I, J)}{C_1 - C_o} \qquad (C.21)$$

$$Uy_{r\,calc}(I, J) = \frac{G_1(I, J) - G_o(I, J)}{C_1 - C_o} \qquad (C.22)$$

The errors between the calculated and measured velocity components are formed.

$$E_{ux}(I, J) = Ux_{r\,calc}(I, J) - Ux_r(I, J) \qquad (C.23)$$

$$E_{uy}(I, J) = Uy_{r\,calc}(I, J) - Uy_r(I, J) \qquad (C.24)$$

Because of the correspondence between (I, J) and (Ux_r, Uy_r (or Ux_r and α)), E_{ux} and E_{uy} are each functions of $Ux_{r\,calc}$ and $Uy_{r\,calc}$. That is, given values for N_o and N_1, $Ux_{r\,calc}$ and $Uy_{r\,calc}$ can be found using King's law in the form of equations (C.21) and (C.22). This fixes a point on the Ux_r, Uy_r plane at which the King's law fit is known to be in error by the amount E_{ux} in Ux_r and E_{uy} in Uy_r. Subtracting these errors from $Ux_{r\,calc}$ and $Uy_{r\,calc}$, one obtains the corrected values for Ux_r and Uy_r.

One might ask why not bypass King's law altogether and simply use a high order polynomial to approximate the calibration data. The main disadvantage of this approach is that a large number of coefficients would be involved. Also, E_{ux} and E_{uy} are each functions of Ux_r and Uy_r, not of N_o and N_1, which removes the nuisance of having to solve a nonlinear system.

A polynomial fit to E_{ux} (Ux_r, Uy_r) and E_{uy} (Ux_r, Uy_r) of order 1 (four coefficients) reduces the inaccuracy in approximating the data to errors in Ux_r on the order of 20-30 cm/sec and to errors in the angle of less than 1 degree. A polynomial of order 3 (16 coefficients) halves this error. Going to still higher order polynomials can make the error arbitrarily small. However, this does not make much sense since tapes 30, 31, 35, 58 and 59 are the only ones which contain enough calibration data to produce an error polynomial, and small changes in the calibration due to wire drift would essentially wipe out the efficacy of higher order terms. The coefficients of the first order polynomials found from calibrations of wire set 5 on tapes 31, 35, 58 and 59 and listed on Table 5 are fairly repeatable in spite of the fact that the wire calibrations drifted considerably. Therefore, when restricted to a first order polynomial, this method of improving the accuracy of the calibration would seem to have merit.

The last records of each file on each wake data tape were averaged together, and the inversion procedure described in the previous section was applied to produce the mean flow. Mean and

RMS voltages were sufficient to produce a good approximation to $\overline{U}_1$ and $\overline{U}_2$.

Substitute the definitions of G and N from equations (C.5), (C.6), (C.7) and (C.8) into equations (C.21) and (C.22). Define $T \equiv T_w - T_\infty$.

$$Ux_r = \left(\frac{C_1}{C_1-C_o}\right)\left(\frac{1}{B_o}\right)^{\frac{1}{\eta_o}}\left[\overline{\left(\frac{1}{T_{wo}-T_\infty}\right)^{\frac{1}{\eta_o}}}\right]\left(E_o^2 - T_oA_o\right)^{\frac{1}{\eta_o}} - \left(\frac{C_o}{C_1-C_o}\right)\left(\frac{1}{B_1}\right)^{\frac{1}{\eta_1}}\left[\overline{\left(\frac{1}{T_{w1}-T_\infty}\right)^{\frac{1}{\eta_1}}}\right]\left(E_1^2-T_1A_1\right)^{\frac{1}{\eta_1}} \quad (C.25)$$

$$Uy_r = \left(\frac{1}{C_1-C_o}\right)\left(\frac{1}{B_1}\right)^{\frac{1}{\eta_1}}\left[\overline{\left(\frac{1}{T_{w1}-T_\infty}\right)^{\frac{1}{\eta_1}}}\right]\left(E_1^2-T_1A_1\right)^{\frac{1}{\eta_1}} - \left(\frac{1}{C_1-C_o}\right)\left(\frac{1}{B_o}\right)^{\frac{1}{\eta_o}}\left[\overline{\left(\frac{1}{T_{wo}-T_\infty}\right)^{\frac{1}{\eta_o}}}\right]\left(E_o^2-T_oA_o\right)^{\frac{1}{\eta_o}} \quad (C.26)$$

Let $P \equiv (E^2 - TA)^{1/\eta}$

$$P + P' = \left(\left(\overline{E} + E'\right)^2 - TA\right)^{2}\Big)^{1/2\eta} \quad (C.27)$$

Assume that

$$\overline{P} = \left[\overline{\left(\left(\overline{E} + E'\right)^2 - TA\right)^2}\right]^{1/2\eta} = \overline{s}^{1/2\eta}. \quad (C.28)$$

This is exact if $\eta = 0.5$. Expand $\overline{s}$ to get

$$\overline{s} = \overline{E}^4\left(1 + 6\,\frac{\overline{E'^2}}{\overline{E}^2} + \frac{\overline{E'^4}}{\overline{E}^4} - \frac{2TA}{\overline{E}^2}\left(1 + \frac{\overline{E'^2}}{\overline{E}^2}\right) + \frac{T^2A^2}{\overline{E}^4}\right). \quad (C.29)$$

The only unknown in equation (C.29) is $\overline{E'^4}$, which is small and can be neglected.

The mean and RMS voltages are used in equations (C.25) through C.29) to compute $Ux_{r\,calc}$ and $Uy_{r\,calc}$ which are then corrected as described earlier.

First efforts at applying the calibrations to the mean flow data concentrated on wire set 5 arm II (L-2, L-3). The flow field was plotted in full scale on wide paper using arrows whose length was normalized by the free stream speed. Points were compared where redundant measurements were taken to check for agreement.

The calibration derived from tape 31 was applied to wake data on tapes 31-57. The flow field according to tapes 31-35 looked right, but tapes 36-57 did not agree very well with each other or with tapes 31-35. Next the calibration derived from tape 58 was applied to tapes 31-57; still there was disagreement, and it was apparent that the wire calibrations had drifted between tapes. An interpolation via straight lines was tried. This interpolation gave good agreement between tapes 31-35 and 48-57. Tapes 36-47 still indicated an odd flow angle and the wrong magnitude (too small). Other efforts were made; all to no avail!

A calibration process was finally adopted which relies on the self-calibrating feature of the flying hot wire and the fact that nearly all of the arcs used for wake measurement include substantial portions where the wires were outside the disturbance region of the wake. The result of this process was a unique set of calibration constants, A, B, η and C, for each wake data tape. These constants are

listed in Table 6.

Frames where the flow was approximately uniform were chosen along each data arc (Table 7). The same technique which was used to extend the $\alpha = 0$ data in the hot wire calibrations was used to produce a King's law curve (at $\alpha = 0$) for each wake data tape.

Because the effective wire angle drifted very little during the calibrations and because the results are relatively insensitive to errors in the optimum exponent, η and C were determined for each wake data tape by interpolating between calibrations via straight lines as described previously.

Each tape was processed in the following way. The known values of K and U_∞ were used to determine α and Ux_r at each of the chosen uniform flow frames. Figure C.1 and equation (C.14) are then used with the known value of C to calculate the value of Ux_{req} that would have to pertain at $\alpha = 0$ in order to give the same velocity component normal to the wire as that given by the actual relative velocity vector. These Ux_r's are exponentiated, using the known value of η and used, along with the values of N chosen along the arc, in equations (C.19) and (C.20) to determine the A and B appropriate to the tape in question. The most accurately known wake results are those for tapes 31 and 57, where wake data were taken immediately after or immediately before an extensive wire calibration. Based on the results for these trajectories, one can get a pretty good idea how valid the assumption of the flow uniformity outside the wake really is! Judging from the

results on these two tapes, points more than 10 diamteres or so downstream of the cylinder and more than $1\frac{1}{2}$ diameters away from the centerline of the wake are in an area where the velocity is equal to U_∞ but diverging at an angle of 2^o. At 6 diameters downstream, the divergence is about 1^o and the velocity is about 3 percent above U_∞. Forward of the cylinder in regions chosen for calibration the divergence is again about 1^o, with the velocity about 3 percent above the free stream speed. These nonuniformities were incorporated into the calibration of each wake data tape. Table 7 lists the uniform flow frame numbers used in the calibration of each tape.

Generally the calibrations listed in Table 6 give good results. Points where different trajectories cross give nearly the same velocity vector in most cases. The two independent x-arrays of wire set 5 yield results for the mean flow which are practically indistinguishable. The only tapes still showing major disagreement are tapes 24 through 28. These trajectories lie almost entirely inside the wake, and therefore the only frames which are outside the region of turbulent flow . re at the extremeties of the arcs where the relative flow angle is severe.

The calculation of velocities is a five step procedure.

STEP 1 Form Nusselt numbers from the measured hot wire voltages and T_∞.

STEP 2 Use equations (C.7), (C.8), (C.21) and (C.22) along with the known values of A, B, C and η (Table 6) for the given wire pair, to compute $Ux_{r\,calc}$ and $Uy_{r\,calc}$.

STEP 3 Substitute $Ux_{r\,calc}$ and $Uy_{r\,calc}$ into equations (C.30) and (C.31) to find E_{ux} and E_{uy}.

$$E_{ux} = COFX(1) + COFX(2) \times 10^{-3}(Uy_{r\,calc}) + COFX(3) \times 10^{-3}(Ux_{r\,calc}) + COFX(4) \times 10^{-6}(Ux_{r\,calc} \cdot Uy_{r\,calc}) \quad (C.30)$$

$$E_{uy} = COFY(1) + COFY(2) \times 10^{-3}(Uy_{r\,calc}) + COFY(3) \times 10^{-3}(Ux_{r\,calc}) + COFY(4) \times 10^{-6}(Ux_{r\,calc} \cdot Uy_{r\,calc}) \quad (C.31)$$

where COFX and COFY are taken from Table 5.

STEP 4 Use E_{ux} and E_{uy} to find the corrected velocity components relative to the flying hot wire.

$$Ux_r = Ux_{r\,calc} - E_{ux} \quad (C.32)$$

$$Uy_r = Uy_{r\,calc} - E_{uy} \quad (C.33)$$

STEP 5 Transform Ux_r, Uy_r from flying coordinates to fixed coordinates (U_1, U_2) using the known arm angle ϕ, tip speed $R\omega$ and equations (2.6) and (2.7).

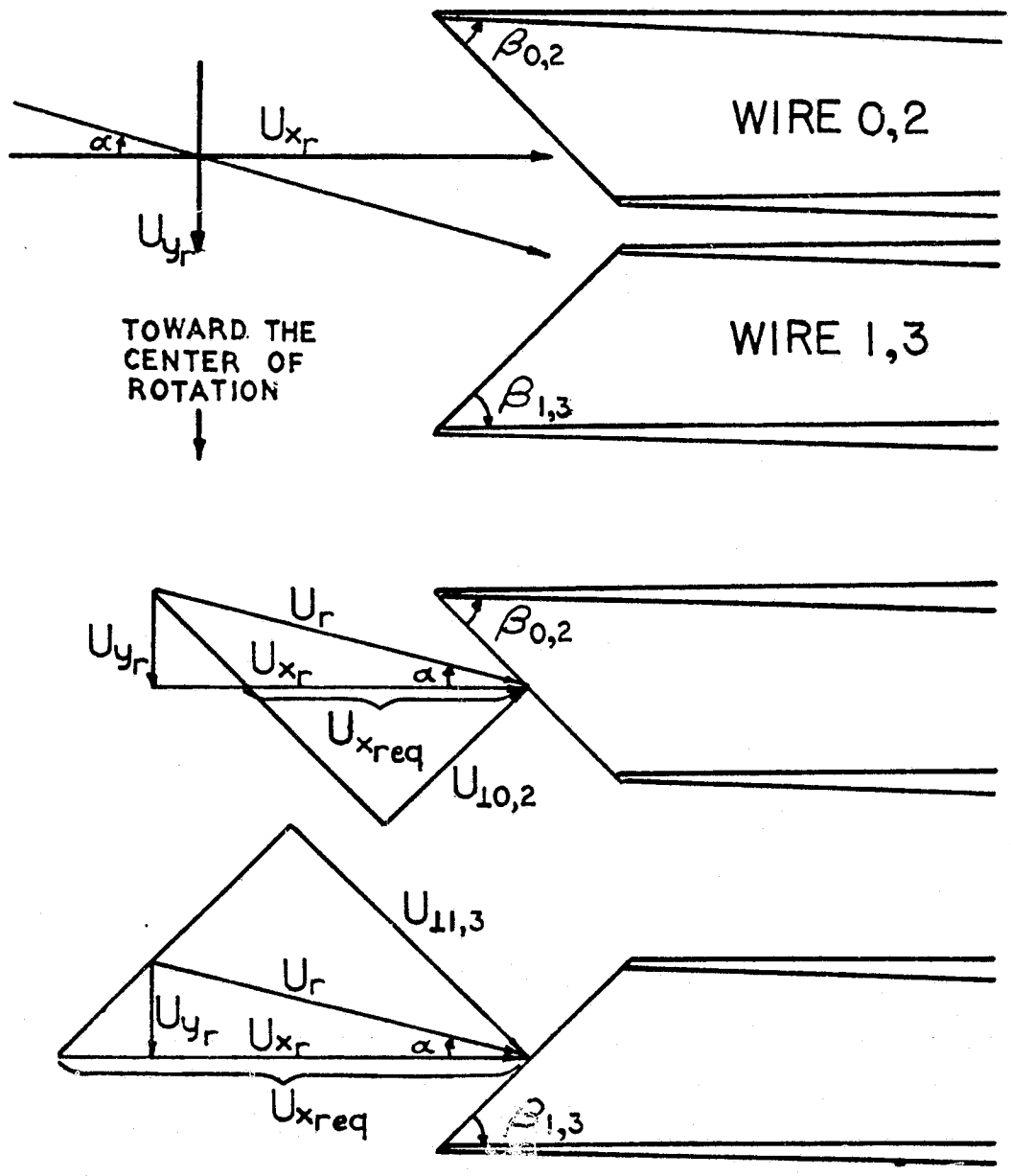

Figure C.1 A sketch showing the choice of coordinates for two inclined wires, including the construction used to supplement data taken at $\alpha = 0$ with data taken at points along the arc where $\alpha \neq 0$.

TABLE 1

NOMINAL ADC CHANNEL ASSIGNMENTS

ADC CHANNEL	INPUT
0(L-11)	Phase Ramp (PITRAN)
1(L-10)	Phase Ramp (Inclined Hot Wire)
2(L-9)	Short
3(L-8)	Short
4(L-7)	+ (-) 5 v. (ANALOGIC)
5(L-6)	Electronic Thermometer (T_∞)
6(L-5)	BAROCEL P_{atm} - P_∞
7(L-4)	BAROCEL Q_∞
8(L-3)	Hot Wire L-3
9(L-2)	Hot Wire L-2
10(L-1)	Hot Wire L-1
11(L-ϕ)	Hot Wire L-ϕ

TABLE 2

PROBES USED FOR MEASUREMENT, HOT AND COLD RESISTANCES, TEMPERATURES

Probe ID# = ADC CHANNEL (L-?) / ANEM CHANNEL / ARM CHANNEL - PROBE # - WIRE #

$$R_w = R_{ref}\,(1 + \sigma(T_w - T_{ref}));\ \sigma = 0.0036^{o}C^{-1}$$

Wire Set-Calibration	Probe ID	T_{ref}, °C	R_{ref}, Ω	R_w, Ω	Cable Resistance, Ω	T_w, °C	Applicable Tape #	Comment
4-1								
Arm 1	0-3-A	25	3.65	5.33	3.17	152.9	12-30	
	1-3-B	25	3.88	5.62	3.18	149.6	12-30	Broken tape 30, File 18
	2-1-A	25	3.50	5.11	3.19	152.8	12	Broken tape
Arm 2	3-1-B	25	3.60	5.31	3.79	156.9	12	11, File 9
5-1								
Arm 1	0-3-A	25	3.80	5.53	3.17	151.5	31-59	
	1-3-B	25	4.20	6.12	3.18	152.0	31-59	
	2-1-A	25	3.90	5.71	3.19	153.9	31-59	
Arm 2	3-1-B	25	4.00	5.81	3.79	150.7	31-59	
5-2								
Arm 1	0-3-A	25	3.80	5.53	3.17	151.5	31-59	
	1-3-B	25	4.20	6.12	3.18	152.0	31-59	
	2-1-A	25	3.90	5.71	3.19	153.9	31-59	
Arm 2	3-1-B	25	4.00	5.81	3.79	150.7	31-59	

TABLE 3

INDEX OF DATA TAPES

Tape #	Files	Date	Time	Data Type	NSKIP	Traverse Settings X, mm	Traverse Settings Y, inches
12	1-3	22 Oct.	17:05	Benchmark	--	522	36.000
12	4-9	"	18:00	Wake Data	50	"	29.000
13	1-6	"	19:50	"	"	"	28.000
14	1-6	"	22:03	"	45	"	27.000
14	7-8	"	23:35	Benchmark	--	"	36.000
15	1-6	23 Oct.	0:32	Wake Data	40	"	26.000
16	1-6	"	2:20	"	"	"	25.000
16	7-8	"	4:28	Benchmark	--	"	36.000
17	1-6	"	5:37	Wake Data	35	"	24.000
18	1-6	"	7:16	"	"	"	23.000
18	7-9	"	9:16	Benchmark	--	"	36.000
19	1-6	"	10:06	Wake Data	35	"	22.000
20	1-6	"	12:15	"	"	"	21.000
20	7-8	"	13:50	Benchmark	--	"	36.000
21	1-6	"	14:30	Wake Data	35	"	20.000
22	1-6	"	16:18	"	"	"	19.000
22	7-11	"	17:50	Benchmark	--	"	36.000
23	1-6	"	18:25	Wake Data	35	"	18.000
24	1-6	"	20:17	"	"	"	17.000
25	1-6	24 Oct.	7:50	"	30	"	16.000
26	1-6	"	10:45	"	"	"	15.000
27	1-6	"	12:28	"	"	"	14.000
28	1-6	"	14:15	"	"	"	13.000
29	1-6	"	16:00	"	"	"	12.000
30	1-18	"	17:38	Benchmark	--	"	36.000
31	1-14	25 Oct.	14:30	Calibration (Wire Set 5)	--	"	36.000

TABLE 3 (Cont'd)

Tape #	Files	Date	Time	Data Type	NSKIP	Traverse Settings X, mm	Traverse Settings Y, inches
31	15	25 Oct.	16:00	Benchmark	--	522	36.000
31	16-18	"	17:00	Wake Data	25	"	12.000
32	1-6	"	18:13	"	"	"	11.000
33	1-4	"	19:43	"	"	"	10.000
34	1-4	"	20:57	"	"	"	9.000
35	1-4	"	22:25	"	"	"	8.000
35	5-16	26 Oct.	0:03	Benchmark	--	"	36.000
36	1-4	"	7:45	Wake Data	50	400	24.000
37	1-4	"	8:53	"	"	"	23.000
38	1-4	"	10:02	"	"	"	22.000
39	1-4	"	11:12	"	"	"	21.000
40	1-4	"	12:.	"	"	"	20.000
41	1-4	"	13:4	"	40	"	19.000
42	1-4	"	15:15	"	"	"	18.000
43	1-4	"	16:34	"	"	"	17.000
44	1-4	"	19:00	"	25	100	13.000
45	1-4	"	20:15	"	"	"	12.000
46	1-4	"	21:26	"	"	"	11.000
47	1-4	"	22:12	"	"	"	10.000
48	1	28 Oct.	7:55	"	"	"	"
48	2-5	"	8:22	"	"	"	9.000
49	1-4	"	10:10	"	"	"	8.000
50	1-4	"	11:19	"	"	"	7.000
51	1-4	"	12:28	"	"	"	7.500
52	1-4	"	13:40	"	"	"	8.500
53	1-4	"	14:55	"	"	"	9.500
54	1-4	"	16:10	"	"	"	10.500
55	1-5	"	17:23	"	"	"	11.500
56	1-4	"	18:55	"	"	"	12.500
57	1-4	"	20:22	"	"	"	13.204
58	1-7	"	21:58	Benchmark	--	522	36.000
59	1-22	29 Oct.	8:47	Calibration Wire Set 5	--	"	"

TABLE 4

CALIBRATION CONSTANTS BASED ON CALIBRATION AND BENCHMARK DATA

Wire	Tape #	A	B	η	C
4-0	12	.0403	.03308	.31	-.8020
4-1		.1746	.00794	.43	1.2313
4-0	14	.0543	.03208	.31	-.8020
4-1		.1814	.00789	.43	1.2313
4-0	16	.0524	.03167	.31	-.8020
4-1		.1827	.00769	.43	1.2313
4-0	18	.0649	.03102	.31	-.8020
4-1		.1895	.00762	.43	1.2313
4-0	20	.0733	.03019	.31	-.8020
4-1		.1867	.00772	.43	1.2313
4-0	22	.0941	.02853	.31	-.8020
4-1		.1677	.00826	.43	1.2313
4-0	30	.1074	.02660	.31	-.8020
4-1		.1727	.00793	.43	1.2313
5-0	31	.1438	.01650	.38	-.8185
5-1		.1881	.00289	.53	1.3204
5-2		.1613	.00592	.47	-.8839
5-3		.1935	.00343	.52	1.2917
5-0	35	.1423	.01797	.37	-.8224
5-1		.1893	.00274	.54	1.2860
5-2		.1666	.00548	.48	-.8770
5-3		.1941	.00384	.51	1.2982
5-0	58	.0977	.03687	.29	-.8127
5-1		.1780	.00553	.46	1.2771
5-2		.1483	.01093	.40	-.8703
5-3		.1819	.00699	.44	1.2834
5-0	59	.1583	.01657	.37	-.8174
5-1		.1661	.00683	.44	1.2727
5-2		.1365	.01354	.38	-.8790
5-3		.1709	.00793	.43	1.2673

TABLE 5

CORRECTION POLYNOMIAL COEFFICIENTS

		X-array pair on Arm I		X-array pair on Arm II	
Tape #	I	COFX1(I)	COFY1(I)	COFX2(I)	COFY2(I)
30	1	50.72	-39.70	—	—
(apply to	2	-8.01	99.70	—	—
Tapes	3	-15.60	17.08	—	—
12-30)	4	.66	-36.72	—	—
31	1	44.49	-6.56	82.40	-30.97
(apply to	2	25.76	84.52	-3.60	102.06
Tapes	3	-6.77	5.75	-18.85	11.97
31-34)	4	-10.48	-25.73	-2.35	-30.06
35	1	50.92	-15.45	82.47	-40.61
(apply to	2	27.33	101.69	-15.70	118.73
Tapes	3	-10.27	7.34	-19.72	14.90
35-43)	4	-12.65	-34.12	.759	-38.96
58	1	55.59	-20.51	91.04	-67.67
(apply to	2	26.11	109.29	-34.03	125.83
Tapes	3	-12.07	6.95	-20.16	19.40
44-58)	4	-10.96	-33.81	6.46	-37.56
59	1	23.06	1.72	52.70	-17.17
	2	55.47	61.87	9.75	90.62
	3	-7.42	5.15	-16.85	9.80
	4	-16.57	-19.30	-3.96	-26.69

TABLE 6

CALIBRATION CONSTANTS BASED ON WAKE DATA TAPES

Tape #	Wire #	A	B	η	C
12	4-0	.03710	.033329	.31	-.8020
	4-1	.15764	.008435	.43	1.2313
13	4-0	.04357	.032824	.31	-.8020
	4-1	.16081	.008367	.43	1.2313
14	4-0	.05100	.032288	.31	-.8020
	4-1	.16479	.008304	.43	1.2313
15	4-0	.06352	.031146	.31	-.8020
	4-1	.16863	.008204	.43	1.2313
16	4-0	.07074	.030523	.31	-.8020
	4-1	.16931	.008168	.43	1.2313
17	4-0	.07154	.030108	.31	-.8020
	4-1	.16892	.008042	.43	1.2313
18	4-0	.05764	.031330	.31	-.8020
	4-1	.18445	.007791	.43	1.2313
19	4-0	.08010	.029591	.31	-.8020
	4-1	.17952	.007941	.43	1.2313
20	4-0	.09396	.028440	.31	-.8020
	4-1	.17874	.007981	.43	1.2313
21	4-0	.11133	.027052	.31	-.8020
	4-1	.17636	.008036	.43	1.2313
22	4-0	.12975	.025356	.31	-.8020
	4-1	.17839	.007954	.43	1.2313

TABLE 6 (Cont'd)

Tape #	Wire #	A	B	η	C
23	4-0	.14544	.024121	.31	-.8020
	4-1	.18035	.007885	.43	1.2313
24	4-0	.11168	.026455	.31	-.8020
	4-1	.18802	.007723	.43	1.2313
25	4-0	.11106	.026264	.31	-.8020
	4-1	.19041	.007549	.43	1.2313
26	4-0	.11234	.025986	.31	-.8020
	4-1	.18948	.007488	.43	1.2313
27	4-0	.11250	.025884	.31	-.8020
	4-1	.19016	.007418	.43	1.2313
28	4-0	.11072	.025914	.31	-.8020
	4-1	.19277	.007312	.43	1.2313
29	4-0	.11560	.025420	.31	-.8020
	4-1	.18431	.007490	.43	1.2313
31	5-0	.13744	.016540	.38	-.8185
	5-1	.20111	.002734	.53	1.3204
	5-2	.15747	.005900	.47	-.8839
	5-3	.20600	.003275	.52	1.2917
32	5-0	.13286	.017247	.377	-.8196
	5-1	.20131	.002686	.533	1.3100
	5-2	.15730	.005817	.473	-.8836
	5-3	.20423	.003436	.516	1.2903
33	5-0	.12987	.017607	.376	-.8199
	5-1	.20076	.002695	.534	1.3070
	5-2	.15613	.005856	.474	-.8835
	5-3	.20323	.003507	.515	1.2900

TABLE 6 (Cont'd)

Tape #	Wire #	A	B	η	C
34	5-0	.12654	.017901	.375	-.8204
	5-1	.20047	.002658	.536	1.2990
	5-2	.15427	.005863	.475	-.8835
	5-3	.20350	.003536	.514	1.2898
35	5-0	.12321	.018865	.370	-.8223
	5-1	.20076	.002581	.540	1.2860
	5-2	.15722	.005606	.480	-.8833
	5-3	.20341	.003682	.510	1.2895
36	5-0	.12670	.019668	.362	-.8214
	5-1	.20816	.002760	.532	1.2850
	5-2	.16419	.005839	.472	-.8828
	5-3	.21073	.003854	.503	1.2860
37	5-0	.13076	.019566	.361	-.8213
	5-1	.20911	.002774	.531	1.2850
	5-2	.16586	.005845	.471	-.8828
	5-3	.21123	.003880	.502	1.2859
38	5-0	.13178	.019575	.360	-.8212
	5-1	.20724	.002813	.530	1.2850
	5-2	.16545	.005872	.470	-.8827
	5-3	.20804	.003953	.501	1.2856
39	5-0	.13996	.019216	.359	-.8208
	5-1	.20361	.002899	.528	1.2845
	5-2	.17068	.005828	.468	-.8826
	5-3	.20364	.004079	.499	1.2850

TABLE 6 (Cont'd)

Tape #	Wire #	A	B	η	C
40	5-0	.14751	.019046	.357	-.8206
	5-1	.19717	.003017	.526	1.2840
	5-2	.17581	.005794	.466	-.8825
	5-3	.19403	.004248	.498	1.2847
41	5-0	.15577	.018830	.355	-.8203
	5-1	.19585	.003057	.525	1.2840
	5-2	.18237	.005670	.465	-.8825
	5-3	.19669	.004248	.497	1.2842
42	5-0	.16546	.018515	.353	-.8202
	5-1	.19619	.003101	.523	1.2840
	5-2	.18893	.005574	.463	-.8823
	5-3	.19609	.004317	.495	1.2839
43	5-0	.18415	.017556	.352	-.8199
	5-1	.18905	.003223	.522	1.2835
	5-2	.20052	.005341	.462	-.8822
	5-3	.18820	.004484	.494	1.2836
44	5-0	.16203	.019537	.349	-.8197
	5-1	.21278	.002965	.519	1.2830
	5-2	.18919	.005848	.459	-.8822
	5-3	.21015	.004160	.492	1.2829
45	5-0	.15845	.019900	.348	-.8195
	5-1	.20971	.003025	.518	1.2830
	5-2	.18702	.005960	.458	-.8821
	5-3	.20905	.004211	.491	1.2824

TABLE 6 (Cont'd)

Tape #	Wire #	A	B	η	C
46	5-0	.15438	.02052	.346	-.8193
	5-1	.20624	.003129	.516	1.2830
	5-2	.18437	.006134	.456	-.8820
	5-3	.20564	.004350	.489	1.2820
47	5-0	.15292	.020799	.345	-.8192
	5-1	.20530	.003171	.515	1.2830
	5-2	.18373	.006231	.455	-.8820
	5-3	.20459	.004416	.488	1.2817
48	5-0	.10871	.031499	.308	-.8148
	5-1	.18620	.004648	.477	1.2790
	5-2	.16010	.009171	.417	-.8803
	5-3	.18253	.006226	.455	1.2720
49	5-0	.10187	.032805	.305	-.8145
	5-1	.18272	.004778	.475	1.2790
	5-2	.15705	.009414	.415	-.8802
	5-3	.17969	.006377	.453	1.2713
50	5-0	.09608	.033797	.303	-.8143
	5-1	.18221	.004863	.473	1.2785
	5-2	.15196	.009771	.413	-.8801
	5-3	.17958	.006479	.451	1.2706
51	5-0	.09742	.033851	.302	-.8141
	5-1	.18102	.004952	.471	1.2780
	5-2	.15185	.009903	.411	-.8800
	5-3	.17890	.006526	.450	1.2702

TABLE 6 (Cont'd)

Tape #	Wire #	A	B	η	C
52	5-0	.09825	.034285	.300	-.8140
	5-1	.18152	.004985	.470	1.2780
	5-2	.15295	.009935	.410	-.8800
	5-3	.17851	.006597	.449	1.2700
53	5-0	.10158	.034196	.299	-.8138
	5-1	.18428	.004990	.469	1.2780
	5-2	.15443	.010044	.408	-.8799
	5-3	.18129	.006603	.448	1.2697
54	5-0	.10540	.033990	.298	-.8137
	5-1	.18571	.004995	.468	1.2780
	5-2	.15478	.010086	.407	-.8798
	5-3	.18266	.006605	.447	1.2692
55	5-0	.10926	.034132	.296	-.8135
	5-1	.18766	.005061	.466	1.2780
	5-2	.15850	.010017	.406	-.8797
	5-3	.18760	.006527	.446	1.2687
56	5-0	.11465	.033816	.295	-.8133
	5-1	.19104	.005080	.464	1.2779
	5-2	.16227	.010001	.404	-.8797
	5-3	.19025	.006565	.444	1.2682
57	5-0	.11759	.033677	.294	-.8134
	5-1	.19056	.005109	.463	1.2778
	5-2	.16446	.009962	.403	-.87960
	5-3	.18803	.006634	.443	1.2680

TABLE 7

UNIFORM FLOW FRAMES

Wire Set 4

Tape #	Frame #'s
12	34-60, 61-86
13	34-60, 61-84
14	34-60, 61-82
15	34-60, 61-80
16	36-60, 61-78
17	38-60, 61-76
18	40-60, 61-74
19	42-60, 61-72
20	44-60, 61-71
21	46-60, 61-69
22	48-60, 61-67
23	50-60, 61-65
24	25-30, 105-110
25	25-30, 104-110
26	25-32, 103-110
27	25-35, 102-110
28	25-35, 101-110
29	32-38, 100-106

Wire Set 5

Tape #	Frame #'s
31	32-38, 100-106
32	32-39, 99-106
33	32-40, 94-102
34	32-41, 92-101
35	32-42, 95-105
36	50-80, 110-114
37	50-76, 110-112
38	50-72, 108-110
39	50-68, 106-110
40	55-61, 104-110
41	50-58, 102-110
42	45-56, 100-110
43	45-52, 98-105
44	30-35, 95-110
45	31-37, 94-108
46	32-39, 93-106
47	33-41, 92-105
48	34-43, 91-104
49	35-45, 90-103
50	35-45, 90-102
51	35-45, 90-103
52	34-43, 91-104
53	33-41, 92-105
54	32-39, 93-106
55	31-37, 94-108
56	30-35, 95-110
57	30-35, 95-110

TABLE 8

REFERENCE LIST OF EXPERIMENTAL PARAMETERS

1. Cylinder diameter, (D), = 10.137 cm
2. Nominal arm radius, (R), = 75.67 cm
3. Dynamic pressure for wake data runs, (Q_∞), = 1.955 mmHg (5 lbs/ft^2)
4. Free stream speed, (U_∞), = 2120 $\pm$ 10 cm/sec
5. Arm tip speed for wake data runs, (ωR), = 2159.56 cm/sec
6. Free stream temperature, (T_∞), = 24 $\pm$ 2 °C
7. Kinematic viscosity, (ν), = 0.1535 cm^2/sec
8. Reynolds number, ($Re = U_\infty D/\nu$), = 140,000
9. Free stream turbulence level, ($\sqrt{u_1''^2}/U_\infty$), $\leq$ 0.006
10. Drag coefficient, (C_D), = 1.227
11. Base pressure coefficient (180°), (Cpb), = -1.21
12. Shedding period = 26.65 msec.
13. Strouhal number = 0.179

REFERENCES

1. Batchelor, G. K., Introduction to Fluid Mechanics, Cambridge University Press, London, (1970).

2. Brown, G. L. and Roshko, A., On Density Effects and Large Structure in Turbulent Mixing Layers, Journal of Fluid Mechanics, 64, (1974).

3. Bloor, M. S., The Transition to Turbulence in the Wake of a Circular Cylinder, Journal of Fluid Mechanics, 19, pp. 300-303, (1964).

4. Castro, I. P., Wake Characteristics of Two Dimensional Perforated Plates Normal to an Air Stream, Journal of Fluid Mechanics, 76, pp. 605-608, (1971).

5. Gerrard, J. H., The Mechanics of the Formation Region of Vortices Behind Bluff Bodies, Journal of Fluid Mechanics, 25, pp. 405-408, (1966).

6. Gerrard, J. H., Numerical Computation of the Magnitude and Frequency of the Lift on a Circular Cylinder, Phil. Trans. of the Royal Society of London, pp. 154-157, (1967).

7. Goldstein, S. H., Modern Developments in Fluid Dynamics Vol. II, Clarendon Press, Oxford, pp. 555-556, (1950).

8. Perry, A. E. and Morrison, G. L., A Study of the Constant Temperature Hot Wire Anemometer, Journal of Fluid Mechanics, 47, (1971).

9. Prandtl, L. and Tietjens, O. G., Applied Hydro- and Aeromechanics, Dover Publications Inc., New York, p. 302, (1957).

REFERENCES (Cont'd)

10. Reynolds, W.C. and Hussain, A.K.M.F., The Mechanics of an Organized Wave in Turbulent Shear Flow Part 3, Journal of Fluid Mechanics, 54, pp. 263-267, (1972).

11. Roshko, A., On the Drag and Shedding Frequency of Two Dimensional Bluff Bodies, NACA TM 3169, pp. 13-17, (1954).

12. Roshko, A., On the Wake and Drag of Bluff Bodies, Journal of the Aeronautical Sciences, February, p. 127, (1955).

13. Roshko, A. and Fiszdon, W., On the Persistence of Transition in the Near Wake, Problems of Hydrodynamics and Continuum Mechanics, S.I.A.M., Philadelphia, (1969).

14. Schiller, L. and Linke, W., Z. Flugtech. Motorluft., 24, (1933).

15. Zdravkovich, M.M., Smoke Observations of the Formation of a Karman Vortex Street, Journal of Fluid Mechanics, 37, (1969).